TRAVERSING CATALYTIC CONTEXTS FOR INTERROGATION AND DESIGN OF CARBON CONVERSION ELECTROCATALYSTS

by

Joy Shuang Zeng

B.S. Chemical Engineering, Stanford University, 2017

Submitted to the Department of Chemical Engineering
in partial fulfillment of the requirements for the degree of

Doctor of Philosophy in Chemical Engineering
at the
MASSACHUSETTS INSTITUTE OF TECHNOLOGY
June 2023

Author.....
Joy Shuang Zeng
Department of Chemical Engineering
April 6, 2023

Certified by .....
Karthish Manthiram
Visiting Professor
Thesis Supervisor

Certified by .....
Yuriy Román-Leshkov
Robert T. Haslam Professor of Chemical Engineering
Thesis Supervisor

Accepted by .....
Patrick S. Doyle
Robert T. Haslam Professor of Chemical Engineering
Chairman, Committee for Graduate Students

TRAVERSING CATALYTIC CONTEXTS FOR INTERROGATION AND DESIGN OF CARBON CONVERSION ELECTROCATALYSTS

by
Joy Shuang Zeng

Submitted to the Department of Chemical Engineering on April 6, 2023
in partial fulfillment of the requirements for the degree of
Doctor of Philosophy in Chemical Engineering

ABSTRACT

Driving chemical reactions with voltage provides an opportunity to perform thermodynamically difficult reactions at mild temperatures and pressures. One useful chemistry to perform electrochemically is CO_2 conversion. Converting CO_2 into value-added chemicals could be one strategy for abating atmospheric carbon, and electrochemistry is well-suited to provide the driving force required for CO_2 conversion reactions that tend to be highly endergonic. However, amidst the physical complexity of electrified interphases, both mechanistic inquiry and rational catalyst design remain challenging. In this work, we leverage concepts from fields outside of electrocatalysis to establish new strategies for both the interrogation and design of promising electrocatalysts.

We first discuss strategies for interrogating electrocatalytic reaction mechanisms. This is described in the context of CO_2 reduction reaction (CO_2RR) to carbon monoxide (CO) at immobilized metal tetrapyrroles. We detail how collecting and quantitatively analyzing reaction rate data over a wide range of reaction conditions illuminated new details of the CO_2RR reaction mechanism at cobalt phthalocyanine (CoPc). Such mechanistic analysis strategies are often used in heterogeneous thermocatalysis, and this work sets a precedent for also using them in electrocatalysis. We also report a robotic system that automates collection of reaction rate data. We report how the robotic system was used to expand our CO_2RR mechanistic analyses to additional metal tetrapyrroles such as cobalt tetraphenyl porphyrin (CoTPP). Together these works establish a foundation for applying more rigorous kinetic analyses in the space of electrocatalysis.

We next discuss strategies for designing electrocatalytic active sites. We show how a new electrochemical C–C bond formation catalyst was developed by sequentially electrifying known hydroformylation catalysts. We show that electrification of a known organometallic catalyst leads to mechanistically distinct, voltage-driven reactivity. This work pioneers the design principle of using known reactivity from thermal catalysis as an experimental starting point for developing new electrocatalysts.

Together, these works provide new interdisciplinary approaches for interrogating and designing electrocatalytic interphases. In the context of carbon conversion, this work has contributed insight on reaction mechanisms of known CO_2RRs, and, demonstrated new catalysts that further upgrade common products of CO_2RR for greater value-add.

Thesis supervisor: Karthish Manthiram
Title: Visiting Professor

Thesis supervisor: Yuriy Román-Leshkov
Title: Robert T. Haslam Professor of Chemical Engineering

ACKNOWLEDGEMENTS

There are many I'd like to thank for their roles along my PhD journey.

First, I would like to thank funding sources who made my science possible. Cenovus, NSF, MIT Lincoln Labs, MIT Presidential Fellowship, Mathworks Engineering Fellowship, and MITEI Energy Fellowship (Chevron) all funded me at some point. I am genuinely grateful for the flexibility in research topic that many of these funding sources provided me.

I would also like to thank my research advisors, Karthish Manthiram and Yuriy Román. Karthish, you have been great to work with – your kindness and optimism are a relief when all experiments are failing, and your genuine interest in good science has helped charter an intellectually exciting lab environment. I am grateful for the freedom and support you gave me as I pursued different research projects – it helped me build confidence in my scientific creativity. You are also a wizard at scientific communication, and I appreciate your thoughtful feedback that has helped my style evolve over the years. Yuriy, thank you for welcoming me into your group more recently. Working with you and your lab has been a delight – your positivity is absolutely infectious, and your group is so intellectually dynamic – even just attending your group meetings has exposed me to such a diverse array of interesting topics. I have appreciated the time you've taken to support me in various ways – from candid career advice to manuscript preparation.

I would also like to thank my other thesis committee members, Timothy Swager and Heather Kulik. Tim, thank you for genuinely engaging with my updates over the years and always providing insightful feedback. Thanks for lending me your organometallics textbook, for setting up a collaboration on CoPc polymers with your student Mason (even though it eventually didn't work out), among other things. Heather, thank you for your insights over the years as well. I particularly appreciated the time you took to help me with career advice as I was looking towards next steps.

Next, I am lucky to have worked with so many positively inspiring lab mates over the years. I have learned so much from you all, and I cannot imagine a better team to have been part of as I grew as a scientist. To the MIT students over the years - Kindle, you were always such a kind and thoughtful presence in the lab. Your care for both your science and other people was always at 110%. Thanks for all the great science conversations, life ranting, etc. Thank you, as well, for the work you put in to make our lab a safer place. Nate, I always looked up to you as the person who knew a lot about everything – whether it was about relevant literature, transport fundamentals, or gas chromatographs – I felt like you had such keen insights drawn from an impressive wealth of knowledge. Zack, you have always felt very academic with your curious nature about both scientific and random (often food-related) topics. I enjoyed our many office conversations and look forward to hopefully many more in the future. Nik, you always had a very practical approach to research, and I was always impressed by your ability to solve problems and get things to work. Many of my views on what makes research interesting and impactful are heavily influenced by you. Also, thank you for your role in keeping our lab a clean and safe place. Joseph, your quiet sass is always appreciated. It was great to work with you on the automated echem project; I think our teamwork made working out oddities in software and hardware that much more enjoyable. I also think it's crazy that unlike the other experimentalists who turned to DFT during the pandemic, you didn't look back and actually did a whole project in a new field. Minju, we have shared so many experiences together, from our quiet existence together as the MIT lab winds down, to multiple beamline trips. I always enjoy our conversations and I hope we stay in touch even if/when you go to Korea. Your work ethic, as well as ability to try new things, especially applying new characterization techniques,

have always been very impressive to me. Adi, thank you too for always being down for long science conversations. Thanks for leading cluster MD during the pandemic – you are so excellent at teaching and communicating and I am grateful to have benefitted from that when you were in the lab. Katie, you are such a kind and lovely person; thank you for your many contributions as "glue" in our lab. I was so impressed by how you mastered so many different types of experiments and were able to apply them so methodically to your work. Thanks also for always being down for some adventure. Sayandeep, Fang-Yu, Simar, and Trent, we didn't spend so long as lab mates, but we've shared a lot of experiences. I am glad we still hang out and am excited to see what you will accomplish in your new labs. To the MIT postodocs over the years – Minghui, thanks so much for mentoring me in my early years. I learned so much from you about efficiently trying new ideas and getting things to work in lab. Kyoungsuk, thank you for all the times you helped me out in lab, your kindness and generosity were greatly appreciated. I remember fondly the many hours we spent trying to do HAADF-STEM on adsorbed CoPc. Dengtao, thanks also for all of your advice and mentorship. You seemed to know everything about organic chemistry and I learned so much from our conversations. I still number my reactions and weigh reactants the way I saw you doing it. Ruquan, we didn't get to work closely together, but you were a dynamic force in the lab. Glen, despite your short time in the lab, I learned so much chemistry from you, and your passion for science and real impact is really fun to watch. To the MIT undergrads I have gotten a chance to work with – Sierra and Alex – you both are so smart and hard working, and I can't wait to see what both of you will accomplish. Thanks for sticking it out with me, particularly as I myself was learning how to mentor. To those on the Caltech side, I have enjoyed getting to know you all. Our interactions, despite being mostly virtual, have been delightful. Particular thanks to Rachel, Chenyu, Thu, Channing, Grace, Florian, James, Jason, and Wes – at some point my interaction(s) with you helped me continue to feel integrated with the lab. And of course, special thanks to Spencer and Emma who have been wonderful to work with, and I am excited to see where you will take the hydroformylation chemistry. To the Roman lab members, you all are so kind and impressive – and in a relatively short amount of time, I've learned so much from all of you. T those in promo subgroup – Ran, Blake, Bhavish, Karl, Thejas, Melissa, Katie – I learned so much about catalysis and characterization during subgroup meetings and have enjoyed 1:1 conversations with each of you; Jie and Guido, thanks for taking the time to teach me how to use the Autochem; Julie, Jamison and Mostapha thank you for your help with fellowship applications.

Outside of research, I am also very thankful for my experience as a 10.40 TA. Thank you Arup and Brad, for both being inspiring and supportive instructors. It was really special to be able to work with faculty who were so knowledgeable about thermo/stat mech and so passionate about teaching. Thank you Thejas as well, for being an amazing co-TA – I was so impressed by your commitment to caring and also your deep intellectual engagement with the material. It was fun stapling together those final exams the night before.

I have also had a chance to be a Teaching Development Fellow – thanks so much to Ben Hansberry for helping to make the experience so rewarding and thought provoking. I feel so lucky to have had so much engagement with the TLL about pedagogy.

Thanks as well to friends from various parts of my life – ChemE, wushu, taekwondo, undergrad, and even high school – who have helped me have fun in and outside of work. Shout outs to Leslie and Qi for helping me get into snowboarding, Ameya for organizing a legendary winter hike, to Yang and old people for the cape cod bike trip, Jim for going Costco shopping with me, George for cooking me good food, Monica for introducing me to Newell Post, Sarah for bringing a fuzzy menace into my life, Vineet for helping me build a really cool robot, and there is so much more…

Of course, to my partner, Jingfan, you are incredible and I treasure the adventures we had together in grad school. Thank you for always believing in me, encouraging me, and pushing me to be better. My figure design skills are only where they are after years of aesthetic pointers from my more artistic half. And, more broadly to the Yang family, thank you for being so welcoming to me. I am glad we had a chance to meet in person before the pandemic hit.

And finally, to my mom and dad, thank you for supporting me from day one. With you I can talk about any problem I have, ranging from life to research, and always feel much better afterwards. I'm so lucky to have such a wonderful family supporting me.

TABLE OF CONTENTS

List of Figures

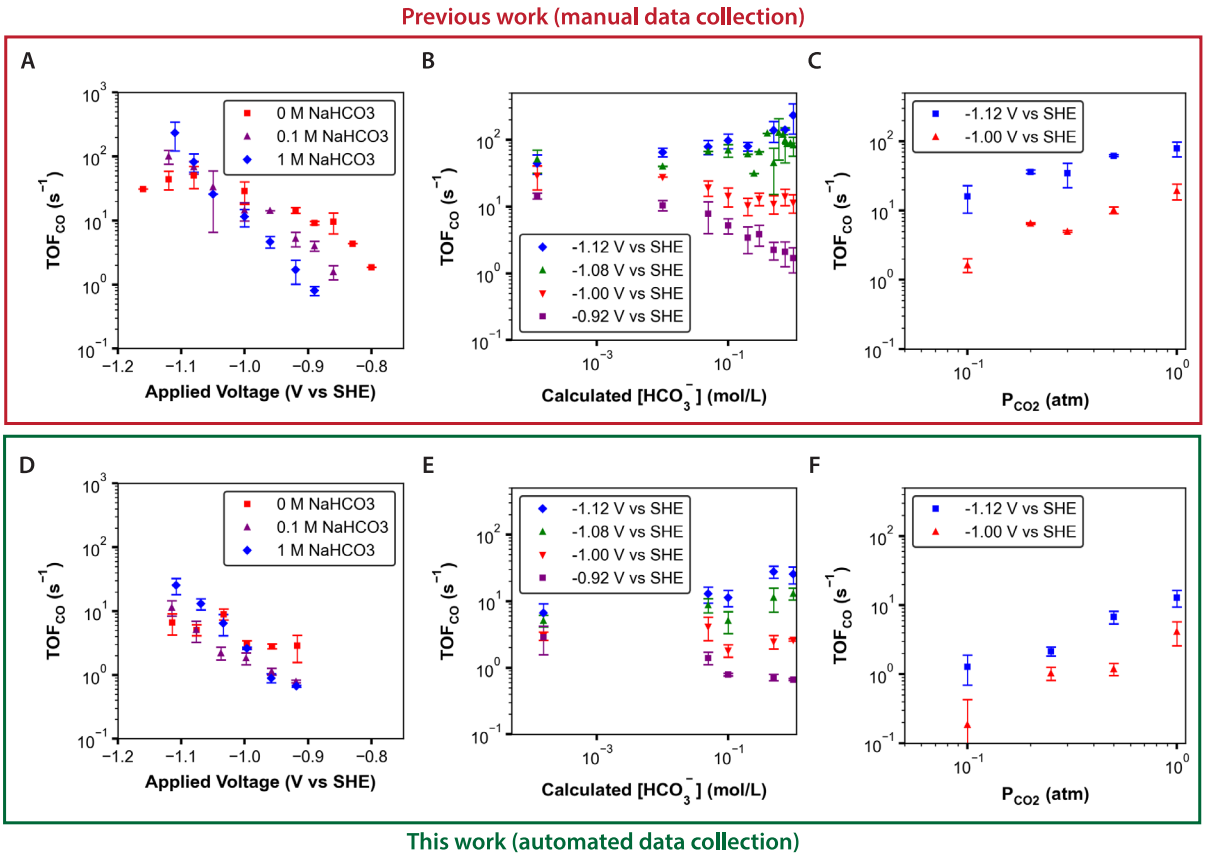

FIGURE 3-2. BENCHMARKING DATA COLLECTED WITH AUTOMATED SETUP. **A-C**, KINETIC DATA FOR CO2RR TO CO AT COPC, REPROCESSED FROM A PREVIOUS WORK. SHOWN FROM LEFT TO RIGHT ARE TAFEL, BICARBONATE, AND CO_2 DEPENDENCES. **D-F**, SAME KINETIC DATA, THIS TIME COLLECTED USING THE AUTOMATED SETUP REPORTED IN THIS WORK....56

LIST OF TABLES

List of Abbreviations and Acronyms

CA: chronoamperometry

CV: cyclic voltammetry

CoPc: cobalt phthalocyanine

CO_2RR: carbon dioxide reduction reaction

EDL: electric double layer

Electro-HFN: electrochemical hydroformylation

EtOH: ethanol

FE: Faradaic efficiency

FID: flame ionization detectorr

GC: gas chromatograph

HER: hydrogen evolution reaction

HFN: hydroformylation (thermochemical)

IPA: isopropyl alcohol

RHE: reversible hydrogen electrode

SHE: standard hydrogen electrode

$TBABF_4$: tetrabutylammonium tetrafluoroborate

TCD: thermal conductivity detector

Thermo-HFN: thermochemical hydroformylation

List of Appendices

1 INTRODUCTION

1.1 Electrocatalysis and sustainability

In electrocatalysis, voltage provides a potent driving force that can enable thermodynamically difficult reactions to be feasible at mild operating conditions.[1] Additionally, the required electrical input can be sourced from renewables such as wind or solar that naturally output electricity. Thus, voltage-driven reactions at electrocatalytic interphases have many potential applications in sustainability.

First, in the space of energy and fuels, electrocatalytic reactions can be used to generate cleaner fuels while also providing energy storage options. Among the most common electrocatalytic fuel-forming reactions are water reduction to hydrogen (H_2) gas and carbon dioxide (CO_2) reduction to carbon-containing fuels. Hydrogen can be used as a clean fuel that generates only water upon oxidation in either a combustion engine or fuel cell.[2] Carbon-containing fuels release CO_2 upon oxidation/combustion, but could be part of a net carbon-neutral cycle since they would be synthesized from CO_2. Common products from CO_2 reduction reactions (CO_2RRs) that have potential applications as fuels include methanol and ethanol.[3–5] Longer-chain hydrocarbons more closely resembling gasoline or diesel are also desired products that would be useful for heavy-duty transportation applications,[6] but are currently difficult to make via electrochemical CO_2RR.[7–9] The above reactions also provide an avenue for renewable energy storage, where voltage-driven reactions transduce electrical energy into chemical energy stored within highly reactive chemical bonds. This concept is similar to that of batteries, but a key difference is that in this case, the energy carrier (i.e., a chemical fuel vs a charged battery) could be more amenable to direct drop-in replacement, particularly in existing transportation infrastructures.[6]

Second, in the space of chemicals manufacturing, electrocatalytic reactions may provide cleaner and safer synthesis routes.[10,11] Although carbon emissions are often associated with

energy and transportation, chemical manufacturing accounted for 24% of global carbon emissions in 2019.[12] Additionally, toxic byproducts from chemical synthesis can cause local pollution. Because voltage provides such a potent driving force for chemical reactions, electrochemistry could enable synthetic routes that do not rely on the harsh operating temperatures, pressures, or chemical reagents often associated with difficult industrial reactions. The academic literature of electrochemical synthesis includes reactions ranging from functionalization of organic molecules[13,14] to generation of small inorganic molecules.[15] Electrochemistry is also currently used in several industrial processes, including the Hall-Héroult (aluminum smelting) and chlor-alkali processes.[16]

1.2 Complexities of catalysis at electrified interphases

Despite the substantial opportunities of voltage-driven catalysis, it remains challenging to design effective electrocatalysts that facilitate desired transformations selectively and efficiently. This is in part because of the complex interactions between solvent, ions, reactants, and catalyst surfaces that arise at an electrified interphase.[17] These complexities present both challenges and opportunities for designing and interrogating catalysts, some of which we summarize below.

1.2.1 Energetics of Faradaic charge transfer

First and foremost, application of voltage at an electrode surface changes the energetics of charge transfer reactions. For elementary steps with explicit charge transfer, also called Faradaic charge transfer steps, thermodynamics change linearly with changes in applied voltage as given by the Nernst Equation (Eq. 1-1):[18]

$$\Delta\Delta G = -nF\Delta V_{app} \qquad \text{Eq. 1-1}$$

Where $\Delta\Delta G$ is the change in reaction free energy, ΔV_{app} is the change in applied voltage, n is the number of electrons being Faradaically transferred, and F is Faraday's constant. There are two remarkable features of this equation. First, it shows that changes in voltage have a linear effect on free energies – this is significant because linear changes in energies often correspond to *exponential* changes physical observables such as equilibrium and rate constants. Additionally, the size of this linear term is large: one electron volt (take $n = 1$ and $\Delta V_{app} = 1$) is greater than thermal energy, or k_BT, at 10,000 degrees Celsius. Intuitively, application of one volt is much more operationally accessible than heating to 10,000 degrees Celsius. One might note that Eq. 1-1 is rigorous in describing thermodynamics of charge transfer reactions, but

often kinetics are more relevant to catalysis. Yet, models of charge transfer kinetics tell a similar story to that of the thermodynamics: Marcus theory derives a quadratic dependence of $\Delta\Delta G^{\ddagger}$ (change in free energy difference between reactants and transition state) on ΔV_{app}, and the Butler-Volmer equation uses a linear dependence to phenomenologically model charge transfer kinetics.[18] Thus, we have laid forth a general fundamental basis for why voltage can be such a potent driving force for chemical reactions that involve Faradaic charge transfer.

Although different models of charge transfer kinetics all show that voltage can make substantial changes to reaction landscapes, the details of these models can be quite complex. For example, the geometry of where charge transfer occurs within the electric double layer (EDL) can reduce the amount of voltage-induced driving force that is locally "experienced" for a charge transfer event. Such effects are described by Frumkin, along with others.[19,20] For inner sphere charge transfer events, similar geometric effects, as well as dipole formation/displacement, and partial charge transfer upon adsorption, can further complicate kinetic models. One thermodynamic framework that has been used to holistically capture these effects is the electrosorption valency (ESV).[21,22] Finally, applied voltage changes the electrochemical potential of the electrode, which is a quantity that has both chemical and electrostatic contributions – in different cases, the driving force from applied voltage can be mainly attributed to one contribution or the other, which leads to different microscopic interpretations of how voltage changes the reaction landscape.[23–25]

In addition to the complexities inherent to individual charge transfer events, the large range of driving forces accessible with applied voltage may also make it more likely for overall reaction mechanisms to become more complex. For example, if various surface intermediates are formed from different steps involving or not involving Faradaic charge transfer, then their relative coverages could change substantially within relatively standard operating voltage windows. Specifically, most charge transfer reactions follow 60 mV/dec scaling, which means that 60 mV causes a 10x change in equilibrium constant. Thus, over potential windows of hundreds of millivolts, relative coverages of reactive intermediates can change by orders of magnitude. Additionally, applied potential can cause complexity even in ostensibly non-Faradaic steps of a reaction mechanism. For example, solvent displacement, which can be important even in at non-polarized solid-liquid interphases,[26] can have a voltage dependence that arises from net formation or displacement of dipoles within the EDL (*vide infra*).[22,27]

1.2.2 Non-Faradaic effects of applied potential

Thus far we have focused on explicitly Faradaic effects of applied potential on catalysis at electrode surfaces. Yet, applied voltage can induce significant perturbations beyond changing the energetics of explicit charge transfer events. Broadly speaking, these contributions involve second-sphere interactions with solvent and ions, as well as inner-sphere changes to active site structure and dynamics.

Electric fields are recognized to play an important role in various catalytic reactions including catalysis within enzymes, at molecular complexes, and on heterogeneous surfaces.[28,29] At electrified interphases, the electric fields within the EDL can be very large, with over a volt or more of potential drop occurring on the length scale of Angstroms. Thus, even for reactions that do not involve explicit charge transfer, electric fields can still affect energetics if there is net change in dipole moment. The potential energy of a dipole in an electric field is given by Eq. 1-2:

$$PE = \vec{\mu} \cdot \vec{E} \qquad \text{Eq. 1-2}$$

Where PE is the potential energy, $\vec{\mu}$ is the dipole moment, and $\vec{E}$ is the electric field. Although we discuss electric fields under non-Faradaic effects, the energetic contribution associated with a dipole in an electric field is closely related to that of Faradaic charge transfer at the interface. In fact, the potential dependence of the electric field effects above can be written in terms of electrosorption valency, where in the crudest sense, the electrosorption valency represents what can be thought of as a "partial" Faradaic charge transfer.[22]

Species in the EDL can also generally perturb catalysis via second sphere interactions beyond the electric field effects described above. Phenomena such as solvent or additive effects are just as relevant at an electrode surface as they are at a typical catalytic solid-liquid interphase. With applied voltage, however, the additional possibility of using polarization to recruit species to the electrode surface and/or orient dipole-containing species, and the effects of such phenomena on catalysis, are a rich topic of exploration.[30–32]

Additionally, applied voltage can induce physical, electronic, and chemical changes to the electrocatalyst surface. For example, oxidative and reductive catalyst restructuring is known to occur on electrocatalyst surfaces, and in some cases has even used been as a strategy for *in situ* creation of highly active sites.[33] For single metal atom sites on an electrode surface, the bulk electrode/support can exert an inductive effect to change the electronic structure at the site.[34] Although such inductive effects are present for all heterogenized single atom sites, at an

electrode surface, such inductive effects could be increased or otherwise tuned with applied potential.

Perhaps more subtly, performing single atom catalysis on an electrode surface can change not only the electronic structure itself, but also electronic structure (or redox) *transitions* that are available to metal active sites. This is particularly true at conductive supports, which can act as electronic reservoirs. Depending on the relative positions between the solid's fermi level and the energetics of the single metal-centred orbitals, electronic coupling between a single site and support could preclude availability of discrete redox transitions to the metal site.[24,35,36] This effect would also be particularly salient at electrode surfaces, where the fermi level of the electrode is set and also maintained to be constant by the applied potential. Particularly for metal sites from organometallic electrochemistry, where the metal often cycles through different distinct redox states, such effects could cause fundamentally different modes of catalysis to occur at ostensibly similar single atom sites embedded in a conductive electrode.

1.2.3 Macroscopic considerations

Finally, any system involving catalysis at a solid/liquid interphase necessitates transport of reactants to and products away from the electrode surface. This can create both fundamental and practical challenges, where mass transport artefacts can convolute mechanistic interpretations of reaction rate data, and mass transport limitations can limit overall performance of electrocatalytic devices.[37–39] Along with these challenges come opportunities in reactor design for, for example, more efficient delivery of both gas[40] and liquid-phase[41] reactants to the electrocatalytic interphase.

1.3 Brief description of this thesis

In this thesis, we explore concepts for the interrogation and design of electrocatalytic active sites in the context of electrochemical CO_2 conversion. As mentioned previously, using CO_2 as a carbon feedstock for value-added fuels and/or chemicals is one strategy for abating atmospheric carbon, and electrochemistry is well-suited to provide the driving force required for CO_2 conversion reactions that tend to be highly endergonic. This work leverages concepts from diverse fields of catalysis, such as heterogeneous and organometallic catalysis, to establish new design strategies for deciphering reaction mechanisms and designing new active sites for carbon conversion electrocatalysts (Figure 1-1).

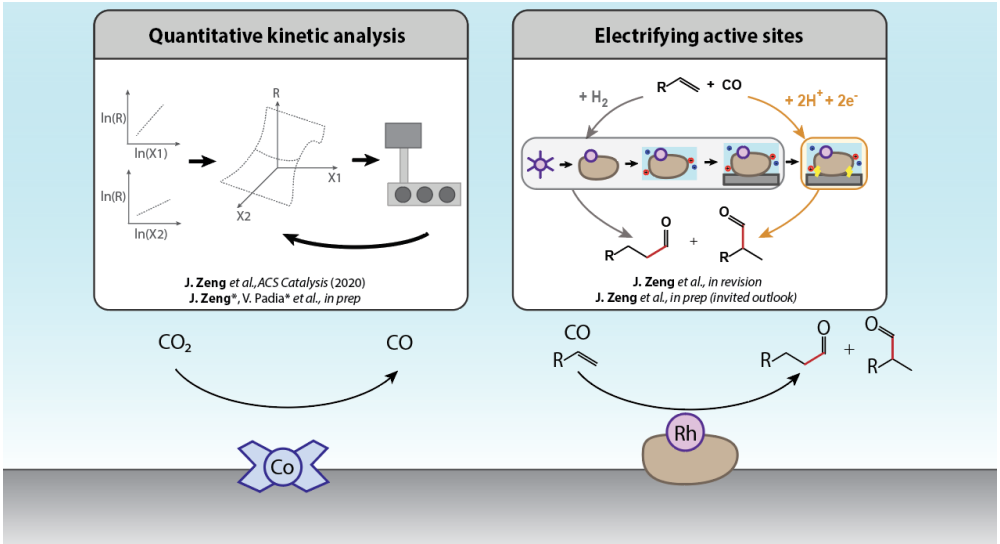

Figure 1-1. Summary of this thesis.

First, in chapters 2 and 3, we demonstrate the strategy of quantitative kinetic modeling for interrogating electrocatalytic reaction mechanisms, which are applied to CO_2RR to CO at immobilized metal tetrapyrroles. Even though CO is one of the simplest possible products from CO_2RR, it is an industrially useful molecule that is used to make methanol, aldehydes, carboxylic acids, and phosgene. Additionally, CO can be used in the Fischer-Tropsch reaction to make long chain hydrocarbon fuels. Immobilized tetrapyrroles such as cobalt phthalocyanine have been known for decades to catalyze CO_2RR with high performance. In these chapters, we show that cohesively fitting kinetic data collected over a wide range of operating conditions lead to new mechanistic insights, even for these ostensibly well-studied reactions. Furthermore, we use automation to improve the workflow for this type of analysis. Thus, in the context of well-studied CO_2RR reactions, we demonstrate the importance and utility of using cohesive and statistically rigorous kinetic analysis to test and formulate mechanistic models of electrocatalytic reactions.

Finally, in chapter 4, we demonstrate a new strategy for designing electrocatalytic active sites, applied in the context of electrocatalytic carbon–carbon (C–C) bond formation. Currently, electrochemical CO_2 conversion to longer-chain hydrocarbon fuels is limited by a lack of electrocatalysts that actually facilitate the C–C bond formation reactions required to make hydrocarbon chains. We show that catalyst active sites that perform C–C bond formation thermochemically can be imported onto electrode surfaces via sequential electrification to achieve C–C bond formation electrochemically. Thus, this work demonstrates an experimental strategy for electrifying a well-studied thermochemical reaction to expose a new electrocatalyst for a difficult and underexplored electrochemical reaction.

2 QUANTITATIVE KINETIC ANALYSIS OF CO_2 ELECTROREDUCTION AT COBALT PHTHALOCYANINE

The material in this chapter is adapted from **Zeng, J.**, Corbin, N., Williams, K., Manthiram, K. Kinetic Analysis on the Role of Bicarbonate in Carbon Dioxide Electroreduction at Immobilized Cobalt Phthalocyanine *ACS Catalysis* 2020, 10, 7, 4326-4336. Reproduced with permission from the American Chemical Society.[42]

2.1 Abstract

The mechanism for carbon dioxide reduction (CO_2RR) to carbon monoxide (CO) at immobilized cobalt phthalocyanine (CoPc) in aqueous electrolytes has been widely debated. In this work, we investigated the mechanism of CO_2RR to CO on CoPc via experimental reaction kinetics coupled with model fitting. Unexpectedly, reactant order dependences and Tafel slopes deviate from commonly expected values and change depending on the testing conditions. For example, (1) the effect of bicarbonate deviates from power law kinetics and transitions from inhibitory to promotional with increasingly reductive potential, and (2) the CO_2 order dependence deviates from unity at more reductive potentials. We propose a kinetic model, chosen from more than 15 candidate models, that is able to quantitatively fit all of the experimental data. The model invokes (1) catalyst poison-ing via bicarbonate electrosorption, (2) mixed control between concerted proton-electron transfer (CPET) and sequential elec-tron transfer-proton transfer (ET-PT), and (3) both water and bicarbonate as kinetically relevant proton donors. The proposed model also predicts that the relative importance of the above factors changes depending on the reaction conditions, highlighting the potential downfalls of broadly applying reaction mechanisms that were inferred from kinetic data collected in a narrow range of testing conditions. This study emphasizes the importance of cohesively using

kinetic data collected over a wide range of operating conditions to test and formulate kinetic models of electrocatalytic reactions.

2.2 Introduction

In electrocatalysis, it can be a challenging task to elucidate reaction mechanisms and develop structure-property relationships amid the complex interplay between catalyst, reacting species, solvent, ions, and electrostatic potential gradient. For carbon dioxide electroreduction (CO_2RR) to carbon monoxide (CO), reaction mechanisms in aqueous electrolytes have been investigated on a suite of heterogeneous catalysts including silver,[43,44] gold,[45–47] metal-nitrogen-carbon catalysts,[48] and immobilized molecular complexes. Immobilized molecular complexes are useful to study due to their atomically well-defined active sites, which could be leveraged to reduce some of the complexity at electrocatalytic interfaces and develop precise structure-property relationships. Among these molecular complexes, cobalt tetrapyrroles such as cobalt phthalocyanine (CoPc) are known to be active and selective for CO_2RR to CO when immobilized on carbonaceous supports.[49–54] On immobilized CoPc, current densities upward of 100 mA/cm^2 and turnover frequencies upward of 100 s^{-1}, with near unity Faradaic efficiencies to CO have been reported.[50,51,55,56]

However, the reaction mechanism of CO_2RR on CoPc is a topic that still remains open to interpretation and debate.[57] Many studies report Tafel slopes around 120 mV/dec, which indicates that the rate-determining step (RDS) likely involves the first electron transfer.[57] However, whether this electron transfer is accompanied by a proton transfer in a concerted proton-electron transfer (CPET) mechanism or if the proton transfer occurs separately in a sequential proton-electron transfer (SPET) mechanism is unclear.

Reaction orders with respect to pH or bicarbonate concentration could be used to distinguish between SPET and CPET pathways. The only experimental kinetic study reporting a bicarbonate order dependence on CoPc for CO_2RR was interpreted at constant voltage versus the reversible hydrogen electrode (RHE),[51] whereas it should have been interpreted at constant voltage versus a pH-independent reference such as the standard hydrogen electrode (SHE).[46,57] Kinetic studies on CoPc-like immobilized cobalt tetrapyrroles such as cobalt tetraphenyl porphyrin,[58] cobalt tetraaminophenyl porphyrin,[59] and iron-nitrogen-carbon catalysts[60] generally suggested that bicarbonate concentration or pH do not affect reaction rate, although studies on perfluorinated CoPc[61] and cobalt protoporphyin IX[62] have suggested that the rate is pH dependent. Spectroscopic studies using in situ x-ray photoelectron spectroscopy (XPS) and

x-ray absorption spectroscopy (XAS)[63] and in situ Fourier-transform infrared spectroscopy (FTIR)[64] have suggested that the CoPc-COOH intermediate forms and is observable during electrolysis, but do not directly provide evidence for whether the intermediate forms from a CPET or SPET mechanism. Additionally, computational studies on CoPc-like tetrapyrroles have reported conflicting conclusions – some studies on cobalt porphine suggested the SPET mechanism is thermodynamically favored,[65,66] whereas another study on the same catalyst suggested that both SPET and CPET mechanisms are possible, and that the preference is pH-dependent.[67] Notably, the above experimental and computational studies may not be comparable because they studied distinct, though similar, catalysts. Nevertheless, largely missing from these debates is a cohesive and comprehensive set of experimental kinetic data on CoPc to support or refute the various proposed mechanistic hypotheses.

Common strategies for studying electrocatalytic reaction mechanisms include collecting Tafel slopes and reaction orders, which are used to infer how many electrons and which reactants participate in reactions during or before the RDS.[45–47] In simple kinetic limits, Tafel-slope and reaction-order analyses can be straightforwardly interpreted when reaction orders are integer values or the Tafel slope is of the form $\frac{60}{n+x/2}$ (where n is an integer, x is 0 or 1, and the transfer coefficient is assumed to be ½).[18] However, in more complex limits of kinetic control, Tafel slopes or reaction orders may deviate from these easily interpretable values or change depending on reaction conditions. For example, it has been shown that Tafel slopes can take on almost any value when the coverages of adsorbed species deviate from the limits of 0 or 1.[68] Typically in these more complex cases, any measured deviations from values associated with simple kinetic limits are only explained qualitatively. However, using the complex kinetic data to specifically and quantitatively test more nuanced mechanistic hypotheses could enhance the development and interpretation of structure-property relationships.

In thermal catalysis, it is more common to evaluate detailed mechanistic hypotheses by fitting multiparameter kinetic models to large sets of kinetic data.[69,70] Such an approach has been used, for example, to study propylene oxidation[71] and acetone conversion.[72] In these contexts, it is well-accepted that macroscopically observed rates usually correspond to the complex interplay of multiple elementary reactions. In electrocatalysis, this complex interplay should also reasonably exist, but, save some exceptions,[73,74] it is usually not quantitatively modeled and compared to experimental kinetic data.

In this work, we present a kinetic study on the mechanism of CO_2 reduction to CO on CoPc with kinetic data collected over a wide range of experimental conditions. Unexpectedly, we observe order dependences and Tafel slopes that deviate from commonly expected values and change depending on the testing conditions. To explain these trends, we propose a kinetic model, which was selected from a wide range of possible mechanistic models, that quantitatively fits all of the experimental data. We show that this model predicts the dominant kinetic mechanism changes depending on reaction conditions, highlighting the danger of broadly applying interpretations of kinetic data collected in a narrow set of testing conditions. This study provides some foundational framework for both understanding catalysis at atomically precise active sites and understanding the complex role of the electrolyte in electrocatalytic systems.

2.3 Materials and methods

2.3.1 Catalyst preparation and characterization

Catalyst electrodes were prepared following a previously reported procedure.[51] Briefly, the catalyst, cobalt(II) phthalocyanine (Strem Chemicals), along with a conductive binder, Nafion (20 wt% dispersion, Fuel Cell Store), were dissolved in N,N-Dimethylformamide (Anhydrous, 99.8%, Sigma Aldrich) to form a catalyst ink. Carbon paper electrodes (Toray060, Fuel Cell Store) were first calcined at 800 ºC in static air to make hydrophilic, oxidized carbon paper (OxCP). Catalyst inks were then drop-casted onto the OxCP electrodes, electrodes were dried at 80 ºC, and used for kinetic tests within 24 hours of preparation. Discussion about the use of Nafion in the electrode is included in Section A.6.1.

Importantly, catalyst loading was kept below 5.8 x 10^{-11} mol/cm^2. At this low loading, all deposited CoPc molecules were assumed to be active, and the turnover frequency was calculated by normalizing reaction rate to the total number of active sites deposited. It has been previously shown that testing in limits of low catalyst loading is essential for mitigating convoluting factors such as catalyst aggregation or mass transport limitations. Mitigating such factors is essential for extracting information about intrinsic turnover frequencies of individual catalyst molecules from bulk electrolysis measurements.[51]

2.3.2 Kinetic measurements

Catalyst electrodes were tested in a 3-compartment cell in which CO_2 flowed through the electrode (presumed to be flooded with electrolyte) and exited through the working

compartment. Platinum foil was used as the counter electrode, leak-free Ag/AgCl (Innovative instruments) as the reference, and Nafion membrane the separator. Products were analyzed every 5 minutes via an online gas chromatograph (GC) (SRI instruments), and reported data points are averages over values collected at 10, 15, and 20 minute marks, during which the GC-sampled headspace composition was expected to reflect steady-state conditions. All data were collected with 85% automatic resistance compensation.

Measurements were performed varying the following experimental settings: sodium bicarbonate ($NaHCO_3$) concentration, potential, and CO_2 partial pressure (P_{CO2}). When varying [$NaHCO_3$], the total salt concentration was kept constant with sodium perchlorate ($NaClO_4$, >98%, Sigma Aldrich) as the balance. Keeping constant ionic strength helps keep the size of the electric double layer (EDL) and activities of ions roughly constant when changing electrolyte composition. Notably, because the chemical potential of the gaseous reactant, CO_2, is set by the gaseous pressure in the headspace, keeping constant electrolyte ionic strength is not a necessary prerequisite for maintaining constant chemical potential of CO_2. When P_{CO2} was varied, the total flow rate was kept constant, and nitrogen gas was used as the diluent. To measure the kinetic isotope effect (KIE), electrolytes were prepared by dissolving sodium carbonate (Na_2CO_3, 99.999%, Sigma Aldrich) and $NaClO_4$ in deuterium oxide (D_2O, 99.9%, Sigma Aldrich). Additional details about all experimental procedures can be found in Section A.1.

For the most rigorous kinetic interpretation, any order dependence is reported at constant V vs. the standard hydrogen electrode, a pH-independent reference point, because only then is it correct to directly interpret the slope of log(rate) vs log(reactant concentration) as the order of the reaction with respect to the varied reactant. This has been discussed in various places in the literature.[46,57]

2.3.3 Modeling and parameter estimation techniques

Modeling and parameter estimation were performed using the Athena Visual Studio (v14.2, W. E. Stewart and M. Caracotsios) statistical software package.[75] Parameter estimation was performed via Bayesian estimation using the natural logarithm of rate as the single response variable. Using the logarithm of rate in the objective function implies an assumption of constant relative error in rate within all conditions tested.[75] This assumption is consistent with the observation that residuals of the best fit model, calculated using logarithm of rate, appear normally distributed (*vide infra*). Lack-of-fit analysis was performed via an F-test, which is

used to test the hypothesis that model and data came from the same distribution, and that residuals between the model and data behave as one would expect for randomly distributed noise.[75,76] The output of the F-test is an F-ratio, which represents model error divided by experimental error. The F-ratio can then be compared to an F-distribution, which is used to determine the probability of observing a higher F-ratio. This probability is denoted as α in this work, and larger α values indicate better goodness-of-fit. Finally, reported uncertainty intervals correspond to 95% highest posterior density intervals. Further details on model fitting can be found in Section A.5.1.

2.4 Results

2.4.1 Kinetic measurements

The rate of CO_2RR to CO was measured at different $NaHCO_3$ concentrations, partial pressures of CO_2, and applied cathodic potentials. Highlighted below are the major observed trends, which are shown in Figure 2-1. It should be noted that, for clarity, Figure 2-1 shows only a representative subset of the kinetic data. A comprehensive table of data at all conditions tested can be found in the supporting information excel file.

When varying the concentration of $NaHCO_3$ at constant ionic strength and constant potential vs SHE, we observed non-power law behavior for the bicarbonate order dependence that shifted from an inhibitory effect of bicarbonate at less reductive potentials to a promotional effect at more reductive potentials (Figure 2-1A). Due to the equilibrium of CO_2 and water to make carbonic acid (H_2CO_3), the as-prepared concentration of $NaHCO_3$ is not exactly equal to the equilibrium concentration of bicarbonate (HCO_3^-) anions at conditions of CO_2 saturation. Therefore, the x-axis variable in Figure 2-1A is the calculated equilibrium value, $[HCO_3^-]_{calc}$ (details in Section A.2). The lowest $[HCO_3^-]_{calc}$ value of ~1 x 10^{-4} M corresponds to no added $NaHCO_3$ (1 M $NaClO_4$). In this text, concentration of sodium bicarbonate will refer to the prepared concentration, and the calculated equilibrium value will be specifically denoted as $[HCO_3^-]_{calc}$.

Tafel behavior was found to vary depending on concentration of $NaHCO_3$ (Figure 2-1B). In the linear range, here taken to be less reductive than -1 V vs SHE, Tafel slopes decreased with increasing bicarbonate concentration (160 mV/dec in 0 M, 141 mV/dec in 0.1 M, and 86 mV/dec in 1 M $NaHCO_3$). Tafel slopes also generally increased with increasingly reductive

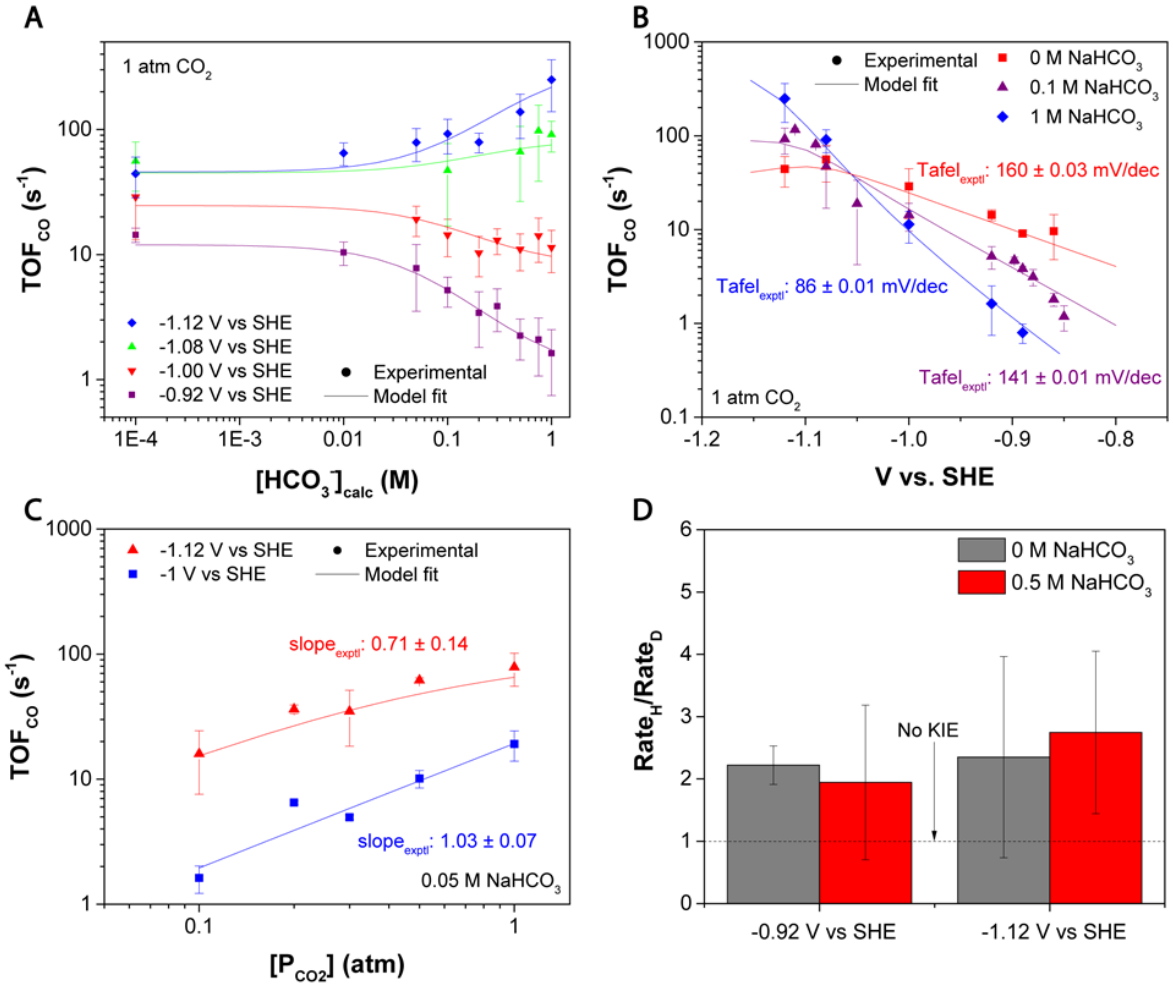

Figure 2-1. Kinetic data and model fits of CO_2RR on CoPc. (A) Bicarbonate order dependence at constant potential vs SHE and ionic strength of 1 M ($NaClO_4$ as the balancing salt) (B) Tafel slopes at different added [$NaHCO_3$] (C) CO_2 order dependence at constant gas flow rate (with N_2 as the balance) (D) Kinetic isotope effect determined from comparing electrolytes prepared with D_2O vs H_2O. Points represent experimental measurements, with error bars indicating one standard deviation ($2 \leq n \leq 10$). Solid lines represent best-fit lines from kinetic model. Annotated slopes are slopes of linear regression lines fitted through all relevant experimental data (regression lines not shown but can be found in Figures S11 and S12). In the case of Tafel slopes, regression lines were fitted only for points with V ≥ -1.0 V vs SHE.

potentials. Increasing Tafel slopes often indicate the onset of transport limitations, but we will later exclude this hypothesis.

The CO_2 order dependence was found to deviate from an expected value of 1 at more reductive potentials (Figure 2-1C). This observation is consistent with a set of previously reported but unexplained CO_2 order dependencies on CoPc.[51] As evidence that the off-unity CO_2 order dependence is not just due to measurement error, we also observed similarly depressed slopes at other $NaHCO_3$ concentrations (Figure A-A13). Graphs explicitly showing linear regressions

that gave the experimental slopes reported in Figure 2-1B and Figure 2-1C are provided in Figures A-A11 and A-A12.

It is worth noting that in Figure 2-1A and Figure 2-1C, due to the equilibrium between CO_2 and carbonic acid, the pH also changes when $[HCO_3^-]_{calc}$ and P_{CO2} are varied. These bulk pH changes were accounted for in thermodynamically equilibrated steps during the kinetic modeling (Section 2.5.1), but turn out to not be physically significant in the final proposed mechanism. Please see Section A.2.2 for an extended discussion.

Finally, kinetic-isotope-effect (KIE) measurements revealed that a proton likely participates in the RDS (Figure 2-1D). A KIE between 2 and 3 was measured in all of the representative experimental conditions tested. This value is consistent with KIE values that have previously been reported, by both experiment and theory, for CPET reactions.[77–79] Although this KIE suggests that a proton participates in the RDS, it provides no information as to whether the source of the proton is hydronium, water, or bicarbonate.

2.4.2 Selectivity against HER and stability

In this analysis, rate towards CO (and not the selectivity towards CO) was the considered dependent variable. Hydrogen evolution (HER) did also occur and was generally found to increase with more reductive potentials (Figure S9). The selectivity towards CO generally had a wide range (from less than 50% to around 100%), and we expected that this was due to background HER that dominated at low overall geometric current densities (generally less than 0.2 mA/cm^2 due to low catalyst loading). In fact, most of the observed HER is likely attributed to this background HER (Figure A-A10), suggesting selectivity towards CO was high for all conditions tested. Additionally, the amount of H_2 generated was often right around or even below the detection limit of the GC. Therefore, we did not model the HER kinetic data because of (1) the low signal-to-noise ratio in the HER measurement and (2) the observation and literature precedent[50,55,56] that HER is a minority reaction.

Catalysts were stable at all of the conditions reported. CoPc catalysts prepared identically to those in this work have been reported to be stable for hours of electrolysis.[51]

2.4.3 Experimental controls

We also performed various control tests to verify that the experimental trends described above were not caused by spurious effects due to referencing shifts, spectator anions, or impurities. Referencing shifts that might have resulted from changes in junction potential in different

electrolyte compositions were ruled out from calibrations to the ferri/ferrocyanide couple (Figure A-A15). Effects from the perchlorate anion were ruled out from perchlorate order dependence experiments (Figure A-A14). Additionally, treating the electrolyte with a chelating agent to remove trace impurities did not have a significant effect on rate (Figure A-A16).

2.5 Discussion

2.5.1 Model formulation and parameter estimation

We used the following procedure to formulate a mechanistic model based on the kinetic data: (1) defining general physical assumptions, (2) enumerating physically feasible kinetic possibilities, and (3) systematically evaluating combinations of the enumerated kinetic possibilities via model fitting.

2.5.1.1 General physical assumptions

Equilibrium bulk electrolyte concentrations were used in the models. Although in CO_2RR, it is well-known that interfacial conditions can deviate significantly from bulk conditions,[44,80,81] we expected that the overall current densities observed in this kinetic study were low enough to reasonably neglect effects arising from mass transport limitations of species participating in the reaction. To evidence our assumption that mass transport limitations should not be at play, we looked at turnover frequency to CO, normalized by total deposited catalyst (TOF_{CO}), as a function of loading. At the most reductive potential, which has the highest rates, we generally see, across several conditions, that there is no clear trend between TOF_{CO} and loading, which suggests mass transport limitations should not be at play (Figure A-A8). If the reaction was mass transport limited, then we would expect TOF_{CO} to decrease with loading, because total rate at the electrode would scale sub-linearly with (and at the diffusion limited current, be invariant to) catalyst loading. One dimensional coupled diffusion-reaction models, assuming either a planar electrode or a hemispherical catalyst, also suggest that for species considered kinetically relevant in our model, there is no significant deviation between bulk and interface concentrations. A more detailed discussion of these transport analyses can be found in Section A.3.

Kinetically relevant proton donors were assumed to be water and bicarbonate. We assumed that hydronium (H_3O^+) and carbonic acid (H_2CO_3) were not kinetically relevant proton donors because (1) CO_2RR is typically performed in near-neutral pH conditions, where [H_3O^+] and [H_2CO_3] are orders of magnitude lower than [HCO_3^-] or [H_2O], (2) there is literature precedent

for favoring kinetically relevant proton donors other than hydronium during CO_2RR due to alkalinity near the cathode,[82] and (3) the interfacial concentrations of H_3O^+ and H_2CO_3 should be very current-sensitive, but we find that TOF_{CO} does not have a clear dependence on total current (Figure A-A8).

The effect of the carbonate (CO_3^{2-}) anion was also not considered. The concentrations of HCO_3^- and CO_3^{2-} are practically difficult to independently manipulate, making effects that might be distinct to one ion or the other difficult to deconvolute. Because [CO_3^{2-}] is orders of magnitude lower than [HCO_3^-], and because carbonate carries a greater negative charge, bicarbonate was considered to be the more likely species to participate in relevant chemistry at the cathode.

Finally, the oxidation state of the cobalt catalyst is not explicitly considered in this work. Though an interesting mechanistic detail and topic of debate,[57] it is one that is not ascertainable via the kinetic analysis in this work because it is not relevant to the level of physical detail being modeled.

2.5.1.2 Enumeration of possible kinetically relevant steps

General literature precedent suggests that the resting state of the CoPc catalyst is unoccupied CoPc (species [1] in Figure 2-2A).[57,63,65–67] From the resting state, the CoPc-COOH intermediate (species [2]) is likely formed from the transfer of CO_2, a proton, and an electron.[63,64] The possible routes we considered for achieving species [2] are illustrated in Figure 2a. They include a CPET mechanism (R1), and SPET mechanisms that involve first an electron transfer (ET) to CO_2, followed by proton transfer (PT) (R2 followed by R3), or PT followed by ET (R4 followed by R5). Full reactions are written out in Table 2-1. A CPET step involving proton and electron transfer to form an adsorbed hydride was not considered due to the literature precedent suggesting that adsorbed hydride species on metal tetrapyrroles typically lead to formate, rather than CO, production.[83] We allowed for the possibility that any of the above paths from species [1] to [2] could occur and that any elementary step along those paths could be rate-determining. From here on, we will use the terminology "R*n*" (for *n*=1 to 5) to mean that the reaction proceeds along the path that R*n* is a part of and that R*n* is the RDS along that path. For example, a mechanism labeled R3 means that the mechanism consists of an ET step followed by a rate-determining PT step.

Table 2-1. List of elementary reactions considered. Associated kinetic constants (if the reaction was assumed to be an RDS) and thermodynamic constants (if the reaction was assumed to be equilibrated before an RDS) are also given. For R1, R3, and R4, proton transfer is assumed to occur from either HCO_3^- or H_2O, and both possibilities are listed separately. Parameters used in the final proposed mechanism are bolded.

Label	Full Reaction	Kinetic Constants [unit]	Thermodynamic Constants
R1 (HCO_3^-)	$\theta_o + CO_2 + HCO_3^- + e^- \leftrightarrow \theta_{COOH} + CO_3^{2-}$	**$k_{1f,HCO3}$ [$(mol/L)^{-1}atm^{-1}s^{-1}$]; $\beta_{1f,HCO3}$**	
R1 (H_2O)	$\theta_o + CO_2 + H_2O + e^- \leftrightarrow \theta_{COOH} + OH^-$	**$k_{1f,H2O}$ [$atm^{-1}s^{-1}$]; $\beta_{1f,H2O}$**	
R2	$\theta_o + CO_2 + e^- \leftrightarrow \theta_{COO}$	k_{2f} [$atm^{-1}s^{-1}$]; β_{2f}	**K_2 [atm^{-1}]**
R3 (HCO_3^-)	$\theta_{COO} + HCO_3^- \leftrightarrow \theta_{COOH} + CO_3^{2-}$	**$k_{3f,HCO3}$ [$(mol/L)^{-1}s^{-1}$]**	
R3 (H_2O)	$\theta_{COO} + H_2O \leftrightarrow \theta_{COOH} + OH^-$	**$k_{3f,H2O}$ [s^{-1}];**	
R4 (HCO_3^-)	$\theta_o + HCO_3^- \leftrightarrow \theta_H + CO_3^{2-}$	$k_{4f,HCO3}$ [$(mol/L)^{-1}s^{-1}$]	$K_{4,HCO3}$ [1]
R4 (H_2O)	$\theta_o + H_2O \leftrightarrow \theta_H + OH^-$	$k_{4f,H2O}$ [s^{-1}]	$K_{4,H2O}$ [mol/L]
R5	$\theta_H + CO_2 + e^- \leftrightarrow \theta_{COOH}$	k_{5f} [$atm^{-1}s^{-1}$]; $\beta_{1f,HCO3}$	
P1	$\theta_o + HCO_3^- \leftrightarrow \theta_{HCO3}$		**K_{HCO3} [$(mol/L)^{-1}$]; γ**

Any kinetic steps after the ones described above were not considered as possible rate determining steps because high experimentally measured Tafel slopes indicated that the RDS should occur early in the catalytic cycle. Measured Tafel slopes were generally around 120 mV/dec, which suggested that the RDS was an initial ET or CPET step. We therefore only considered steps involving the first electron transfer and immediate subsequent chemical steps, but any further steps in the catalytic cycle including and beyond the second electron transfer would have, in the limit of no coverage effects, corresponded to 40 mV/dec (or lower) Tafel slopes and were therefore excluded. Explicit consideration and rejection of some such steps can be found in Section A.4.5.

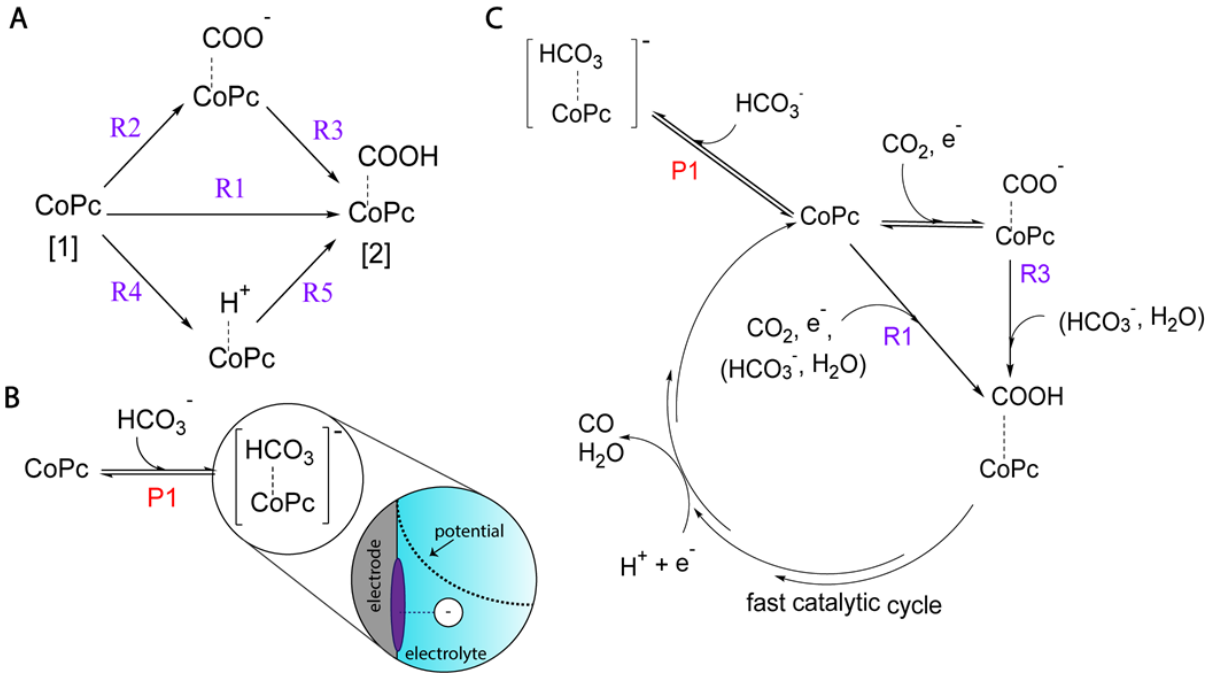

Figure 2-2. Proposed mechanisms of CO_2RR on CoPc. (A) All of the rate determining step possibilities considered during model formulation. For simplicity, only catalyst intermediates are illustrated. Complete reactions are listed in Table 1. Labels for each step are shown in purple. (B) Potential-dependent bicarbonate adsorption onto CoPc. (C) The final proposed model (M2) consisting of (1) bicarbonate poisoning (P1) and (2) mixed control between SPET (R1) and ET-PT (R3) pathways. 9 fitting parameters are associated with this mechanism.

The turnover frequency (TOF) corresponding to each candidate RDS was expressed using Butler-Volmer kinetics:

$$TOF_j = k_j \theta_k e^{-\beta_j x F \phi / RT} \prod_{i_{react}} C_i^{|\nu_i|} \qquad \text{(Eq. 2-1)}$$

where constant terms in the equation are defined as follows: x is the number of electron transfers that occur during the RDS (either 1 or 0), R is the ideal gas constant, T is the temperature in Kelvin, F is Faraday's constant, i enumerates all of the reactants that occur in the forward reaction of the RDS, and ν_i are the stoichiometric coefficients of those species i. Fitted parameters are defined as follows: k_j is the rate constant and β_j is the transfer coefficient of the RDS. Typically the transfer coefficient is assumed to be around 0.5, but in our general model formulation, β_j was allowed to vary between 0 and 1. Independent variables are the following: ϕ is the applied cathodic potential, and $\{C_i\}$ are the concentrations of the reactants. The term θ_k corresponds to the fraction of CoPc catalysts sites occupied by a kth species and

is the site at which the RDS proceeds. θ_k incorporates additional concentration and potential dependences, and is expressed using the definition of equilibrium:

$$\theta_k = K_k \theta_o \, e^{-xF\phi/RT} \prod_m C_m^{\nu_m} \quad \text{(Eq. 2-2)}$$

where K_k is the equilibrium constant x is the number of electrons transferred to form θ_k from θ_o, m enumerates all of the reactants and products in the equilibrium, and ν_m are the stoichiometric coefficients of those species *m* (positive for products, negative for reactants). The term θ_o corresponds to the fraction of unoccupied CoPc catalyst sites, and is analytically determined from a site balance:

$$\theta_o = \frac{1}{1 + \sum_k \frac{\theta_k}{\theta_o}} \quad \text{(Eq. 2-3)}$$

If multiple RDS possibilities were allowed to occur in parallel (for example, considering multiple proton donors for a single R*n*, or, allowing multiple R*n* to occur in parallel), the total rate was expressed as the sum of the individual contributions:

$$TOF_{total} = \sum_j TOF_j \quad \text{(Eq. 2-4)}$$

If two steps in series were both considered rate determining, a site balance was performed by assuming steady state concentration of the intermediate connecting the two kinetically relevant steps[84] (Section A.4.2).

2.5.1.3 Catalyst poisoning possibility

In addition to considering various possible rate determining steps, we also allowed the possibility for bicarbonate to adsorb to and poison the catalyst (Figure 2-2B). Other electrolyte ions such as chloride,[85,86] phosphate,[46] and bulky cations[87] have been implicated in having site-blocking effects on heterogeneous CO_2RR catalysts. We hypothesized that such poisoning could explain the inhibitory effect of bicarbonate that was observed at less reductive potentials. In addition, because bicarbonate is a negatively charged anion and reductively polarizing an electrode to more negative potentials makes the electrode more negatively charged, it was also physically consistent that the apparent inhibitory effect of bicarbonate was attenuated at more reductive potentials. Therefore, this poisoning mechanism, which we will label as P1, added θ_{HCO_3} to the set of θ_k in the site balance described in equation Eq. 2-3:

$$\theta_{HCO_3} = \theta_o K_{HCO_3} [HCO_3^-] e^{\gamma F\phi/RT} \quad \text{(Eq. 2-5)}$$

where γ is the electrosorption valency of the bicarbonate anion and, in the limit of no charge transfer between adsorbed ion and electrode, is often interpreted to represent how far the charge on the adsorbed anion lies from the electrode divided by the characteristic length scale of the potential drop in the electric double layer. A γ value closer to 1 indicates that the adsorbed anion's negative charge resides at the electrode surface, whereas a γ value closer to 0 indicates that the adsorbed anion's negative charge lies outside of the double layer.[21,88] Exclusion of other anions as poisoning species is discussed in Section A.4.6, and discussion on the best-fit value of γ can be found in Section 2.5.3.1.

2.5.1.4 Systematic model exploration

We enumerated all combinations of the RDS options shown in Figure 2-2A and bicarbonate poisoning option in Figure Figure 2-2B to generate a list of candidate kinetic models. Fully-written reactions for these steps are given in Table 2-1. We generally considered up to two distinct RDSs be kinetically relevant (considered in either series or parallel, depending on whether or not they resided along the same reaction pathway). The assumption of rate determining or kinetically relevant steps was taken to mean that any prior steps were in thermodynamic equilibrium, and any subsequent steps were rapid, implying no coverage effects from steps subsequent to the RDSs. These assumptions also implied that the energetic landscape of the catalytic cycle did not contain any large energy differences between intermediates other than in the kinetically relevant steps.[89]

Parameters for the enumerated models were fit to the experimental data, and the optimum parameter fits were used to evaluate candidate kinetic models. Rejected models had low goodness-of fit statistics (α value) and also did not capture one or more of the qualitative order-dependence trends described above. The α value is an output of the F-test, which assesses the likelihood that the deviation of model from data is due to random error. Generally, α values below commonly cited cutoff values such as 0.05 or 0.01 indicate a model should be rejected.[75,76] A subset of the considered RDS combinations is shown in Table 2-2. The models that are not explicitly listed in Table 2-2 had α values of 0 (all enumerated models can be found in Sections A.4.4 to A.4.6).

Table 2-2. Partial enumeration of candidate models. Higher α values indicate better goodness of fit.

Mechanism	**Total # Parameters**	**α value**
M1: R1 + R2 + P1	8	0.001
M2: R1 + R3 + P1	**9**	**0.109**
M3: R1 + R4 + P1	8	0.001

M4: R1 + R5 + P1	9	0.001
M5: R2 + R5 + P1	7	0.000
M6: R1 + P1	6	0.001
M7: R1 + R3 + R5	10	0.000
M8: R1 + R2 + R3 + P1	11	0.109*

* best-fit parameter values made the model equivalent to M2

2.5.2 Proposed mechanism for CO_2RR on CoPc

2.5.2.1 Model description

The proposed mechanism (Model M2 in Table 2-2) includes mixed kinetic control between a CPET mechanism and an SPET mechanism (Figure 2-2C). The SPET mechanism consists of a facile ET step followed by a rate-determining PT step and can therefore be more specifically described as an ET-PT step. For both the CPET and ET-PT, both water and bicarbonate are proton donors. Additionally, the mechanism invokes catalyst poisoning via bicarbonate adsorption. TOF from the model is expressed as follows (precise expressions for each term can be found in Section A.4.2):

$$TOF = \frac{r_{1HCO3} + r_{1H2O} + r_{3HCO3} + r_{3H2O}}{1 + \frac{\theta_{HCO3}}{\theta_o} + \frac{\theta_{COO}}{\theta_o}} \tag{2-6}$$

Where in total, there are 9 fitting parameters: four kinetic rate constants, two CPET transfer coefficients, two equilibrium constants, and the bicarbonate electrosorption valency.

2.5.2.2 Statistical analysis of selected model

The proposed kinetic mechanism was the only enumerated mechanism that qualitatively and quantitatively fit the experimental data. From Table 2-2 it can be seen that model M2 was the only model with an α value greater than 0.05. Additionally, predictions of the model M2 qualitatively match key experimental trends, which can be seen in Figure 2-1A, B and C, where solid lines represent model fitting results.

Additionally, the normal probability plot from the model fit appeared linear (Figure A-A5), which indicates that the distribution of model error was normal. A lag plot of the residuals appeared random (Figure A-A6), indicating error in the model should be random and uncorrelated. Therefore, the normal probability plot and lag plot confirmed the normal distribution of random error that is a prerequisite condition to the validity of a goodness-of-fit test such as the F-test.

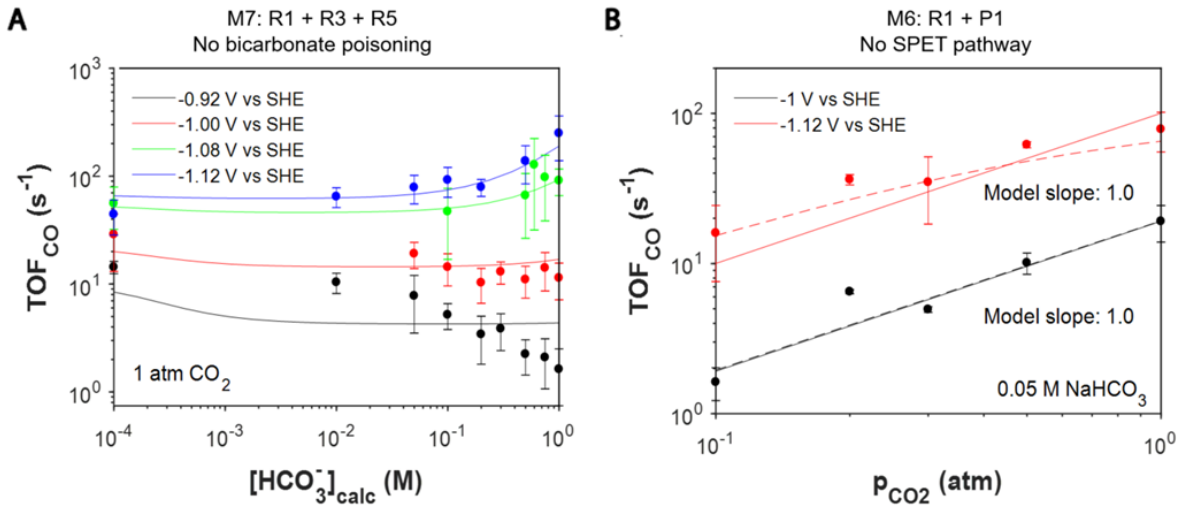

Figure 2-3. Examples of excluded models. (A) A model that does not invoke bicarbonate poisoning is unable to explain negative bicarbonate order dependence at less reductive potentials. (B) A model that does not invoke parallel ET-PT and CPET is unable to explain off-unity CO_2 order dependence at more reductive potentials. Points represent experimental data, solid lines represent rejected model fit, and dashed lines in (B) represents model fitting trend from the best-fit model, M2.

2.5.2.3 Rejected models

The following discussion of rejected models serves to illustrate that the kinetic steps invoked in model M2 were all necessary to describe the experimental data and that models which had similar complexity but invoked different kinetic steps were not able to fit the data. We find it necessary to include such a discussion because often, adding complexity to a model improves model fit simply by virtue of having more fitting parameters. From the discussion below, we would like to argue that the better fit of model M2 to the kinetic data was due to the inclusion of relevant chemistry and not just a general artifact of including more parameters.

The importance of bicarbonate poisoning is illustrated by the lack of fit of model M7 Table 2-2. Even when a complex mixed control between three RDS steps is invoked, model M7 cannot capture the inhibitory effect of bicarbonate that is observed at less reductive potentials (Figure 2-3A). The importance of allowing a CPET and an ET-PT step to occur in parallel is illustrated by the lack of fit of model M6 in Table 2-2. Without a parallel ET-PT pathway, model M7 is unable to capture the off-unity CO_2 order dependences that were observed at more reductive potentials ((Figure 2-3B).

We also considered a model that allowed R1, R2, and R3 to all be kinetically relevant steps (M8 in **Error! Reference source not found.**), essentially adding extra parameters to relax the assumption that the electron transfer (R2) in the ET-PT pathway was rapid. The best-fit

parameters from that model still converged to M2, predicting that the forward and reverse reactions of the electron transfer step (R2) were at least two orders of magnitude faster than the forward reaction of the proton transfer step (R3).

The lack of fit of all of the other excluded models enumerated in Table 2-2 and Appendix A suggests that the chemistry specific to M2 was important for capturing the experimental observations. Of so many different enumerated model mechanisms, all with a similar number of fitting parameters, model M2 had, by far, the highest goodness-of-fit statistic and was the only model that could qualitatively capture the observed experimental trends. Based on these results, we propose model M2 to describe the complex interplay of anions and proton donors in CO_2RR to CO on CoPc.

2.5.3 Physical interpretation of kinetic model

2.5.3.1 Interpretation of parameter values

The best-fit parameter values, expressed with respect to the representation in which they were fit, are listed in Table 2-3. It is only meaningful to compare values of rate constants that correspond to reactions with the same potential dependence. This is due to the arbitrary referencing of potential that was used in this model (see Section A.4.2 for details). Changing this arbitrary reference will change the relative magnitudes of rate constants that correspond to steps with different potential dependences. Therefore, we can only meaningfully compare rate constants in the protonation step, R3, and note that the rate constant for bicarbonate is larger than that for water ($k_{3f,HCO3}>k_{3f,H2O}$). This trend is qualitatively consistent with the physical intuition that bicarbonate is a stronger acid than water and should therefore donate protons more easily. Quantitatively, it might be surprising that the ratio between $k_{3f,HCO3}$ and $k_{3f,H2O}$ is lower than the ratio between K_a values of bicarbonate and water. This discrepancy between thermodynamic driving force and kinetic rate for proton transfer is reported in similar contexts[90,91] and may be due to local structure of solvation, ions, and electric fields near the electrode.

The transfer-coefficient values of the CPET step also have physical meaning. The transfer coefficient of the CPET with bicarbonate as the proton donor was, within error, approximately 0.5. In electrocatalysis, β is typically assumed to be 0.5.[18,90] The transfer coefficient of the CPET with water as the proton donor was around 0.25, which is lower than this expected value. It has been postulated that transfer coefficients can deviate from 0.5 due to the structure of the

proton donor or differences in charge distribution in the EDL.[90] In this context, the physical reason for this low transfer coefficient may be a topic of further inquiry.

The electrosorption valency of bicarbonate adsorption was found to be around 0.2. This low value suggests that the negative charge of bicarbonate resides closer to the edge of the EDL than it does to the electrode surface. This value of 0.2 is conceivable given that the size of bicarbonate and the EDL are of similar magnitudes. The unsolvated, thermochemical radius of the bicarbonate anion is 156 pm,[92] and the width of the EDL in 1M salt is around 300 pm.[18] In a carbonic anhydrase enzyme, the distance between the oxygens of a bound bicarbonate ion and the enzyme's cobalt center was found to be around 250 pm.[93] Additionally, it is conceivable that adsorbed bicarbonate could be polarized by the EDL such that most its negative charge resides on the side that is farthest away from the electrode surface. However, given uncertainty about the actual bond distance between bicarbonate and CoPc, and general uncertainty about the molecular arrangement of ions, charge, and solvent in the EDL, a more specific geometric interpretation of this electrosorption valency value is difficult.

Table 2-3. Best-fit values and physical meaning of parameters in the proposed model (M2). ± values indicate 95% highest posterior density intervals.

Parameter	Value	Meaning
$\ln(k_{1f,HCO3})$	3.4 ± 0.71	CPET (HCO_3^-) forward rate constant
$\ln(k_{1f,H2O})$	2.7 ± 0.15	CPET (H_2O) forward rate constant
$\beta_{1f,HCO3}$	0.44 ± 0.20	CPET (HCO_3^-) transfer coefficient
$\beta_{1f,H2O}$	0.23 ± 0.05	CPET (H_2O) transfer coefficient
$\ln(k_{3f,HCO3})$	6.1 ± 0.65	PT (HCO_3^-) forward rate constant
$\ln(k_{3f,H2O})$	3.5 ± 0.52	PT (H_2O) forward rate constant
$\ln(K_2)$	-5.8 ± 0.59	ET equilibrium constant
$\ln(K_{HCO3})$	2.6 ± 0.43	Bicarbonate poisoning equilibrium constant
γ	0.16 ± 0.12	Bicarbonate electrosorption valency

2.5.3.2 Model-predicted limits of kinetic relevance

The proposed kinetic model allows for occupation of CoPc by both adsorbed HCO_3^- and CO_2, mixed control between CPET and ET-PT, and two kinetically relevant proton donors. The relative importance of these various effects are discussed below.

With respect to site occupation, the fraction of CoPc sites that are occupied by HCO_3^- increases with [HCO_3^-] and decreases as applied potential becomes more reductive (Figure 2-4A). A more reductive potential reduces HCO_3^- occupation due to electrostatic repulsion between bicarbonate and a more negatively charged electrode. The fraction of CoPc sites that are occupied by CO_2 radical anion generally increases at more reductive potentials (Figure 2-4B) because the formation of the CO_2 radical anion involves a reductive electron transfer. Higher CO_2 partial pressure also favors CoPc occupation by the CO_2 radical anion (Figure A-A19).

With respect to dominant reaction kinetics, the reaction shifts from CPET-dominant to ET-PT-dominant as the applied potential becomes more reductive (Figure 2-4C). This is because formation of the CO_2 radical anion, which is a step along the ET-PT pathway, has a stronger potential dependence ("60 mV/dec") than the CPET step (~"120 mV/dec"). Interestingly, a shift from CPET to ET-PT at more reductive potentials has also been proposed as a reaction mechanism for CO_2RR to CO on silver.[94]

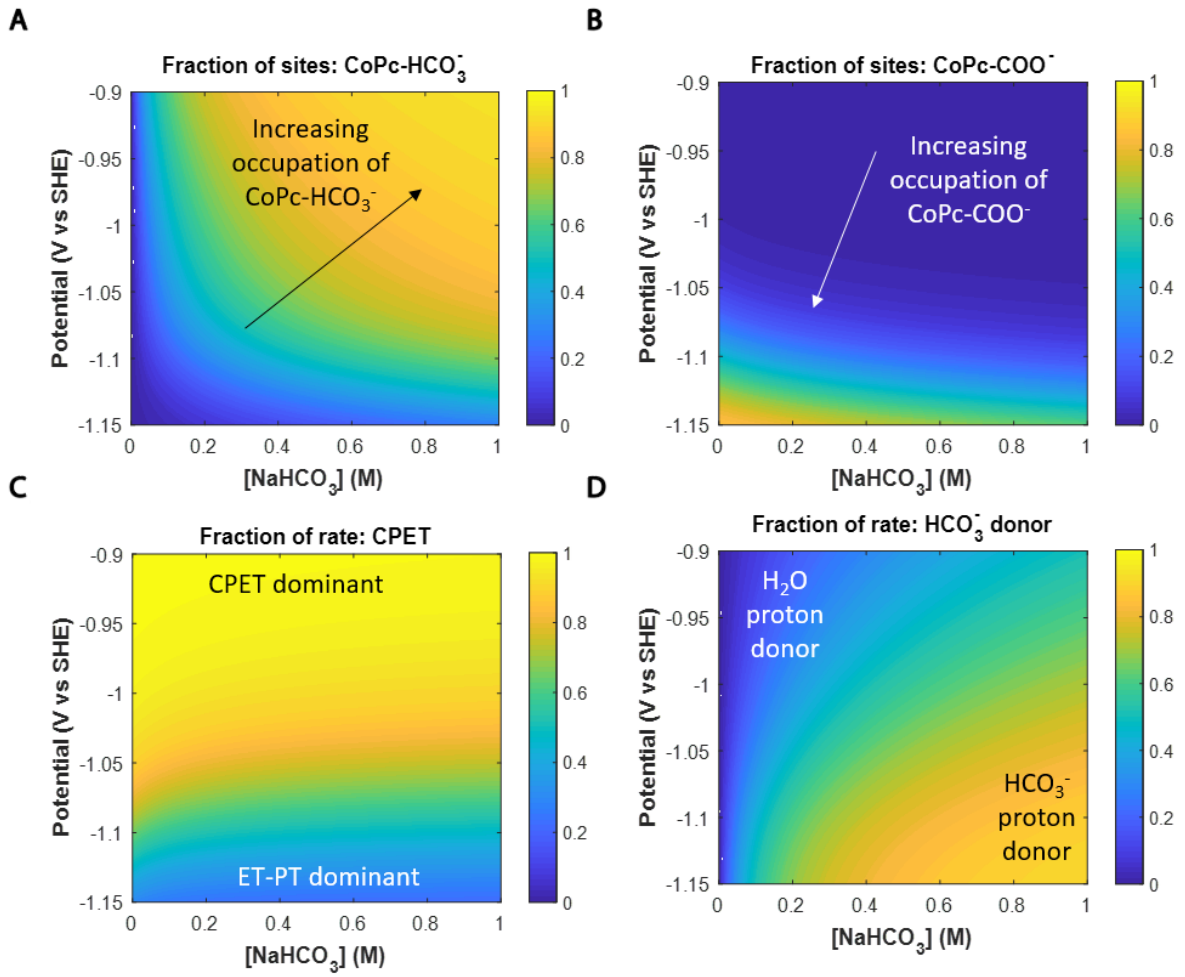

Figure 2-4. Model-predicted limits of kinetic control, calculated at 1 atm CO_2. (A) Fraction of sites occupied by bicarbonate anion. (B) Fraction of sites occupied by COO radical anion. (C) Fraction of total rate occurring through CPET. (D) Fraction of total rate occurring via bicarbonate as a proton donor.

With respect to proton donor, bicarbonate is dominant at higher [HCO_3^-] and more reductive potentials (Figure 2-4D). The kinetic relevance of HCO_3^- should naturally be linked to its concentration, and the potential dependence can be explained as follows: at more reductive potentials when ET-PT is dominant, HCO_3^- is the dominant proton donor simply because $k_{3HCO3}>k_{3H2O}$. At less reductive potentials when CPET is dominant, the importance of HCO_3^- as a proton donor increases with more reductive potentials because $\alpha_{1HCO3}> \alpha_{1H2O}$, which means that the rate of CPET with HCO_3^- is more potential-sensitive.

The discussions above were considered at constant CO_2 partial pressure of 1 atm. Similar graphs at constant [HCO_3^-] and varying P_{CO2} can be found in Section 0. The only term with interesting CO_2 sensitivity was the occupation of CoPc-COO^-, which, as noted earlier, increased as P_{CO2} increased.

2.5.3.3 Model-based explanation of kinetic data

From the physical trends discussed above, it is possible to explain the experimental trends shown in Figure 2-1. First, the bicarbonate order dependence at less reductive potentials is negative because CoPc- HCO_3^- occupation is significant and HCO_3^- is not yet a significant proton donor. Therefore, the net effect of adding more bicarbonate is to inhibit rate. At more reductive potentials, the poisoning effect of HCO_3^- becomes attenuated, and the importance of HCO_3^- as a proton donor increases. Therefore, at more reductive potentials, the net effect of adding more HCO_3^- is to increase rate. To further support this hypothesis, we also measured bicarbonate order dependence in the presence of 0.5 M, pH 7 phosphate buffer (Figure A-A17). Because $H_2PO_4^-$ has a pKa of 7.2 whereas HCO_3^- has a pKa of 10.33, when the two ions are present at similar concentrations, $H_2PO_4^-$ should be the preferential proton donor. We did observe that at more reductive potentials, in the presence of phosphate buffer, the apparent positive bicarbonate order dependence was attenuated.

Second, in the linear, low-overpotential regime, the Tafel slopes collected at high $[HCO_3^-]$ were smaller than those collected at low $[HCO_3^-]$. The reason for this is two-fold. First, in the low-overpotential regime, CPET is dominant. CPET with HCO_3^- as the proton donor is more dominant at higher $[HCO_3^-]$ and has a lower Tafel slope than CPET with H_2O as the proton donor because $\alpha_{1HCO3} > \alpha_{1H2O}$. Additionally, at higher $[HCO_3^-]$, bicarbonate poisoning is a more important phenomenon. As a result, applying a more reductive potential in higher $[HCO_3^-]$ has a stronger effect in both promoting the Faradaic reaction step and reducing the amount of bicarbonate poisoning, and should therefore have a lower Tafel slope. In the high overpotential regime, when the reaction shifts towards an ET-PT mechanism, all of the Tafel slopes increase. This is somewhat counterintuitive because the ET-PT mechanism is generally associated with a lower Tafel slope than the CPET mechanism. However, in this model, the Tafel slope increases due to coverage effects of the θ_{COO} species from the equilibrated ET step in the ET-PT.

The off-unity CO_2 order dependence at more reductive potentials can be understood by coverage effects from occupation of CoPc-COO^- sites at more reductive potentials. Since the occupation of CoPc-COO^- is in the site balance in the denominator of the rate equation, higher occupation of CoPc-COO^- results in a lowered rate. Therefore, when increasing the CO_2 partial pressure, the competing effects of increasing the amount of reactant for an RDS step but also increasing CoPc-COO^- occupation result in apparent CO_2 order dependences that are less than 1.

2.5.4 Related systems

Non power law, inhibitory, and potential-dependent effects of bicarbonate concentration were also observed with immobilized cobalt tetraphenyl porphyrin (CoTPP) (Figure A-A18), which suggests that the mechanistic hypotheses presented in this work may also be relevant to other tetrapyrrole or tetrapyrrole-like CO_2RR catalysts. The specific generalization of this hypothesis to other catalysts could be the topic of future investigation.

2.6 Conclusions

In this work, we investigated the mechanism of CO_2RR to CO on CoPc through fitting kinetic models to experimental data collected over a wide range of testing conditions. Particularly when order dependencies and Tafel slopes deviate from commonly interpreted values, this strategy of simultaneously fitting a wide range of the kinetic data allows one to cohesively and quantitatively develop detailed mechanistic hypotheses.

The proposed mechanism itself may contain some interesting implications. First, the somewhat unconventional, though not unreported,[67,94] mixed control between CPET and ET-PT suggests that it may be generally relevant to consider mixed control between these two pathways when studying electrochemical reaction mechanisms, and that the dominant mechanism can actually change depending on the operating conditions. This is important because the conditions at which kinetic data are collected may be different from practically relevant operating conditions, where different reaction kinetics could be at play. For example, electrochemical kinetic data is usually collected at low overpotentials to achieve low currents that avoid convolution with mass transport,[45,47] but practical systems should have higher currents and may operate at higher overpotentials to drive that current. From our work, we see that the mechanism may change depending on the operating voltage and that this "voltage gap", which could be analogous to the "pressure gap" that is well-acknowledged in thermal catalysis,[95] cannot necessarily be ignored. Kinetic insights obtained from one set of testing conditions may not be generally applicable to a wider range of operating conditions. This also illustrates the point that when making comparisons across different catalysts to understand some type of structure-property relationship, the testing conditions at which the catalyst comparisons are made may influence which underlying physical phenomena are most dominantly at play.

Additionally, this model makes a quantitative prediction about various kinetic roles of bicarbonate in the catalysis - as a proton donor and as a catalyst poisoning species. Such a kinetic hypothesis may be very relevant to another open question in CO_2RR electrocatalysis:

the role of electrolyte anions.[96–101] Understanding the role of anions in general, or even just understanding the role of the bicarbonate anion (which will always be present in CO_2RR due to the equilibrium between CO_2 and water) is a complicated prospect because of the multifaceted roles that anions such as bicarbonate can assume. For example, bicarbonate may be thought of as a proton donor, pH buffer, or a generally charged electrolyte species; all of these physical roles could have separate influences on reaction rate through perturbing kinetics, mass transport, and the electric double layer. In this work, we were able to circumvent some of this complexity by studying a well-defined catalyst active site and operating in conditions where mass transport limitations did not affect the reaction kinetics. By quantitatively and specifically analyzing the kinetic role of bicarbonate in CO_2RR at a well-known catalyst, this study may augment the foundational basis and analytical framework for future work that seeks to generally understand the role of electrolyte composition in complex electrocatalytic systems.

3 AUTOMATING ELECTROCHEMICAL KINETIC ANALYSIS

Content of this chapter adapted from following manuscript, in preparation: **Zeng, J.***, Padia, V.*, Maalouf, J., Limaye, A., Liu, A., Hunter, I., Manthiram, K. Automated platform for quantitative kinetic analysis of CO_2 electroreduction mechanisms at immobilized metal tetrapyrroles.

3.1 Introduction

Kinetic analysis of reaction rate data is a prevalent and powerful strategy for reaction mechanism interrogation. However, this task, which involves mapping a finite set of reaction rate data to one of ostensibly infinite mechanistic possibilities, can be complex and challenging.[102] Commonly, kinetic analysis of steady-state reaction rate data is analyzed with one of two frameworks, which we will term linearization and cohesive model fitting. With linearization, one assumes simple forms of the rate equation for which the contributions of different reactants can be factored separately and linearized on log-log or semi-log graphs. This is the basis for typical reactant order dependence and Tafel analyses. Although linearization can provide valuable mechanistic insight with relatively light data requirements, it requires highly simplifying mechanistic assumptions. For example, if coverages of surface intermediates change significantly with different reaction conditions, or, if there is partial rate control between two different elementary steps within the mechanism, these effects may lead to "uninterpretable" curvature or apparent slopes in typical Tafel or order dependence plots.[68,102–104] On the other hand, in cohesive model fitting, one assumes a general rate equation which need not be factorable nor linearizable. Such models are then fit to an entire set of reaction rate data, ideally collected over a wide range of reaction conditions.[69,72,105,106] Model discrimination and parameter estimation are thus performed using quantitative statistical methods.[75] Cohesive model fitting requires more data and more quantitative statistical analysis of that data, and is thus better suited to capture mechanistic complexity.

The field of electrocatalysis has traditionally relied on interpretations of linearized kinetic data. However, given the substantial effect of voltage on reaction energy landscapes, as well as the general complexity of electrified interphases, it might be expected that many electrocatalytic reactions actually follow complex, non-linearizable reaction mechanisms. For example, dynamic coverages of surface intermediates lead to complex kinetic behavior,[68,102–104] and such phenomena should intuitively be quite prevalent in electrocatalysis. Often, for an elementary step involving charge transfer, only 59 mV can cause a 10x change in equilibrium constant (i.e., 59 mV/dec scaling). This means that within a potential window of even just a few hundred millivolts, changes in applied potential could substantially change the relative coverages of different surface intermediates. Additionally, effects from solvent or electrolyte displacement, which are general to solid-liquid interfaces[26] but may also have additional potential dependences,[22,27,88] can further complicate reaction rate data. Thus, the wider use of cohesive model fitting in electrocatalysis should shed light on complex kinetic behavior that has been unexplained or even missed by typical, linearization-based kinetic analyses.

In fact, analyses beyond linearization have helped to shed light on some of the complex kinetic phenomena[107] that are increasingly discussed for the electrochemical CO_2 reduction reaction (CO_2RR). For example, a meta-analysis of reported Tafel data across many classes of CO_2RR catalysts showed that Tafel slopes do not show a strong preference for commonly interpretable values (e.g., 120, 60, 40 mV/dec).[108] This pointed to the likely prevalence of additional mechanistic phenomena not being fully captured with Tafel analysis. Additionally, cohesive kinetic analysis of complex reaction rate data evinced the presence of mechanistic complexities such as competitive electrolyte adsorption and mixed control for CO_2RR to CO on cobalt phthalocyanine.[42] Additionally, kinetic modeling coupled with continuum transport modeling illustrated the importance of mass transport and competing reactions for explaining complex kinetic behavior of CO_2RR to CO at Ag.[109]

One of the barriers for implementation of cohesive kinetic analysis in electrocatalysis may be its requirement for a larger set of reaction rate data. For example, if a system has n independent variables that affect rate (e.g., reactant concentration or voltage), a linearization-based strategy assumes no correlations between the independent variables thus the data requirement scales with nx. Here, x represents the number of distinct points collected for an independent variable (e.g., 5 different applied voltages). However, to fit to a more complex kinetic model, it is necessary to collect data that captures correlations between the different independent variables, and thus the data requirement may scale with up to x^n. For example, cohesive kinetic modeling

can easily require hundreds of data points, which could mean months of intensive yet menial experimentation.

Automation could provide a valuable tool for accelerating kinetic analysis workflows in electrocatalysis. To date, most strategies for automation in electrocatalysis are tailored towards high-throughput catalyst or condition screening.[110,111] For example, one automation strategy involves miniaturization, where small (order microliter) electrolyte volumes are employed for rapid materials screening within scanning droplet cells.[112–114] However, with such small working volumes, it can be difficult to quantify reaction products; thus, these rapid screening techniques cannot be used to automate kinetic analysis of electrocatalytic reactions that do not have 100% Faradaic efficiency. Parallelization is another strategy, where arrays of different metal compositions or electrolyte conditions are tested simultaneously.[115–117] Parallel setups often do allow for product quantification, but quantification is typically performed either by aggregating effluents from multiple reactors or by manual work-up after electrolysis. An automated kinetic analysis workflow would ideally involve online product quantification of individual electrochemical cells, which is possible but likely to be expensive in a parallel configuration. Thus, a strategy involving sequential electrochemical testing and online product quantification of well-controlled reaction conditions within geometrically well-defined reactors would be ideal for automating kinetic analysis. This automation strategy has been used to screen catalysts for the (photo)electrochemical CO_2 reduction reaction (CO_2RR).[118–121] We demonstrate that a similar automation concept can be used to automate electrochemical kinetic analysis workflows.

In this work, we report an automated platform for both the collection and quantitative statistical analysis of electrochemical reaction rate data. To be more tailored toward the application of kinetic analysis, our robotic system automatically performs queued electrochemical experiments that can accommodate a different electrode, electrolyte, and gas-phase reactant for each individual experiment. This extent of operational versatility is not necessary for high throughput catalyst screening, but is essential for the kinetic analysis we sought to automate, which involves testing fresh electrocatalysts under a wide range of different operating conditions. Additionally, our experimental automation is integrated with an analysis software that increases the throughput of data processing, kinetic model fitting, and iterative experimental design.

We used this system to investigate the mechanism of carbon dioxide electroreduction (CO_2RR) to carbon monoxide (CO) at various immobilized metal tetrapyrroles. We first validated the

automated system with immobilized CoPc, where cohesive kinetic analysis of reaction data collected over a wide range of reaction conditions has previously been reported.[42] We then extended the kinetic analysis to additional metal tetrapyrroles commonly used as catalysts for CO_2RR to CO. Our analyses highlight that complex reaction mechanisms involving electrolyte adsorption and potential-dependent degrees of rate control are prevalent across this broad range of electrocatalysts.

3.2 Methods

3.2.1 Automated data collection

The robotic setup automates electrochemical testing in 1-compartment sandwich cells. Up to ten electrode/electrolyte samples can be loaded at one time, and the robot tests the ten samples sequentially (Figure 3-1A). In this work, the setup was used for carbon paper electrodes, aqueous electrolytes, and gas-phase quantification via an online gas chromatograph (GC).

For operation, the user performs the following actions:

1. Load carbon paper-based working electrodes into cell pans
2. Load 2 mL of electrolyte into inlet vials
3. Add electrolysis specifications to an excel queue file (e.g., applied voltage & duration)
4. Hit run

And the setup automates the following:

1. Read queue and initiate a run:
    a. Move cell body to desired cell pan
    b. Close the cell
    c. Fill electrolyte and flow gas
    d. Start electrolysis and GC data collection
    e. Wait for run to complete
    f. Collect electrolyte into collection vial and turn off gas
    g. Open the cell
    h. Move to wash station and rinse cell body
    i. Copy data files to a time-stamped folder and database the run
2. Continue reading queue entries until all are complete

Vertical and horizontal motion of the cell body are achieved with stepper motors (Fuyu), which are controlled by Silent Stepper Bricks (Tinkerforge). Electrolyte solution is pumped using peristaltic pumps (Kamoer), which are controlled using an Industrial Quad Relay Bricklet (Tinkerforge). Gas is flowed using a mass flow controller (Alicat), which is controlled with an RS232 Bricklet (Tinkerforge). Voltage is applied to the system using an SP300 potentiostat

(Biologic), which is controlled through python interfaces utilizing both the EC-lab development package and PyExpLabSys. Gas-phase products are quantified using a gas chromatograph (SRI) which is controlled using PeakSimple software and an Industrial Quad Relay Bricklet. All Tinkerforge bricks and bricklets are controlled from a python script.

3.2.2 Electrochemical cell design

A cell assembly consists of the cell body closed on top of two cell pans (Figure 3-1B). This assembly is analogous to a one compartment sandwich cell that houses a working, counter, and reference electrode. The working electrode, which takes the form of a circular, 13 mm diameter carbon paper disk, is clamped between the two cell pans once the cell is closed. This forces the working electrode into electrical contact with a conductive rod at the bottom of the cell pan that leads to a connection with the potentiostat. Once closed, only part of the working electrode (a circle of 1 cm diameter) is exposed to the electrolyte. The reference electrode is a 2 mm diameter leak-free Ag/AgCl reference (Innovative Instruments) that is inserted on the side of the cell body. The counter electrode is a 0.25 mm diameter platinum wire (Sigma Aldrich) inserted on a different side of the cell body. Gas phase reactants are sparged into the electrolyte near the electrode surface using 1/16" OD plastic tubing, and gas flows out of the top of the cell to the online GC for product quantification. Electrolyte is pumped in and out of the cell via two additional ports.

We note that this cell design does come with some considerations. First, because the working electrode is a plane and the counter is a wire, the distance between the counter and working electrodes is different for different locations on the working electrode. In principle, this can lead to spatial inhomogeneities in current flux along the surface of the working electrode. However, these effects are expected to be minimal at the high ionic strengths of 1 M salt used in this work. Please see supplemental discussion B.2.1 for more detailed discussion. Additionally, in a one-compartment cell, product, reactant, and even dissolved metal crossover between working and counter electrodes can cause issues. For example, oxygen evolved at the counter electrode could cross over to the working electrode and lead to parasitic oxygen reduction reaction (ORR) current. Based on our Faradaic efficiency closure, we expect this effect to be relatively minor (Section 3.3.1). Additionally, crossover of dissolved Pt from anode to cathode can lead to an increase in hydrogen evolution current over time, even when a separator is present.[38] This does not appear to be an issue in our system. [add control tests with glassy carbon anode] To conclude, even though these considerations are important to keep in

mind, they likely do not influence the conclusions of this work. In particular, we also benchmark against previous data collected within a geometrically symmetric, two-compartment cell to demonstrate robustness of results collected using this automated setup (*vide infra*).

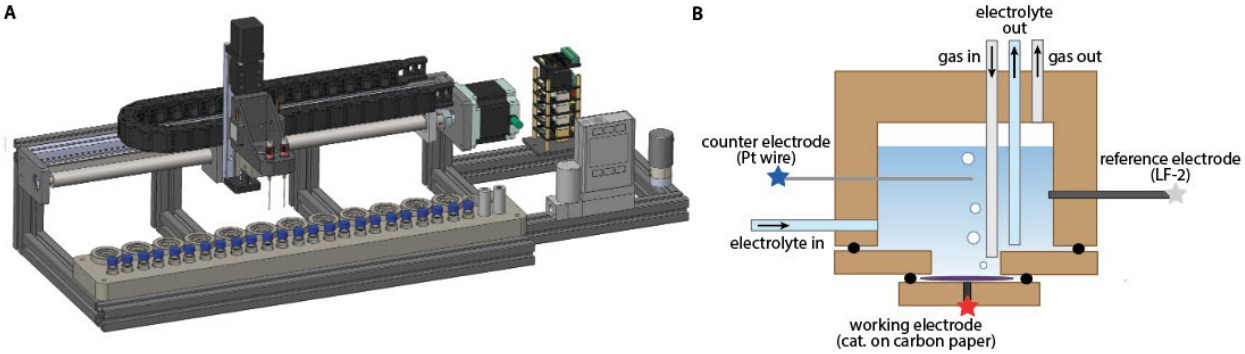

Figure 3-1. Schematic of robot for automated electrochemical kinetic data collection. **A**, CAD drawing of entire robotic system, with a single cell body that travels to different cell pans, each associated with an input and output electrolyte vial, to automatically perform experiments in sequence. **B**, schematic of the cell used.

3.2.3 Additional experimental details

Catalyst and electrolyte preparation closely followed what has been previously reported in the literature. Briefly, for CoPc, low loadings (below 6 x 10^{-11} mol/cm^2) of as-purchased CoPc were dropcasted, along with Nafion binder, onto carbon paper. For CoTPP, low loadings (below 8 x 10^{-10} mol/cm^2) of as-purchased CoTPP were dropcasted, along with Nafion binder and carbon black, onto carbon paper, also following a previously reported method.

Electrolytes were prepared by dissolving required amounts of $NaClO_4$ and Na_2CO_3 in milliQ water. Electrolytes were purged with CO_2 overnight upon preparation, and bubbled with CO_2 for at least 30 minutes prior to use.

Electrolyses were run for 50 minutes, and reported CO and H_2 partial currents correspond to the average of GC injections at the 20, 30, 40, and 50 minute marks. One hundred percent resistance compensation was manually applied with post-processing, where the solution resistance was measured to be 15 ohms (Figure 7-1).

3.2.4 Quantitative kinetic analysis

Bayesian parameter estimation was carried out using the previously described, Python-based julius package.[108] This package was also extended to aid in analysis of variance (ANOVA) model discrimination by calculating F-values.[75,76] In the coming weeks, we will extend this

code for additional functionality of recommending experimental conditions and quantifying model distinguishability.

3.3 Results

3.3.1 Data robustness

To assess the accuracy and robustness of rate data collected with the automated setup, we first measured the kinetics of CO_2RR to CO at cobalt phthalocyanine and compared against previously reported[42] rate data (Figure 3-2). Figure 3-2A through C show previously reported Tafel, bicarbonate, and CO_2 dependencies, manually collected in a 3-compartment cell, and Figure 3-2D through F show the same rate data collected using the automated setup. Visually, the non-linear and condition-dependent kinetic trends are preserved in the data collected with the automated setup. However, turnover frequencies measured with the automated setup are about 2-3 times lower those previously reported. This discrepancy is likely due to differences in gas flow geometry, where in the 3-compartment cell, CO_2 gas was flowed through the electrode, but in the automated 1-compartment cell, the CO_2 gas was sparged into the electrolyte. Further discussion can be found in Section B.2.2.

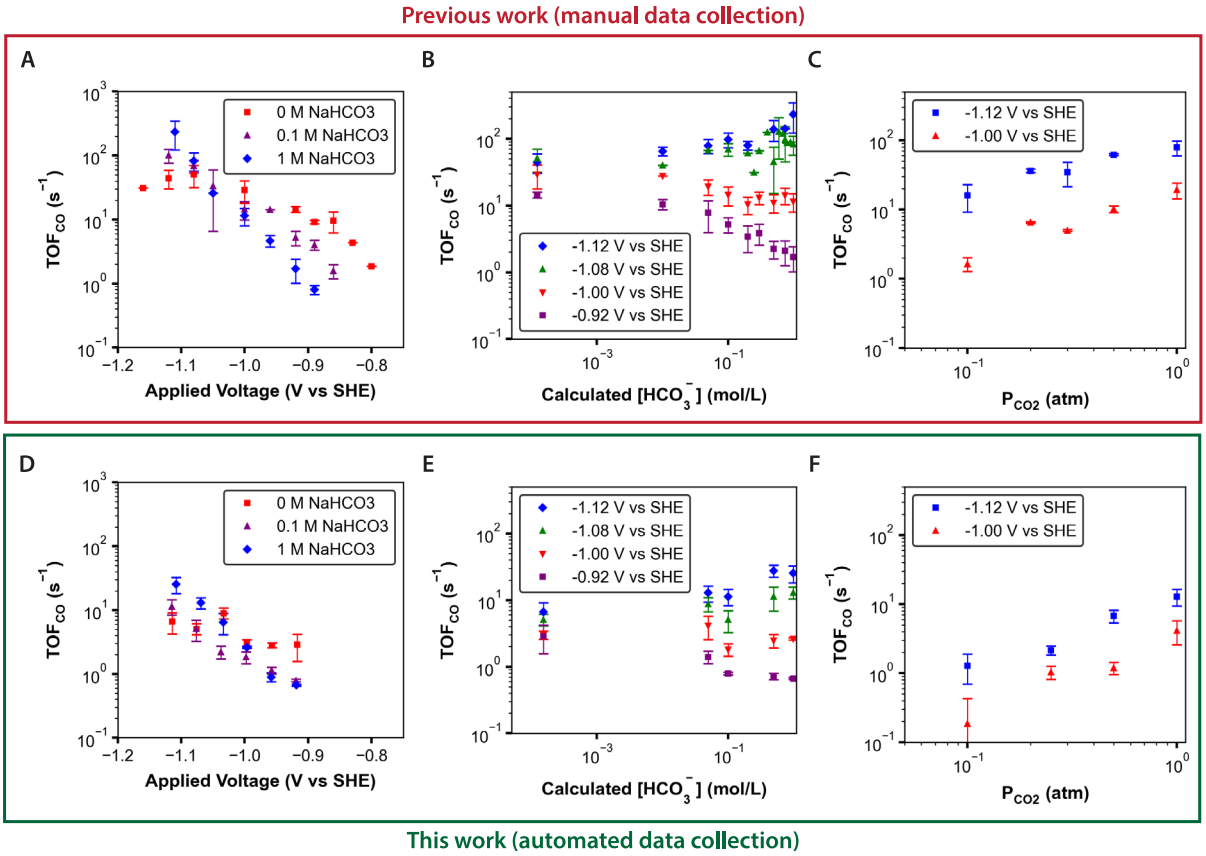

Figure 3-2. Benchmarking data collected with automated setup. **A-C**, Kinetic data for CO_2RR to CO at CoPc,

reprocessed from a previous work. Shown from left to right are Tafel, bicarbonate, and CO_2 dependences. **D-F**, same kinetic data, this time collected using the automated setup reported in this work.

3.3.2 Extension to cobalt tetraphenyl porphyrin

We next used the robotic setup to analyse the reaction mechanism at cobalt tetraphenyl porphyrin (CoTPP). As shown in Figure 3-3, the apparent bicarbonate order dependence at CoTPP suggests that bicarbonate poisoning may be occurring, particularly at less reductive potentials.

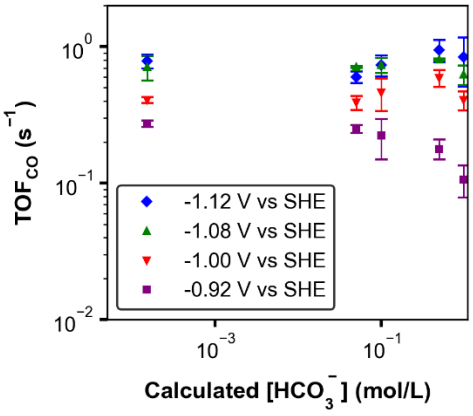

Figure 3-3. Bicarbonate order dependence collected with automated setup for CO_2RR to CO at cobalt tetraphenyl porphyrin.

3.4 Conclusion

Here we have demonstrated a robotic device for automated collection of kinetic data. Preliminary benchmarking against previous CO_2RR data at CoPc suggests that the data collected with this setup is robust. Specifically, trends in the kinetic data collected at CoPc are suggestive of both bicarbonate poisoning and potential-dependent changes in reaction mechanism. Additionally, kinetic data collected at CoTPP is also indicative of complex reaction mechanisms, and in particular, the preliminary evidence indicates bicarbonate poisoning is also a salient phenomena at CoTPP.

4 ELECTRIFYING C–C BOND FORMATION CATALYSTS

Content of this chapter adapted from following manuscript, under revision: **Zeng, J.**, Jiang, C., Adams, J., Delgado, S., Román-Leshkov, Y., Manthiram, K. Electrified C–C bond formation at hydroformylation catalysts.

4.1 Abstract

Hydroformylation (thermo-HFN) is an industrially important reaction that couples olefins and carbon monoxide (CO) to make aldehydes. If thermo-HFN were electrified to use protons and electrons instead of hydrogen gas, such an electrochemical hydroformylation (electro-HFN) reaction could be useful in the context of electrified chemicals manufacturing for functionalizing abundant olefins to synthetically versatile aldehydes. Additionally, electro-HFN could provide a method for sequentially elongating carbon chains in the context of electrochemical CO_2-to-fuels conversion. However, electro-HFN represents a complex C–C bond-forming reaction that is difficult to achieve at heterogeneous electrocatalysts. In this work, we import Rh-based thermo-HFN catalysts onto electrode surfaces to unlock electro-HFN reactivity. At mild conditions of room temperature and 5 bar CO, we achieve Faradaic efficiencies of up to 15% and turnover frequencies of up to 0.7 hr^{-1}. This electro-HFN rate is an order of magnitude greater than the corresponding thermo-HFN rate at the same catalyst, temperature, and pressure. Reaction kinetics and *operando* spectroscopy evince an electro-HFN reaction pathway that is fundamentally distinct from thermo-HFN. Most generally, this work demonstrates an experimental strategy for electrifying a well-studied thermochemical reaction to expose a new electrocatalyst for a difficult and underexplored electrochemical reaction.

4.2 Introduction

Electrochemical reactions leverage voltage as a driving force that can be highly potent and renewably sourced. Thus, electrified manufacturing is envisioned to provide more sustainable routes to important fuels and chemicals.[1] However, many industrially important reactions lack

well-developed electrochemical alternatives. For example, carbon–carbon (C–C) bond formation between olefins and carbon monoxide (CO) is a highly versatile reaction that remains underexplored in electrocatalysis. In the context of chemicals manufacturing, the reaction that achieves this reactivity is hydroformylation (thermo-HFN), which adds CO and H_2 to olefins to generate aldehydes (Figure 4-1a). Because olefins are some of the highest volume bulk chemicals[122] and aldehydes are versatile intermediates for many products such detergents and plastics,[122–125] thermo-HFN is performed at a global scale of over 10 million tons/year.[122–124] Additionally, in the space of electrochemical CO_2 to fuels conversion, C–C bond formation is a critical reaction for carbon chain extension. Specifically, C–C bond formation between olefins and CO could provide a way to electrochemically couple ethylene and CO, which are common products of electrochemical CO_2 reduction (CO_2RR),[126] to achieve C_{3+} products, which remain relatively harder to achieve in CO_2RR.[7–9]

However, forming C–C bonds between olefins and CO is challenging in heterogeneous electrocatalysis, despite its relevance to both electrified chemicals and fuels syntheses. Related reactivity is thought to be useful for forming three-carbon (C3) products during CO_2 electroreduction, but even at state-of-the art Cu-based catalysts,[127,128] the complex mixture of products formed has made it challenging to both understand reaction mechanisms and design catalysts that steer selectivity to one product.[126,127,129] Electrochemical hydroformylation (electro-HFN), in which protons and electrons replace the hydrogen gas used in thermo-HFN (Figure 4-1a), would be an ideal reaction to cleanly achieve C–C bond formation, but this reaction remains highly underdeveloped. To our knowledge, only one instance of electro-HFN was reported in 1997, and the work featured spontaneous half reactions that required elevated temperature and H_2 as a reactant; additionally, external applied voltage was not able to improve the observed reactivity.[130] Thus, there remains a need for catalysts that that can facilitate directly voltage-driven C–C bond formation between olefins and CO.

We hypothesized that catalysts for electro-HFN could be designed using precedent from thermo-HFN catalysis. We show that electrifying a working thermo-HFN catalyst reveals a reaction system that is able to access two chemically similar reactions driven by either voltage (i.e., electro-HFN) or H_2 gas (i.e., thermo-HFN). Within such a system, we show that the additional handle of applied voltage in electro-HFN can mitigate the need for elevated temperatures (90 – 120 ^{o}C), as well as the use of H_2 gas, typically required for thermo-HFN.

4.3 Sequentially electrifying thermo-HFN

We sequentially electrified thermo-HFN by implementing changes to typical organometallic thermo-HFN systems that would make them more amenable for heterogeneous electrocatalysis. This involved synthesizing heterogenized catalytic sites, using ionically conductive reaction media, and depositing catalysts on electrode surfaces (Figure 4-1a).

For heterogenized sites, we followed literature precedent showing that Rh atoms on metal oxide supports are active for hydroformylation.[131,132] We used wetness impregnation to deposit 1.8 wt% Rh (as determined by inductively coupled plasma mass spectrometry (ICP-MS)) onto ~20 nm sized cerium (IV) oxide nanoparticles (Figure A-C5a). The final powder catalyst, referred to as Rh@CeO_2, was confirmed to be active for thermo-HFN of a model styrene substrate under typical thermo-HFN conditions:[131] octane solvent, 80 ºC, 5 bar CO, and 5 bar H_2 (Figure A-C5b).

We then moved to protic and ionically conductive solvent conditions that would eventually be required for electro-HFN. For the solvent, we found that mixtures of water and alcohols allowed thermo-HFN to proceed relatively unaffected, whereas other common solvents for organic electrochemistry, such as acetonitrile and N,N-dimethylformamide, interfered with reactivity (Figure A-C5b). For the salt and proton source, we saw favorable reactivity in the presence of triflate-containing salts and acids, particularly tetrabutylammonium triflate (TBAOTf) and triflic acid (HOTf) (Figure A-C5c). We speculate that enhancement from triflate is due an increase in lability of Rh-surface bonds that increases the availability of empty coordination sites at Rh for catalysis (Section C.2.5).[133]

Finally, we deposited the Rh@CeO_2 catalyst, along with carbon black and Nafion, onto carbon paper electrodes. Electro-HFN was performed in a two-compartment electrochemical cell with no H_2 gas supplied (Figure 4-1b). We first performed electro-HFN at elevated temperatures (80 ºC) and pressures (5 bar), to parallel typical thermo-HFN conditions (Figure A-C5d). However, we found that electro-HFN rate and selectivity actually improved at 25 ºC (Section C.2.1). Thus, our following discussions focus on experiments at ambient temperature.

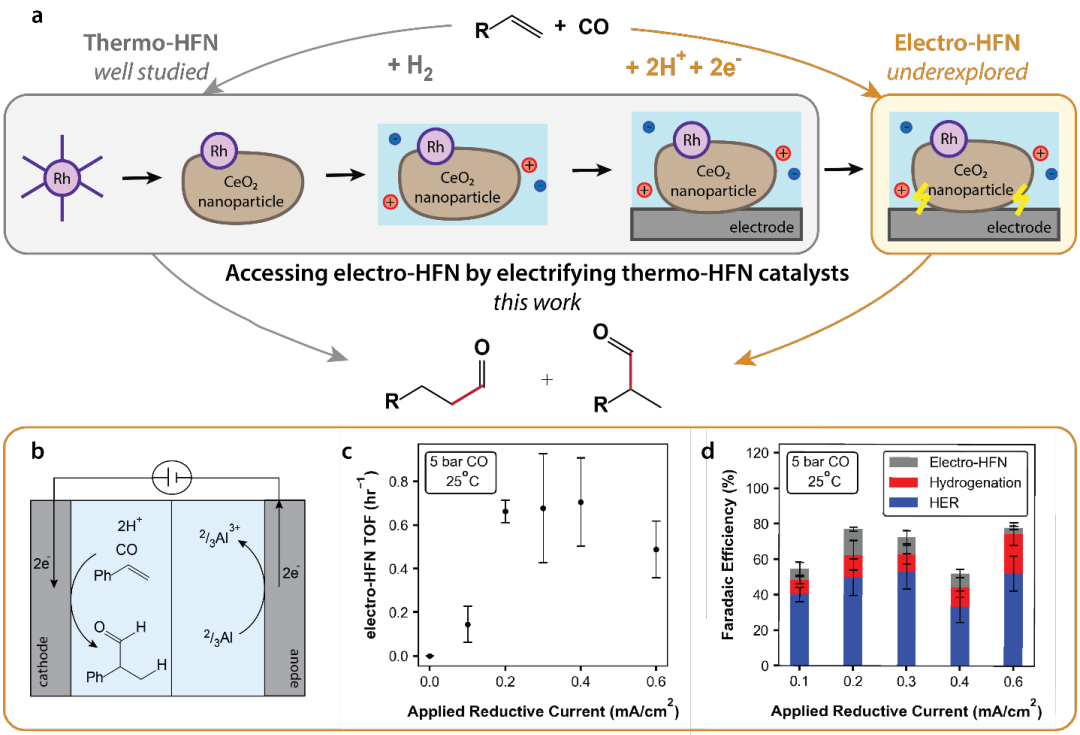

Figure 4-1. Electrifying a thermo-HFN catalyst to access electro-HFN reactivity. **a**, thermochemical and electrochemical hydroformylation (HFN) reactions. In this work, a thermo-HFN catalyst was sequentially electrified to achieve electro-HFN. **b**, schematic of the two-compartment electro-HFN cell configuration. **c**, electro-HFN rate, or turnover frequency, as a function of applied reductive current. **d**, electro-HFN product distribution, given as Faradaic efficiency, as a function of applied reductive current. All data was collected at 25 °C, 5 bar CO, 0.52 M styrene, 0.1 M TBAOTf, 25 mM HOTf in a 50% v/v IPA/H_2O mixture. Error bars represent standard deviation with $n \geq 3$.

4.4 Demonstration of electro-HFN

Electro-HFN of styrene at ambient temperature (25 °C) yielded the branched aldehyde product 2-phenylpropanal. During galvanostatic experiments at 5 bar CO, the turnover frequency (TOF), or rate per site (approximated with the total number of Rh atoms deposited), of electro-HFN reached a maximum of ~ 0.7 hr^{-1} at an applied current of -0.4 mA/cm^2 (Figure 4-1c). This TOF was significantly higher than that of thermo-HFN under similar conditions: replacing applied current with 5 bars of H_2 gas (for a total of 10 bar syngas) led to a TOF of less than 0.02 hr^{-1} (Figure A-C6a). The maximum observed Faradaic efficiency (FE), or selectivity per electron, for electro-HFN was ca. 15%, which was observed at -0.2 -0.4 mA/cm^2, where other major side reactions included hydrogenation to yield ethylbenzene (13% FE) and hydrogen evolution (HER) (50% FE) (Figure 4-1d). At 25 °C, we did not observe the linear aldehyde 3-phenylpropanal.

We then confirmed that electro-HFN activity was occurring at heterogeneous sites, because heterogeneous thermo-HFN catalysts can suffer from metal leaching.[134] Although we did detect leached Rh in the electrolyte after electrolysis (up to 2% of deposited Rh after 2 hours via ICP-MS, Figure A-C7a), an electrochemical "filtration test" suggests that the dissolved Rh species do not significantly contribute to catalysis: halfway through an electrolysis, swapping out the catalyst-containing electrode with a blank carbon paper and reusing the same electrolyte completely stopped reaction progress (Figure A-C7b).

Next, we confirmed which reactions were associated with Rh active sites by measuring the rate of electro-HFN, as well as those of the major side reactions (i.e., hydrogenation and HER) as a function of Rh@CeO_2 particle loading. We found that both electro-HFN and HER rates monotonically increased with increasing particle loading, whereas hydrogenation rates decreased with particle loading (Figure A-C7c). Electrodes with bare CeO_2 nanoparticles or with only carbon black were active for hydrogenation and HER but not for electro-HFN (Figure A-C7d). These results suggest that electro-HFN principally occurs on Rh-containing sites, but that the same is not necessarily true for HER and hydrogenation. Our observation that hydrogenation is mostly associated with a site different from that of electro-HFN is in surprising contrast with what is understood for thermo-HFN, where hydrogenation is a side pathway within the hydroformylation mechanism.[123,124,135]

Finally, we examined whether electro-HFN occurs via an indirect mechanism, where the role of applied voltage would simply be to generate H_2 gas that then reacts in the thermo-HFN pathway. If this indirect mechanism were the case, we would expect that at the same local CO and H_2 activities, the electro-HFN rate should equal the thermo-HFN rate. However, we observed across several experiments that under similar reaction conditions, the rate of electro-HFN was significantly faster than that of thermo-HFN. For example, the maximum electro-HFN rate observed at 5 bar (pure CO) was over 10x higher than the observed thermo-HFN rate at 5 bar CO/5 bar H_2 (*vide supra*). Additionally, feeding 0.5 bar CO/0.5 bar H_2 while applying voltage resulted in observable product whereas flowing the same gas mixture with no applied voltage resulted in no observable product (Figure A-C6b). It is worth noting these observations could still be consistent an indirect mechanism if (1) local H_2 accumulation during electro-HFN significantly exceeded the H_2 pressure supplied during the thermo-HFN reactions described above, or (2) applied voltage non-Faradaically promotes thermo-HFN. Analysis of H_2 transport shows that at the reported current densities, local H_2 accumulation cannot account for the above observations (Section C.2.3). We also did not find evidence for the second

possibility of non-Faradaic promotion. We first tested whether applied voltage was only needed to activate the catalyst to a reactive state (e.g., help to generate surface hydrides necessary to enter a catalytic cycle) by feeding 0.5 bar CO/0.5 bar H_2 and only applying voltage for the first 5 minutes of the reaction; we did not observe product (Figure A-C6b). Additionally, at elevated temperatures where the rate of thermo-HFN exceeded that of electro-HFN, we saw no evidence of non-Faradaic promotion upon the application of voltage (Figure A-C8 and Section C.2.2).

4.5 *Operando* catalyst characterization

We used X-ray absorption spectroscopy (XAS) at the Rh K-edge to characterize Rh valency (via X-ray absorption near edge structure, or XANES) and Rh coordination (via extended X-ray absorption fine structure, or EXAFS) under both *ex situ* and *operando* conditions. [136]

Ex situ measurements on the as-synthesized catalyst show the presence of hexacoordinate Rh(III). The XANES spectrum of the Rh@CeO_2 catalyst is similar to that of a Rh_2O_3 standard, suggesting similar Rh oxidation states of +3 (Figure 4-2a). The Rh@CeO_2 EXAFS spectrum shows a strong contribution from a first shell Rh-O scattering path with no visible Rh-Rh scattering contribution (Figure 4-2c). EXAFS fitting[137] of the Rh-O scattering path shows that, within fitting error, both the Rh@CeO_2 powder catalyst ($CN_{Rh\text{-}O}$ = 5.8 ± 1.5) and the Rh_2O_3 standard ($CN_{Rh\text{-}O}$ = 6) have the same Rh-O coordination number. These observations could be consistent with either small Rh_2O_3 clusters or single Rh(III) atoms on the ceria surface. Literature precedent suggests that at ~2 wt% loadings, Rh deposited on similar metal oxide nanoparticles yields small clusters.[138] In either case, the as-synthesized Rh(III) sites appear to be fully coordinated to either lattice or ligand oxygen atoms.

Operando measurements show that on average, the Rh@CeO_2 catalyst remains as Rh(III) but coordinates fewer oxygen atoms under reaction conditions. *Operando* XANES shows that under operating conditions with all reactants present, the Rh K-edge energy still reflects a Rh(III) oxidation state and does not change substantially in response to applied potential (Figure 4-2b, red triangles).The Rh(III) assignment is in surprising contrast to the expected Rh(I) state that is expected from both homogeneous and heterogeneous thermo-HFN precedent.[123,135,139] *Operando* EXAFS shows that the Rh-O coordination number decreases to around 4.5 – 5 under reaction conditions, which suggests availability of open sites for catalysis (Figure 4-2c and Figure 4-2d). We found no changes in fitted Rh-O bond lengths with applied potential (Figure A-C9b). Notably, we did find that the response of Rh valency to applied potential is highly dependent on which reactants are present. When neither CO nor styrene are

present, the Rh K-edge energy responds to applied potential (Figure 4-2a and Figure 4-2b), and does so in an irreversible fashion (Figure A-C9a). However, addition of CO attenuates the voltage response and addition of styrene eliminates the voltage response (Figure 4-2b). That Rh valency does change in response to applied potential under certain conditions shows that at least some fraction of the Rh sites are electrochemically accessible. Thus, the *operando* XAS data suggest that the resting state of the Rh catalyst is in a +3 oxidation state, coordinated to 4-5 oxygen ligands, electrochemically accessible, and not strongly perturbed by changes in applied potential.

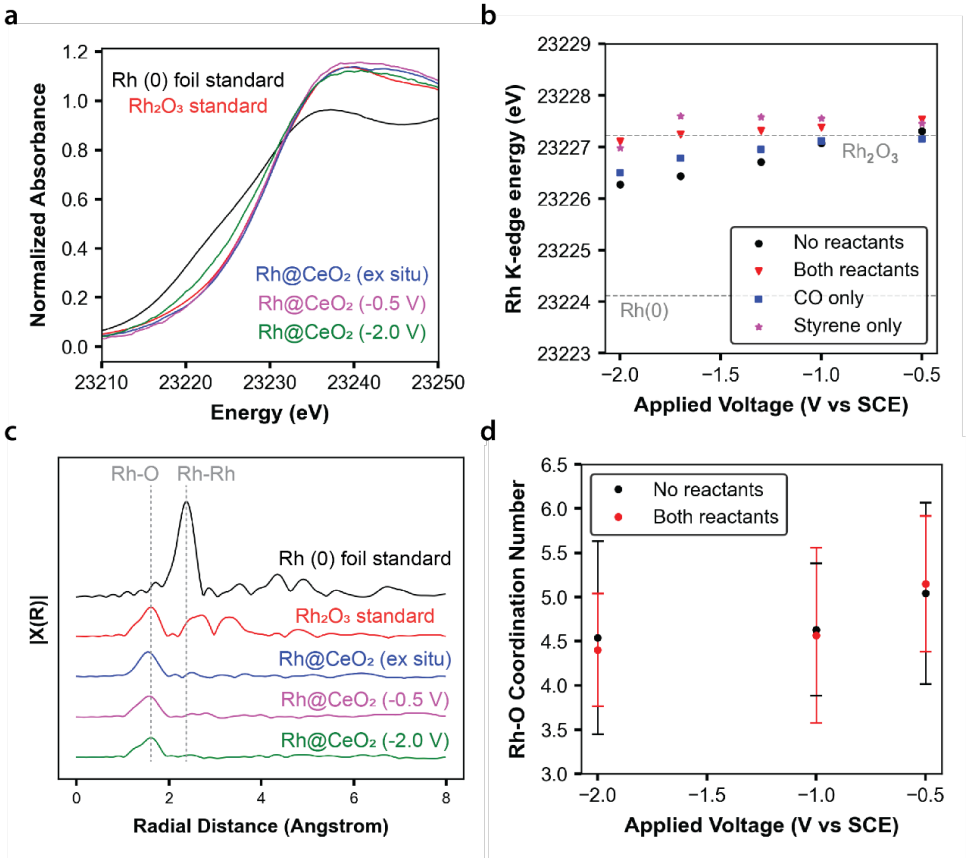

Figure 4-2. X-ray absorption spectroscopy. **a**, normalized XANES data zoomed in on rising edge, shown for *ex situ* and *in situ* samples, as well as known rhodium-containing standards. **b**, processed *in situ* XANES data showing Rh K-edge energy as a function of applied potential under various conditions with and without reactants. **c**, R-space EXAFS spectra of *ex situ* and *in situ* samples, as well as known rhodium-containing standards. **d**, processed *in situ* EXAFS data showing fitted Rh-O coordination numbers as a function of applied potential, with and without reactants. Error bars in **d** represent fitting errors given by the Artemis fitting software. All data collected at ambient temperature and pressure in electrolyte composed of 0.1 M TBAOTf and 25 mM HOTf in IPA/H_2O. The representative *in situ* samples shown in **a** and **c** were collected without styrene or CO present. Voltages reported vs SCE.

4.6 Electrochemical kinetic analysis

To further interrogate the reaction mechanism, we collected electrochemical kinetic data via potentiostatic experiments at ambient pressure. We measured Tafel (voltage) dependence as well as CO, styrene, and proton dependences at both less reductive (-1.05 V vs SCE) and more reductive (-1.45 V vs SCE) potentials. We assumed steady-state rates, which we confirmed with time dependence experiments (Figure A-C10a).

The Tafel data of electro-HFN show a weak voltage dependence that attenuates at more reductive potentials (Figure 4-3a). Fitting the points at the least reductive potentials yields a Tafel slope around 170 mV/dec, and fitting the most reductive potentials yields a slope around 530 mV/dec. This saturation behavior is unlikely caused by mass transport limitations, since the measured currents are below 1% of the predicted transport limited current density (Section C.2.4). For CO, rates increase sublinearly ($n_{CO} = 0.6 \pm 0.1$) with CO pressure at more reductive potentials and linearly ($n_{CO} = 1.3 \pm 0.3$) at less reductive potentials (Figure 4-3b). Across most of the conditions tested, the styrene dependence of electro-HFN is approximately linear at both more reductive ($n_{sty} = 0.9 \pm 0.3$) and less reductive ($n_{sty} = 0.6 \pm 0.4$) potentials (Figure 4-3c). We also observed a sharp increase in electro-HFN rate at the highest styrene activities that were tested, which may be associated with phase separation that occurs in those conditions. Finally, for proton dependence, the reaction displays sublinear dependence ($n_{H^+} = 0.3 \pm 0.1$) at more reductive potentials, and at less reductive potentials, displays a complex dependence that appears to be proton independent ($n_{H^+} = -0.1 \pm 0.1$) in the operationally relevant regime, and negative at higher proton concentrations (Figure 4-3d). Similar kinetic data for the hydrogenation and HER side reactions, as well as total current, are presented inFigure A-C11, Figure A-C12, and Figure A-C13. A summary of apparent Tafel slopes and rate orders for all three reactions is provided in Figure A-C14.

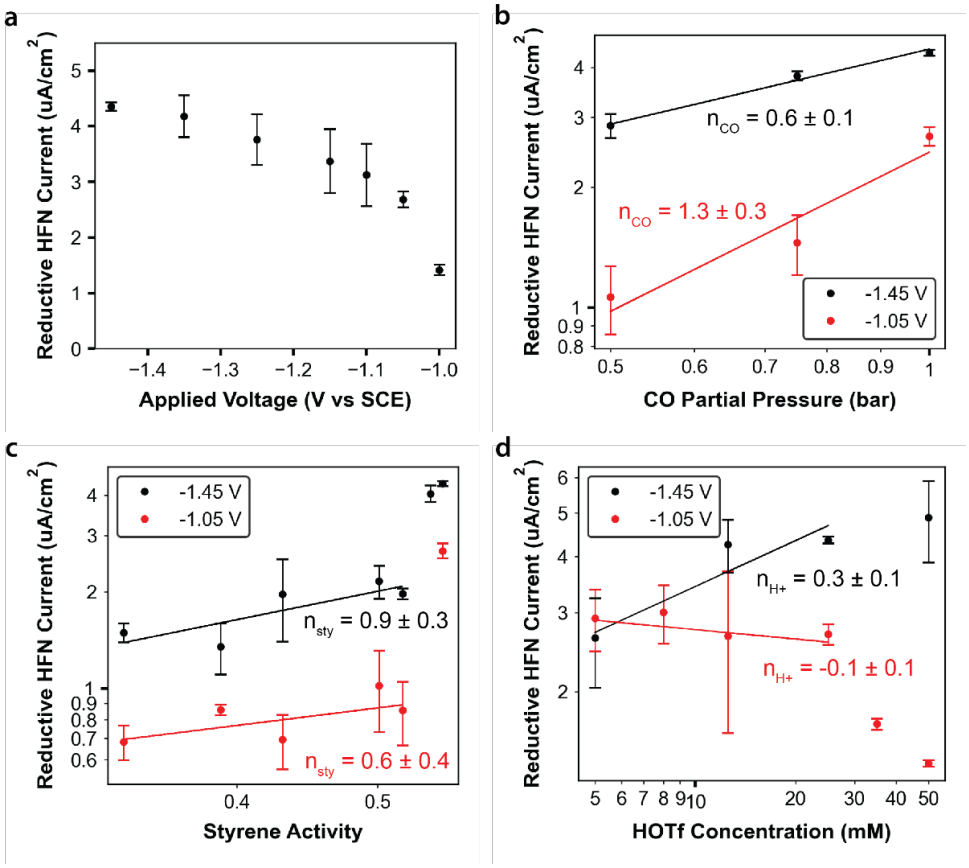

Figure 4-3. Kinetic data on electro-HFN at ambient temperature and pressure. **a**, voltage dependence. **b**, CO partial pressure dependence. **d**, Styrene activity dependence. **e**, acid concentration dependence. Panels **b** – **d** plotted on log-log scales with data at higher driving forces (-1.45 V vs SCE) in black, and data at lower driving forces (-1.05 V vs SCE) in red. All data was collected at 25°C, 1 bar CO, 0.52 M styrene, and 25 mM HOTf, in a 50% v/v IPA/H_2O mixture, unless explicitly labeled otherwise. Error bars represent standard deviation with n ≥ 3.

A mechanistic hypothesis qualitatively consistent with the presented observations is illustrated in Figure 4-4. The proposed electro-HFN mechanism is similar to thermo-HFN mechanisms that have been suggested in both the homogeneous[123,124] and heterogeneous[130,131,135,139] literature. These mechanisms include olefin coordination (**1**→**2**) and hydride insertion (**2**→**3**) to form a Rh–alkyl (**3**), followed by CO coordination and migratory insertion (**3**→**4**) to form a Rh–acyl (**4**). We propose that **1** is the most abundant reactive intermediate and that the aforementioned steps are in pre-equilibrium, which is consistent with the approximately linear order dependencies observed for CO and styrene. From the Rh–acyl, we propose that a hydride is generated on the Rh site via an electron transfer (ET, **4**→**5**) step followed by a proton transfer (PT, **5**→**6**) step. Mixed control between the ET and PT could give rise to the observed Tafel and proton dependences. Specifically, at less reductive potentials, the stronger potential dependence (m_T ~170) and weaker proton dependence (n_{H+} ~0) could be consistent with the

ET step having a higher degree of rate control. At more reductive potentials, where the ET step should be more facile, the weaker potential dependence (m_T ~500) and higher proton dependence (n_{H+} ~ 0.3) are consistent with the PT step having a higher degree of rate control. This would also be associated with greater coverages of (**5**). Consistent with this proposed mechanism, we also observe a larger kinetic isotope effect (2.8 ± 0.5) at -1.45 V, where the PT is proposed to have a higher degree of rate control, than at -1.00 V (1.5 ± 0.2) (Figure A-C10b). Finally, after formation of species **6**, we propose that facile addition of a proton and electron, as well as desorption of the aldehyde product, complete the catalytic cycle. We loosely hypothesize that the Rh sites may dynamically coordinate and decoordinate lattice oxygens throughout this catalytic cycle, which would allow Rh to expose empty coordination sites and access chemically reasonable oxidation states (i.e., Rh(I/III)) throughout the proposed cycle (Section C.2.5).

Although the proposed mechanism is just one possible explanation of the kinetic data, we posit that our observations do more strongly exclude several mechanistic possibilities. First, our observation that proton dependence is stronger where potential dependence is weaker and vice versa makes it very unlikely that the rate-limiting step is a concerted proton-electron transfer (**4→6**, or P2). Other mechanistic possibilities that we exclude based on previous observations (*vide supra*) include (1) an indirect mechanism where H_2 gas is generated as an intermediate (P1), and (2) hydrogenation reactivity occurring as a side reaction along the hydroformylation pathway (P3). All three excluded mechanistic features are also illustrated in Figure 4-4. Further mechanistic discussion is provided in Section C.2.6.

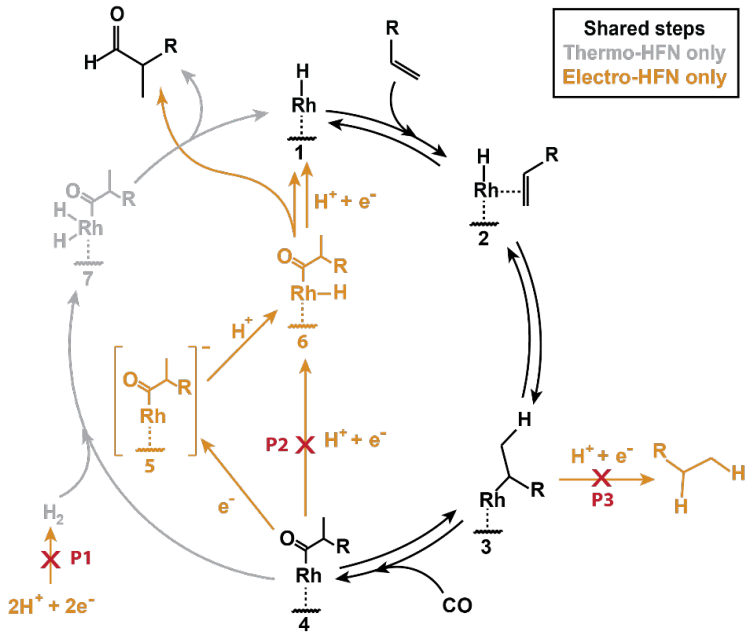

Figure 4-4. Mechanistic hypotheses. Steps from previously proposed thermo-HFN mechanisms are shown in black and grey, and additional pathways involving applied voltage are shown in yellow. Black paths show steps that are proposed to be shared between the thermo- and electro- HFN mechanisms. Excluded hypotheses are indicated with a red cross. Although not illustrated, these surface Rh species are likely dynamically coordinated to up to 5 additional lattice oxygen atoms.

4.7 Discussion

In this work, we first show that there are catalysts competent for both thermo- and electro-HFN, which is in contrast to what had previously been observed.[130] This insight is important because it allowed us to use known thermochemical reactivity as an experimental starting point for designing a new electrocatalyst, which is a design principle with limited, if any, precedent. We note that catalysts competent for both the thermo- and electro- catalytic versions of the same reaction have been reported in many contexts including CO_2 hydrogenation,[140] hydrogen oxidation,[141] carbon monoxide oxidation,[142] oxygen reduction,[143–146] hydrogenation,[147] and nitrate reduction.[148] However, these works are typically limited to oxidations or reductions of small molecules, and typically both the electro- and thermo- chemical reactions are already independently well-studied. Our work adds to this by demonstrating how the thermo- electro-catalysis divide can be experimentally traversed to expose relatively complex and underexplored C–C bond formation reactivity.

Importantly, we also argue that electro-HFN is mechanistically distinct from thermo-HFN. Therefore, our electrified hydroformylation analog is fundamentally different from previously reported electrified analogs of other organometallic thermochemistries[149] such as oxidative C-

H activation[150,151] and reductive cross-coupling.[152,153] In these other systems, catalysis occurs at a homogeneous site, and voltage indirectly participates in catalysis. Specifically, voltage replaces a sacrificial reductant or oxidant, and its role is to perform outer sphere electron transfer to generate an active species (such as regenerating an active Ni species)[152,153] that then thermochemically participates in known catalysis. Thus, it was not obvious that we would observe a change in reaction mechanism upon electrifying hydroformylation catalysts.

This mechanistically distinct and directly voltage-driven pathway has several important implications. First, from a practical perspective, we show that accessing electrochemical pathways can lead to practical improvements in reactivity at milder reaction conditions. Thermo-HFN is typically performed at elevated temperatures (90 – 120ºC), and the voltage-driven pathway may enable operation at milder temperatures. For a comparison of rates in the broader literature, heterogeneous thermo-HFN rates are not reported at room temperature, presumably because the catalysis is too sluggish.[131,132,135,154,155] The rates we observe are not yet competitive with those reported for homogeneous thermo-HFN at ambient temperature,[156,157] but bringing parity between heterogeneous and homogeneous systems is a known challenge in hydroformylation chemistry. Additionally, because thermo-HFN with H_2 gas is exergonic, the equilibrium potential of electro-HFN occurs at a less reductive potential than that of HER. Thus, a direct electro-HFN reaction could be more energy efficient than a thermo-HFN process that uses HER-derived H_2. However, we note that the voltages reported in this work are still ~1 volt more reductive than those required for HER, so further reaction optimization will be a subject of future work (Section C.2.7).

From a fundamental standpoint, the different mechanism that electro-HFN exposes could allow for different catalyst design principles. For example, an electro-HFN catalyst does not need to activate H_2 to generate hydrides; it simply needs to accept protons and electrons to do so. Thus, electro-HFN catalysts could be further optimized for earlier steps in the hydroformylation cycle such as olefin activation or C–C bond formation without being constrained by the need to activate H_2. Additionally, we observed that in some reaction conditions, Rh valency changed with applied potential. This suggests that voltage might also be useful as a handle to change catalyst electronic structure, which adds an additional design handle to those of ligand and support identity that are typically used in thermocatalysis. Thus, the framework of electrifying promising thermocatalysts described in this work may provide a useful strategy for developing voltage-driven reactions that simultaneously improve upon known thermochemical reactivity and expand the electrochemical reaction toolkit.

4.8 Methods

Catalyst synthesis. CeO_2 nanoparticle synthesis was adapted from the literature.[131] 2 g of Cerium(III) nitrate hexahydrate (Beantown Chemical, 128635) was ground with mortar and pestle, put in a combustion boat, and calcined under nitrogen flow at 350 ºC for 2 hrs in a tube furnace. The resulting light yellow solid was ground again with mortar and pestle and stored for later use.

Rh@CeO_2 was synthesized via a wet impregnation procedure that was adapted from the literature.[131] In summary, 1 g of CeO_2 powder was combined with 99 mg of Rhodium (III) acetylacetylonate (97%, Sigma Aldrich 282774) and approx. 3 mL of acetone in a heated (~80 ºC) mortar. The rhodium salt dissolved completely in acetone, and the mixture was ground with a pestle until all of the acetone evaporated. The resulting powder was transferred to a combustion boat, dried at 80 ºC for 30 minutes, and transferred to a muffle furnace, where it was heated in static air at 800 ºC for 10 hours with a 10 ºC/min ramp rate.

Rh loading quantification. Actual Rh loading in the Rh@CeO_2 catalysts was determined following a previously reported procedure involving acid digestion followed by ICP-MS.[132] In short, around 5 mg of the powder catalyst was mixed with 5 mL of aqua regia (1 mL of concentrated HNO_3 added to 4 mL of concentrated HCl). The sample was then digested in a sealed, Teflon-lined Parr digestion vessel at 80 ºC for more than 48 hours. The sample was then diluted into a 2% nitric acid solution, and terbium was added as an internal standard. Finally, the sample was filtered with a 0.22 um polypropylene syringe filter (ThermoFisher Scientific, CH2213-PP), and the Rh concentration was quantified using an ICP-MS (Agilent 7900 ICP-MS).

Electrode preparation. Toray 120 carbon paper (Fuel Cell store, 5% wetness proofing) was punched into 13 mm diameter circles and calcined in a muffle furnace in static air at 600 ºC for 1 hour. The muffle furnace treatment partially oxidizes the carbon paper surface to make it more hydrophilic.

A catalyst dispersion solution containing solvent, nafion (ionically conductive binder), and carbon black (conductive additive) was prepared by mixing the following: 13.2 mL isopropanol, 6 mL of Nafion 117 solution (5% in alcohols and water, Sigma Aldrich 70160), and 64 mg of carbon black (Vulcan XC 72, Fuel Cell Store).

Catalyst ink solutions were prepared by mixing Rh@CeO_2 powders with the above catalyst dispersion solution in a ratio of 60 mg Rh@CeO_2 to 960 uL of catalyst dispersion solution. The resulting catalyst ink solution was shaken and sonicated for ~5 minutes until it visually appeared well-dispersed and was then drop-casted onto hydrophilic carbon paper supports at a loading of 5 mg Rh@CeO_2 per carbon paper (for a loading of 3.77 mg Rh@CeO_2 per cm^2 electrode). To achieve this, approximately 35 uL of the catalyst ink solution was dropcasted on each side of the carbon paper support. Electrodes were dried at 80 ^oC for 30 minutes and then annealed at 150 ^oC for 6 hours. The final annealing step was roughly based off of nafion membrane annealing literature.[158]

Electrolyte preparation. The default electrolyte mixture used in these studies was a 50/50 v/v% water/isopropanol mixture with 0.1 M tetrabutylammonium trifluoromethanesulfonate (TBAOTf, Sigma Aldrich 86888) and 0.025 M trifluoromethanesulfonic acid (HOTf, Sigma Aldrich 347817). Directly prior to performing a reaction, this electrolyte was combined with styrene (Sigma Aldrich, S4972) to afford 0.52 M styrene in the electrolyte solution. Notably, 0.52 M styrene is above the solubility limit, so the final electrolyte was cloudy with a small amount of phase separation. During order dependence studies, the styrene and HOTf concentrations were changed accordingly. During kinetic isotope effect studies, water, isopropanol, and triflic acid were substituted with deuterium oxide (Sigma Aldrich, 151882), isopropanol-D8 (Sigma Aldrich, 175897), and DOTf (Sigma Aldrich, 369632), respectively.

Electrolyte activity characterization. For styrene order dependence studies, the activity of styrene was experimentally measured using previously reported methods.[159] Measured styrene activities are reported in Figure A-C3a. To quantify proton activity, reversible hydrogen electrode (RHE) potentials for electrolytes with different HOTf concentrations were also measured using methods based on literature.[57,160,161] In short, RHE was determined by measuring steady-state open circuit voltage (OCV) a Pt/C carbon electrode with 1 atm of H_2 gas bubbling. Measured RHE potentials are reported in Figure A-C3b.

Thermochemical reaction setup. Thermochemical HFN reactions were performed in 350 mL Parr reactors. All thermochemical measurements were intentionally performed such that parameters such as catalyst loading/preparation, electrolyte, reactant concentration, etc., were directly comparable to electrochemical reactions.

In short, one catalyst-covered carbon paper electrode was added to a 25 mL round bottom flask, in addition to 1 magnetic stir bar and 2 mL of electrolyte solution. This round bottom flask was

placed within the Parr reactor, and the Parr was then sealed. Then, the Parr reactor was purged with nitrogen gas. Afterwards, 3 pump-purge cycles were performed with CO in which the reactor was charged to 5 bar CO (Airgas CM R300), then purged, and this process was repeated for a total of 3 times. Then on the fourth pump step, the reactor was left at 5 bar CO. Subsequently, the reactor was then connected to an H_2 (Airgas HY UHP35) line and filled to the appropriate pressure of H_2 (typically 5-10 bar H_2 for a total pressure between 10-15 bar). The reactor was then left on a magnetic stir plate, typically overnight, to allow the reaction to occur (typically 14-16 hrs). Upon completion of the reaction, the gas was released, reactor purged with N_2, and reaction mixture within the flask was worked up (*vide infra*).

Electrochemical reaction setup. Electrochemical measurements were performed in PEEK sandwich cells (Custom-made, Lab Machinist Solutions) in a 2-compartment configuration. Aluminum foil (Reynold's Wrap) was used as the sacrificial counter electrode, Neosepta AHA membranes (Ameridia Innovative Solutions, stored in milliQ water and rinsed with IPA before use) were used as the separator, and when applicable, a leak-free Ag/AgCl electrode (Innovative Instruments LF-2) was used as the reference electrode. Anode and cathode compartments were filled with 2 mL of electrolyte solution each. A miniature magnetic stir bar was also added to the cathode compartment. Seals were made with chemically resistant Viton O-rings (McMaster-Carr 1170N32/1170N26). All structural components for the 2-comparment cells are shown in a blown-out view in Figure A-C1a. They were assembled as shown in the steps illustrated by Figure A-C1b. Between experiments, all parts were rinsed thoroughly with acetone and a new catalyst electrode and membrane were used for each experiment.

The gas configuration for electrolysis experiments at elevated pressures is shown in Figure A-C1c. To set up an experiment, 3 pump-purge cycles were performed with CO in which the reactor was charged to 5 bar CO (Airgas CM R300), then purged, and this process was repeated for a total of 3 times. Then on the fourth pump step, the reactor was left at 5 bar CO. Notably, both catholyte and anolyte were connected to the same static atmosphere of CO – this helped ensure no large pressure differentials across the separator, and gas-phase crosstalk between anode and cathode was assumed to not influence the electrochemical hydroformylation reaction of interest. A reference electrode was not used in elevated pressure experiments.

The gas configuration for electrolysis experiments at ambient pressure is shown in Figure A-C1d. In short, CO gas was bubbled into the catholyte at 10 sccm. Bubbling into the catholyte was necessary to achieve high degree of convection required to mitigate mass transport limitations and allow for collection of more reliable kinetic data.

Application of potential was performed using a potentiostat (Biologic VMP-3e). Elevated pressure experiments were performed as chronopotentiostatically (CP, constant current). Ambient pressure experiments were performed chronoamerometrically (CA, constant voltage). CA measurements were run with 90% automatic resistance compensation, where electrolyte resistance was determined using potentio-electrochemical impedence spectroscopy (PEIS) measurements. The last 10% of IR drop was not compensated. Typical electrochemical experiments, at both elevated and ambient pressures, were run for 1-3 hrs.

Reaction workup and product quantification. For thermochemical measurements, the entire electrolyte was collected for product analysis, and for electrochemical measurements, only the catholyte was collected for product analysis (product crossover to the anolyte was confirmed to be negligible). In both cases, this yielded approx. 2 mL of collected liquid. To the reaction liquid, 20 uL of 0.16 M 1,3,5-trimethoxybenzene (TMB, Sigma 138827) solution in IPA was added as an internal standard. Then, 1 mL of acetonitrile and 1 mL of milliQ water were added. Finally, the reaction was extracted three times, using 500 uL of hexanes for each extraction. A Gas Chromatograph-Mass Spectrometer (GCMS, 7890B GC, Agilent) fitted with a DB-WAX column and Flame Ionization Detector (FID) was used to identify and quantify products. Splitless injection was used. The temperature ramp of the GCMS method is shown in Figure A-C2. GCMS analysis was performed directly on the ~1.5 mL of collected organic phase.

For quantitative analysis of the FID signal, we constructed calibration curves to account for two unknowns: (1) the FID response factor differences between the internal standard (TMB) and the products and (2) differences in extraction efficiencies between the internal standard and the products (we noticed some product remained in the aqueous phase during extractions). To account for both of these factors simultaneously, we constructed a calibration curve in which we added known amounts of the products (2-phenylpropanal (Sigma 241369) and/or ethylbenzene (Sigma 296848)) to 2 mL of electrolyte solution and worked up the resulting "product-spiked electrolyte" solution in the same way that we worked up electrolyte collected from actual reactions (as detailed in the paragraph above). Integrations from the resulting FID spectra yielded calibration curves with "observed product/TMB peak ratio" on one axis and "known product/TMB molar ratio prior to extraction" on the other. The number of moles in the calibration curve for 2-phenylpropanal ranged from around 60-800 umoles in 2 mL of electrolyte, and the calibration curve for ethylbenzene ranged from 0.5-1.2 mmoles in 2 mL of electrolyte (the quantification for ethylbenzene was less sensitive than that for 2-phenylpropanal). Finally, to account for any errors in massing during the preparation of

reference solutions with known product amounts, a second set of solutions was prepared identically to the "product-spiked electrolyte", but with 2 mL of $CDCl_3$ instead of electrolyte. This resulting solution was directly analyzed with NMR to confirm molar ratios between products and internal standard.

Hydrogen gas was quantified using an online gas chromatograph (GC, 8610C SRI MultiGas 5). Samples were injected through a 1 ml sample loop to a mol sieve column held at 80 °C. A thermal conductivity detector (TCD) was used to quantify hydrogen. The sample sequence was run every 5 minutes. Hydrogen FE was calculated by averaging H_2 signal from the 5 minute mark until the end of the run.

Data analysis - calculations and statistics. Turnover frequency was calculated as following:

$$(moles\ of\ product) \Big/ (moles\ of\ active\ sites) * (reaction\ time)$$

The products of electro-HFN were 2-phenylpropanal, and, at elevated temperatures, 3-phenylpropanal as well (the latter was not detected at room temperature). The number of active sites was calculated assuming all deposited Rh sites were active. This may be an overestimation of the actual number of catalytically accessible Rh atoms, so the TOFs reported in this work may be an underestimation of the true TOF of the system. Because this site normalization was used consistently throughout the work, its nature does not change any mechanistic interpretations of the data.

Faradaic efficiency was calculated as the following:

$$F * (moles\ of\ product) * (\#electrons\ per\ product) \Big/ (total\ charge\ passed)$$

Where F is Faraday's constant, and all products reported in this work (electro-HFN, hydrogenation, and HER) are 2 electron products.

In general, data values represent means and error bars represent sample standard deviations for independently collected replicates of $n \geq 3$.

XAS measurements. Both *operando* and *ex situ* XAS measurements were performed at the Inner Shell Spectroscopy (ISS, also known as 8-ID) beamline[136] at Brookhaven National Laboratory. Catalyst samples were prepared identically to as they were for actual reactivity studies. Additionally, measurements were taken using a standard electrochemical cell with the only differences being (1) for convenience, no separator was used and (2) the back plate touching the working electrode had a Kapton (X-ray transparent) window in it, and electrical

contact to the working electrode was made with a thin ring of aluminum tape (i.e., aluminum tape with a 12 mm diameter hole punched in it) rather than the glassy carbon plate that was used for actual electrolysis experiments (Figure A-C4).

All XAS measurements on catalyst samples were collected in fluorescence mode, with the sample facing the incident beam at a 45-degree angle. Fluorescing photons were collected with a PIPS detector, and better signal-to-noise (s/n) was achieved with two strategies: (1) use of a z-1 (Ru) filter to absorb adventitious, lower-energy fluorescence and (2) use of soller slits to help focus fluorescence collection to a more localized spatial region right at the electrode surface. We did not find the use of a silicon drift detector (SDD) to help improve s/n in this case.

For *ex situ* measurements, samples were mounted inside the aforementioned XAS cell, but the cell was kept empty (i.e., no electrolyte and open to ambient air)

For any given *operando* experiment, the sample was first filled with a typical electro-HFN electrolyte: 0.1 M TBAOTf + 25 mM HOTf in either 50% or 80% v/v IPA/H_2O electrolyte (we found the exact water content in the electrolyte did not affect the measurements, Figure A-C9c). Then, the appropriate reactants were added (between 0.4 – 0.5 M styrene when styrene was added, and 10 sccm of CO at 1 bar when CO was added). The electrode was then sequentially stepped from the least reductive to the most reductive potential. At each potential, the sample was allowed to reach steady state for 10 minutes, and then XAS data at the Rh K-edge was collected for ~30 minutes, yielding approximately 30 scans (each collected at a different location on the electrode) that would later be averaged. We collected in different locations simply to get a more spatially averaged measurement of the electrode; we tested for but did not see any evidence of beam damage. For the same electrolyte/gas settings, the electrode was not swapped out between different tested potentials. For different electrolyte/gas settings, the cell was disassembled, cleaned, and prepared with a fresh electrode and electrolyte. All experiments were performed at ambient pressure with gas (either CO or N_2) bubbling through the electrolyte.

Reference materials employed for these studies were Rh_2O_3 powder (Sigma Aldrich 204226) and Rh(0) foil. The Rh_2O_3 powder was diluted into PEG powder using quantities calculated in Athena[137] and then pressed into a pellet. XAS measurements were then collected on this pellet in transmission mode. Spectra for the Rh(0) foil were obtained by using reference channel data

for an arbitrary run. Since Rh(0) foil was used as the reference channel, using I_R (reference current)/I_T (transmission current) gave the XAS absorption of the Rh(0) foil.

XANES and EXAFS data analysis. General XAS data processing was performed in Athena, and EXAFS fitting was performed using Artemis.[137]

For XANES processing, all spectra were normalized with the same parameters. Rh K-edge energies that are reported represent the energies at which the normalized spectra obtain a value of 0.5; this was intended as an approximation of the inflection point of the rising edge.

For EXAFS fitting, IFEFFIT calculations of Rh_2O_3 scattering paths were performed using a trigonal Rh_2O_3 cif structure (mp543734) downloaded from materialsproject.org. For this structure, the IFEFFIT calculations yielded two nearly identical Rh-O scattering paths, each with a coordination number of 3. For the fitting in this work, to reduce the number of fitting parameters, only the Rh-O scattering path with the shorter characteristic length was used for fitting, and for bulk Rh_2O_3, its associated coordination number was set to 6. In terms of other data processing parameters, we used an rbkg value of 1.2 and constrained the fitting between r values of 1.25 and 2.15 (to get approx. the first coordination shell).

5 CONCLUSIONS & OUTLOOK

5.1 Conclusions

In this thesis, we discuss how the complex phenomena at electrocatalytic interphases can be deconvoluted to achieve deeper mechanistic insight and also how they can be leveraged to achieve new catalytic outcomes. We explore these concepts for chemistries with possible applications in sequentially converting CO_2 into hydrocarbon fuels – first, making CO, and then, forming C–C bonds to make extended hydrocarbon chains.

In the context of the relatively well-studied chemistry of CO_2 electroreduction to CO, we develop strategies for gaining mechanistic insight. We show that cohesive kinetic analysis strategies typically used in heterogenous thermocatalysis are equally useful in electrocatalysis, and that their application led to new mechanistic insight on a promising and ostensibly well-studied CO_2 reduction catalyst. We also developed an automated system to enhance the workflow for this type of kinetic analysis, and used it to extend the initial mechanistic analysis to a series of related catalysts.

We then moved into the relatively underexplored realm of electrochemical C–C bond formation between olefins and CO. In this case, we showed that new electrocatalytic reactivity could be designed by importing active sites with related thermochemical reactivity onto electrode surfaces. Specifically, we imported active sites from organometallic hydroformylation catalysis onto electrode surfaces to achieve electrochemical C–C bond formation.

5.2 Outlook

5.2.1 Cohesive kinetic analysis

Cohesive kinetic analysis has the potential to offer new evidence and perspectives on a variety of mechanistic questions. We discuss some possibilities in the spaces of electrolyte effects and structure-property relationships.

In the space of electrolyte effects, certain ions or additives within the electrolyte have been shown to affect electrocatalytic activity for reactions including CO_2RR and HER. The

experimental interrogation of these effects generally involves relatively small quantities of experimental rate data, which are typically used, in conjunction with other computational or spectroscopic characterizations, to support relatively general mechanistic hypotheses. However, this space is one in which complex mechanisms are likely to exist, and for which cohesive kinetic analyses akin to the ones we demonstrated in this thesis could be highly useful. Such analysis could involve, for example, collecting "order dependencies" for the different additives/salts, as well as rate data in different regimes of additive/salt concentrations. Additionally, use of automated systems could significantly reduce the experimental burden of performing such analyses.

Additionally, in the general space of "structure property relationships", it would be interesting to demonstrate that catalytic "properties" can be highly multidimensional. For example, in a complex mechanism where limits of rate control or surface coverage differ significantly with, for example, applied potential, "property" of a catalyst that is being tested is highly dependent on the testing condition. Yet, this complexity is not often captured in "structure-property" studies, where often, rates of different catalysts are only compared at one reaction condition. It would be interesting to demonstrate that for the same series of catalysts, different properties of the catalyst structure are important for describing reactivity for different operating conditions. Such a study would require cohesive kinetic analysis of a series of catalysts to help describe the limits of reactivity that are being probed at different reaction conditions.

5.2.2 Electrified C–C bond formation

Electrified hydroformylation catalysis is an underexplored space with many opportunities for improving both performance and fundamental understanding of the chemistry. Possible directions include studying the effects of catalyst modification, electrolyte composition, and reactor design. For example, different metals, supports, and motifs would be interesting to explore. Within this phase space, one particularly interesting question would be whether the above changes could be used to effect different extents and natures of electronic coupling between the catalytic site and the support, and whether these different electronic structures could give rise to perturbed, enhanced, or perhaps even fundamentally different modes of catalysis. Additionally, different solvents and electrolyte additives would be interesting to explore further. The triflate anion, for example, seemed to be critical for improving reactivity, and it would be interesting to probe the origin and possible extension of that effect. Finally, continued exploration of reactor design is likely to be interesting from an engineering

standpoint and also highly fruitful. The current system involves gas-phase reactants, high pressure, and sparingly soluble liquid-phase reactants – clever cell engineering to efficiently deliver reactants to the electrified interphase would likely improve performance.

Finally, in the most general sense, it would be interesting to apply the strategy we developed of importing thermochemical catalysts onto electrode surfaces to more chemistries and active site motifs. Many “dream” electrocatalytic reactions have thermochemical “counterparts” that are efficiently achieved by known thermochemical catalysts. Broader extension of this design paradigm could prove to be highly impactful.

6 REFERENCES

(1) Schiffer, Z. J.; Manthiram, K. Electrification and Decarbonization of the Chemical Industry. *Joule* **2017**, *1* (1), 10–14. https://doi.org/10.1016/j.joule.2017.07.008.

(2) Zhu, J.; Hu, L.; Zhao, P.; Lee, L. Y. S.; Wong, K. Y. Recent Advances in Electrocatalytic Hydrogen Evolution Using Nanoparticles. *Chem Rev* **2020**, *120* (2), 851–918. https://doi.org/10.1021/ACS.CHEMREV.9B00248/ASSET/IMAGES/MEDIUM/CR9B00248_0056.GIF.

(3) Qiao, J.; Liu, Y.; Hong, F.; Zhang, J. *A Review of Catalysts for the Electroreduction of Carbon Dioxide to Produce Low-Carbon Fuels*; 2014; Vol. 43. https://doi.org/10.1039/C3CS60323G.

(4) Zhao, G.; Wang, X.; Wang, X. Progress in Catalyst Exploration for Heterogeneous CO 2 Reduction and Utilization : A Critical Review. *Journal of Materials Chemistry A: Materials for energy and sustainability* **2017**, *5*, 21625–21649. https://doi.org/10.1039/C7TA07290B.

(5) Hori, Y. Electrochemical CO 2 Reduction on Metal Electrodes. *Modern Aspects of Electrochemistry* **2008**, No. 42, 89–189. https://doi.org/10.1007/978-0-387-49489-0_3.

(6) Schemme, S.; Samsun, R. C.; Peters, R.; Stolten, D. Power-to-Fuel as a Key to Sustainable Transport Systems – An Analysis of Diesel Fuels Produced from CO2 and Renewable Electricity. *Fuel* **2017**, *205*, 198–221. https://doi.org/10.1016/J.FUEL.2017.05.061.

(7) Wang, X.; Ou, P.; Ozden, A.; Hung, S. F.; Tam, J.; Gabardo, C. M.; Howe, J. Y.; Sisler, J.; Bertens, K.; García de Arquer, F. P.; Miao, R. K.; O'Brien, C. P.; Wang, Z.; Abed, J.; Rasouli, A. S.; Sun, M.; Ip, A. H.; Sinton, D.; Sargent, E. H. Efficient Electrosynthesis of N-Propanol from Carbon Monoxide Using a Ag–Ru–Cu Catalyst. *Nature Energy 2022 7:2* **2022**, *7* (2), 170–176. https://doi.org/10.1038/s41560-021-00967-7.

(8) Jiang, K.; Sandberg, R. B.; Akey, A. J.; Liu, X.; Bell, D. C.; Nørskov, J. K.; Chan, K.; Wang, H. Metal Ion Cycling of Cu Foil for Selective C–C Coupling in Electrochemical

CO2 Reduction. *Nature Catalysis 2017 1:2* **2018**, *1* (2), 111–119. https://doi.org/10.1038/s41929-017-0009-x.

(9) Ren, D.; Wong, N. T.; Handoko, A. D.; Huang, Y.; Yeo, B. S. Mechanistic Insights into the Enhanced Activity and Stability of Agglomerated Cu Nanocrystals for the Electrochemical Reduction of Carbon Dioxide to N-Propanol. *Journal of Physical Chemistry Letters* **2016**, *7* (1), 20–24. https://doi.org/10.1021/ACS.JPCLETT.5B02554/SUPPL_FILE/JZ5B02554_SI_001.PDF.

(10) Woodall, C. M.; Fan, Z.; Lou, Y.; Bhardwaj, A.; Khatri, A.; Agrawal, M.; McCormick, C. F.; Friedmann, S. J. Technology Options and Policy Design to Facilitate Decarbonization of Chemical Manufacturing. *Joule* **2022**, *6* (11), 2474–2499. https://doi.org/10.1016/J.JOULE.2022.10.006.

(11) Mallapragada, D. S.; Dvorkin, Y.; Modestino, M. A.; Esposito, D. v.; Smith, W. A.; Hodge, B. M.; Harold, M. P.; Donnelly, V. M.; Nuz, A.; Bloomquist, C.; Baker, K.; Grabow, L. C.; Yan, Y.; Rajput, N. N.; Hartman, R. L.; Biddinger, E. J.; Aydil, E. S.; Taylor, A. D. Decarbonization of the Chemical Industry through Electrification: Barriers and Opportunities. *Joule* **2023**, *7* (1), 23–41. https://doi.org/10.1016/j.joule.2022.12.008.

(12) Shukla, P. R.; Skea, J.; Slade, R.; Khourdajie, A. al; van Diemen, R.; McCollum, D.; Pathak, M.; Some, S.; Vyas, P.; Fradera, R.; Belkacemi, M.; Hasija, A.; Lisboa, G.; Luz, S.; Malley, J. *IPCC, 2022: Climate Change 2022: Mitigation of Climate Change. Contribution of Working Group III to the Sixth Assessment Report of the Intergovernmental Panel on Climate Change*; Cambridge, UK, 2022.

(13) Novaes, L. F. T.; Liu, J.; Shen, Y.; Lu, L.; Meinhardt, J. M.; Lin, S. Electrocatalysis as an Enabling Technology for Organic Synthesis. *Chem Soc Rev* **2021**, *50* (14), 7941–8002. https://doi.org/10.1039/D1CS00223F.

(14) Yan, M.; Kawamata, Y.; Baran, P. S. Synthetic Organic Electrochemical Methods since 2000: On the Verge of a Renaissance. *Chem Rev* **2017**, *117* (21), 13230–13319. https://doi.org/10.1021/ACS.CHEMREV.7B00397/ASSET/IMAGES/MEDIUM/CR-2017-00397G_0054.GIF.

(15) Xia, C.; Xia, Y.; Zhu, P.; Fan, L.; Wang, H. Direct Electrosynthesis of Pure Aqueous H2O2solutions up to 20% by Weight Using a Solid Electrolyte. *Science (1979)* **2019**,

366 (6462), 226–231. https://doi.org/10.1126/SCIENCE.AAY1844/SUPPL_FILE/AAY1844-XIA-SM.PDF.

(16) Pletcher, D.; Walsh, F. C. Industrial Electrochemistry. **1993**. https://doi.org/10.1007/978-94-011-2154-5.

(17) Wuttig, A.; Toste, F. D.; Toste, F. D.; Sci, N. The Interface Is a Tunable Dimension in Electricity-Driven Organic Synthesis. *Natural Sciences* **2021**, *1* (2), e20210036. https://doi.org/10.1002/NTLS.20210036.

(18) Bard, A. J.; Faulkner, L. R. *Electrochemical Methods: Fundamentals and Applications, 2nd Edition*; Wiley, 2001.

(19) Timmer, B.; Sluyters-Rehbach, M.; Sluyters, J. H. Electrode Kinetics and Double Layer Structure. *Surf Sci* **1969**, *18* (1), 44–61. https://doi.org/10.1016/0039-6028(69)90266-0.

(20) Limaye, A. M.; Willard, A. P. Modeling Interfacial Electron Transfer in the Double Layer: The Interplay between Electrode Coupling and Electrostatic Driving. *Journal of Physical Chemistry C* **2020**, *124* (2), 1352–1361. https://doi.org/10.1021/ACS.JPCC.9B08438/SUPPL_FILE/JP9B08438_SI_001.PDF.

(21) Schmickler, W.; Santos, E. *Interfacial Electrochemistry*; Springer Berlin Heidelberg, 2010. https://doi.org/10.1007/978-3-642-04937-8.

(22) Schultze, J. W.; Vetter, K. J. Experimental Determination and Interpretation of the Electrosorption Valency γ. *Journal of Electroanalytical Chemistry* **1973**, *44* (1), 63–81. https://doi.org/10.1016/S0022-0728(73)80515-7.

(23) Nong, H. N.; Falling, L. J.; Bergmann, A.; Klingenhof, M.; Tran, H. P.; Spöri, C.; Mom, R.; Timoshenko, J.; Zichittella, G.; Knop-Gericke, A.; Piccinin, S.; Pérez-Ramírez, J.; Cuenya, B. R.; Schlögl, R.; Strasser, P.; Teschner, D.; Jones, T. E. Key Role of Chemistry versus Bias in Electrocatalytic Oxygen Evolution. *Nature 2020 587:7834* **2020**, *587* (7834), 408–413. https://doi.org/10.1038/s41586-020-2908-2.

(24) Boettcher, S. W.; Surendranath, Y. Heterogeneous Electrocatalysis Goes Chemical. *Nature Catalysis 2021 4:1* **2021**, *4* (1), 4–5. https://doi.org/10.1038/s41929-020-00570-1.

(25) Boettcher, S. W.; Oener, S. Z.; Lonergan, M. C.; Surendranath, Y.; Ardo, S.; Brozek, C.; Kempler, P. A. Potentially Confusing: Potentials in Electrochemistry. *ACS Energy Lett* **2021**, *6* (1), 261–266.

https://doi.org/10.1021/ACSENERGYLETT.0C02443/ASSET/IMAGES/MEDIUM/NZ0C02443_M021.GIF.

(26) Akinola, J.; Barth, I.; Goldsmith, B. R.; Singh, N. Adsorption Energies of Oxygenated Aromatics and Organics on Rhodium and Platinum in Aqueous Phase. *ACS Catal* **2020**, *10* (9), 4929–4941. https://doi.org/10.1021/ACSCATAL.0C00803/SUPPL_FILE/CS0C00803_SI_001.PDF.

(27) Foresti, M. L.; Innocenti, M.; Hamelin, A. Adsorption Behavior of N-Hexanol on Ag(Lll) from Aqueous 0.05 M KCIO4. *Langmuir* **1995**, *11* (2), 498–505. https://doi.org/10.1021/LA00002A023/ASSET/LA00002A023.FP.PNG_V03.

(28) Léonard, N. G.; Dhaoui, R.; Chantarojsiri, T.; Yang, J. Y. Electric Fields in Catalysis: From Enzymes to Molecular Catalysts. *ACS Catal* **2021**, *11* (17), 10923–10932. https://doi.org/10.1021/ACSCATAL.1C02084/ASSET/IMAGES/MEDIUM/CS1C02084_0006.GIF.

(29) Wesley, T. S.; Román-Leshkov, Y.; Surendranath, Y. Spontaneous Electric Fields Play a Key Role in Thermochemical Catalysis at Metal-Liquid Interfaces. *ACS Cent Sci* **2021**, *7* (6), 1045–1055. https://doi.org/10.1021/ACSCENTSCI.1C00293/ASSET/IMAGES/MEDIUM/OC1C00293_0004.GIF.

(30) Velasco-Velez, J. J.; Wu, C. H.; Pascal, T. A.; Wan, L. F.; Guo, J.; Prendergast, D.; Salmeron, M. The Structure of Interfacial Water on Gold Electrodes Studied by X-Ray Absorption Spectroscopy. *Science (1979)* **2014**, *346* (6211), 831–834. https://doi.org/10.1126/SCIENCE.1259437/SUPPL_FILE/VELASCO-VELEZ-SM.PDF.

(31) Sharifi Golru, S.; Biddinger, E. J. Effect of Additives in Aqueous Electrolytes on CO2 Electroreduction. *Chemical Engineering Journal* **2022**, *428*, 131303. https://doi.org/10.1016/J.CEJ.2021.131303.

(32) Pennathur, A. K.; Tseng, C.; Salazar, N.; Dawlaty, J. M. Controlling Water Delivery to an Electrochemical Interface with Surfactants. *J Am Chem Soc* **2023**. https://doi.org/10.1021/JACS.2C11503/SUPPL_FILE/JA2C11503_SI_001.PDF.

(33) Li, C. W.; Ciston, J.; Kanan, M. W. Electroreduction of Carbon Monoxide to Liquid Fuel on Oxide-Derived Nanocrystalline Copper. *Nature 2014 508:7497* **2014**, *508* (7497), 504–507. https://doi.org/10.1038/nature13249.

(34) Ro, I.; Resasco, J.; Christopher, P. Approaches for Understanding and Controlling Interfacial Effects in Oxide-Supported Metal Catalysts. *ACS Catal* **2018**, *8* (8), 7368–7387. https://doi.org/10.1021/ACSCATAL.8B02071/ASSET/IMAGES/MEDIUM/CS-2018-02071R_0012.GIF.

(35) Kaminsky, C. J.; Weng, S.; Wright, J.; Surendranath, Y. Adsorbed Cobalt Porphyrins Act like Metal Surfaces in Electrocatalysis. *Nature Catalysis 2022 5:5* **2022**, *5* (5), 430–442. https://doi.org/10.1038/s41929-022-00791-6.

(36) Jackson, M. N.; Oh, S.; Kaminsky, C. J.; Chu, S. B.; Zhang, G.; Miller, J. T.; Surendranath, Y. Strong Electronic Coupling of Molecular Sites to Graphitic Electrodes via Pyrazine Conjugation. *J Am Chem Soc* **2018**, *140* (3), 1004–1010. https://doi.org/10.1021/jacs.7b10723.

(37) Burdyny, T.; Smith, W. A. CO 2 Reduction on Gas-Diffusion Electrodes and Why Catalytic Performance Must Be Assessed at Commercially-Relevant Conditions. *Energy Environ Sci* **2019**, *12* (5), 1442–1453. https://doi.org/10.1039/C8EE03134G.

(38) Clark, E. L.; Resasco, J.; Landers, A.; Lin, J.; Chung, L. T.; Walton, A.; Hahn, C.; Jaramillo, T. F.; Bell, A. T. Standards and Protocols for Data Acquisition and Reporting for Studies of the Electrochemical Reduction of Carbon Dioxide. *ACS Catal* **2018**, *8* (7), 6560–6570. https://doi.org/10.1021/ACSCATAL.8B01340/ASSET/IMAGES/LARGE/CS-2018-01340U_0010.JPEG.

(39) Lobaccaro, P.; Singh, M. R.; Clark, E. L.; Kwon, Y.; Bell, A. T.; Ager, J. W. Effects of Temperature and Gas–Liquid Mass Transfer on the Operation of Small Electrochemical Cells for the Quantitative Evaluation of CO2 Reduction Electrocatalysts. *Physical Chemistry Chemical Physics* **2016**, *18* (38), 26777–26785. https://doi.org/10.1039/C6CP05287H.

(40) Lazouski, N.; Chung, M.; Williams, K.; Gala, M. L.; Manthiram, K. Non-Aqueous Gas Diffusion Electrodes for Rapid Ammonia Synthesis from Nitrogen and Water-Splitting-Derived Hydrogen. *Nature Catalysis 2020 3:5* **2020**, *3* (5), 463–469. https://doi.org/10.1038/s41929-020-0455-8.

(41) Han, C.; Zenner, J.; Johny, J.; Kaeffer, N.; Bordet, A.; Leitner, W. Electrocatalytic Hydrogenation of Alkenes with Pd/Carbon Nanotubes at an Oil–Water Interface. *Nature Catalysis 2022 5:12* **2022**, *5* (12), 1110–1119. https://doi.org/10.1038/s41929-022-00882-4.

(42) Zeng, J. S.; Corbin, N.; Williams, K.; Manthiram, K. Kinetic Analysis on the Role of Bicarbonate in Carbon Dioxide Electroreduction at Immobilized Cobalt Phthalocyanine. *ACS Catal* **2020**, *10* (7), 4326–4336. https://doi.org/10.1021/acscatal.9b05272.

(43) Clark, E. L.; Bell, A. T. Direct Observation of the Local Reaction Environment during the Electrochemical Reduction of CO 2. *J Am Chem Soc* **2018**, *140* (22), 7012–7020. https://doi.org/10.1021/jacs.8b04058.

(44) Singh, M. R.; Goodpaster, J. D.; Weber, A. Z.; Head-Gordon, M.; Bell, A. T. Mechanistic Insights into Electrochemical Reduction of CO2 over Ag Using Density Functional Theory and Transport Models. *Proc Natl Acad Sci U S A* **2017**, *114* (42), E8812–E8821. https://doi.org/10.1073/pnas.1713164114.

(45) Williams, K.; Corbin, N.; Zeng, J.; Lazouski, N.; Yang, D. T.; Manthiram, K. Protecting Effect of Mass Transport during Electrochemical Reduction of Oxygenated Carbon Dioxide Feedstocks. *Sustain Energy Fuels* **2019**, *3* (5), 1225–1232. https://doi.org/10.1039/c9se00024k.

(46) Wuttig, A.; Yoon, Y.; Ryu, J.; Surendranath, Y. Bicarbonate Is Not a General Acid in Au-Catalyzed CO 2 Electroreduction. *J Am Chem Soc* **2017**, *139* (47), 17109–17113. https://doi.org/10.1021/jacs.7b08345.

(47) Dunwell, M.; Lu, Q.; Heyes, J. M.; Rosen, J.; Chen, J. G.; Yan, Y.; Jiao, F.; Xu, B. The Central Role of Bicarbonate in the Electrochemical Reduction of Carbon Dioxide on Gold. *J Am Chem Soc* **2017**, *139* (10), 3774–3783. https://doi.org/10.1021/jacs.6b13287.

(48) Zhang, Z.; Xiao, J.; Chen, X.-J.; Yu, S.; Yu, L.; Si, R.; Wang, Y.; Wang, S.; Meng, X.; Wang, Y.; Tian, Z.-Q.; Deng, D. Understanding the Reaction Mechanisms of Well-Defined Metal-N4 Sites in Electrocatalytic CO2 Reduction. *Angewandte Chemie International Edition* **2018**, *57* (50), 16339–16342. https://doi.org/10.1002/anie.201808593.

(49) Furuya, N.; Koide, S. Electroreduction of Carbon Dioxide by Metal Phthalocyanines. *Electrochim Acta* **1991**, *36* (8), 1309–1313. https://doi.org/10.1016/0013-4686(91)80010-6.

(50) Furuya, N.; Matsui, K. Electroreduction of Carbon Dioxide on Gas-Diffusion Electrodes Modified by Metal Phthalocyanines. *Journal of Electroanalytical Chemistry* **1989**, *271* (1–2), 181–191. https://doi.org/10.1016/0022-0728(89)80074-9.

(51) Zhu, M.; Ye, R.; Jin, K.; Lazouski, N.; Manthiram, K. Elucidating the Reactivity and Mechanism of CO 2 Electroreduction at Highly Dispersed Cobalt Phthalocyanine. *ACS Energy Lett* **2018**, *3* (6), 1381–1386. https://doi.org/10.1021/acsenergylett.8b00519.

(52) Abe, T.; Imaya, H.; Yoshida, T.; Tokita, S.; Schlettwein, D.; Wohrle, D.; Kaneko, M. Electrochemical CO2 Reduction Catalyzed by Cobalt Octacyanophthalocyanine and Its Mechanism. *J Porphyr Phthalocyanines* **1997**, *1* (4), 315–321. https://doi.org/10.1002/(sici)1099-1409(199710)1:4<315::aid-jpp35>3.0.co;2-v.

(53) Hu, X.; Rønne, M. H.; Pedersen, S. U.; Skrydstrup, T.; Daasbjerg, K. Enhanced Catalytic Activity of Cobalt Porphyrin in CO 2 Electroreduction upon Immobilization on Carbon Materials. *Angewandte Chemie* **2017**, *56*, 6468–6472. https://doi.org/10.1002/anie.201701104.

(54) Manbeck, G. F.; Fujita, E. A Review of Iron and Cobalt Porphyrins, Phthalocyanines and Related Complexes for Electrochemical and Photochemical Reduction of Carbon Dioxide. *J Porphyr Phthalocyanines* **2015**, *19* (01–03), 45–64. https://doi.org/10.1142/S1088424615300013.

(55) Ren, S.; Joulié, D.; Salvatore, D.; Torbensen, K.; Wang, M.; Robert, M.; Berlinguette, C. P. Molecular Electrocatalysts Can Mediate Fast, Selective CO 2 Reduction in a Flow Cell. *Science (1979)* **2019**, *365*, 367–369. https://doi.org/10.1126/science.aax4608.

(56) Wang, M.; Torbensen, K.; Salvatore, D.; Ren, S.; Joulié, D.; Dumoulin, F.; Mendoza, D.; Lassalle-Kaiser, B.; Işci, U.; Berlinguette, C. P.; Robert, M. CO2 Electrochemical Catalytic Reduction with a Highly Active Cobalt Phthalocyanine. *Nat Commun* **2019**, *10* (1). https://doi.org/10.1038/s41467-019-11542-w.

(57) Corbin, N.; Zeng, J.; Williams, K.; Manthiram, K. Heterogeneous Molecular Catalysts for Electrocatalytic CO 2 Reduction. *Nano Res* **2019**, *12* (9), 2093–2125. https://doi.org/10.1007/s12274-019-2403-y.

(58) Zhu, M.; Yang, D.-T.; Ye, R.; Zeng, J.; Corbin, N.; Manthiram, K. Inductive and Electrostatic Effects on Cobalt Porphyrins for Heterogeneous Electrocatalytic Carbon Dioxide Reduction. *Catal Sci Technol* **2019**, *9*, 974–980. https://doi.org/10.1039/C9CY00102F.

(59) Lin, S.; Diercks, C. S.; Zhang, Y. B.; Kornienko, N.; Nichols, E. M.; Zhao, Y.; Paris, A. R.; Kim, D.; Yang, P.; Yaghi, O. M.; Chang, C. J. Covalent Organic Frameworks Comprising Cobalt Porphyrins for Catalytic CO2 Reduction in Water. *Science (1979)* **2015**, *349* (6253), 1208–1213. https://doi.org/10.1126/science.aac8343.

(60) Varela, A. S.; Kroschel, M.; Leonard, N. D.; Ju, W.; Steinberg, J.; Bagger, A.; Rossmeisl, J.; Strasser, P. PH Effects on the Selectivity of the Electrocatalytic CO 2 Reduction on Graphene-Embedded Fe–N–C Motifs: Bridging Concepts between Molecular Homogeneous and Solid-State Heterogeneous Catalysis. *ACS Energy Lett* **2018**, *3* (4), 812–817. https://doi.org/10.1021/acsenergylett.8b00273.

(61) Morlanés, N.; Takanabe, K.; Rodionov, V. Simultaneous Reduction of CO2 and Splitting of H2O by a Single Immobilized Cobalt Phthalocyanine Electrocatalyst. *ACS Catal* **2016**, *6* (5), 3092–3095. https://doi.org/10.1021/acscatal.6b00543.

(62) Shen, J.; Kortlever, R.; Kas, R.; Birdja, Y. Y.; Diaz-Morales, O.; Kwon, Y.; Ledezma-Yanez, I.; Schouten, K. J. P.; Mul, G.; Koper, M. T. M. Electrocatalytic Reduction of Carbon Dioxide to Carbon Monoxide and Methane at an Immobilized Cobalt Protoporphyrin. *Nat Commun* **2015**, *6*. https://doi.org/10.1038/ncomms9177.

(63) Xia, Y.; Kashtanov, S.; Yu, P.; Chang, L. Y.; Feng, K.; Zhong, J.; Guo, J.; Sun, X. Identification of Dual-Active Sites in Cobalt Phthalocyanine for Electrochemical Carbon Dioxide Reduction. *Nano Energy* **2019**. https://doi.org/10.1016/j.nanoen.2019.104163.

(64) Christensen, P. A.; Hamnett, A.; Muir, A. V. G. An In-Situ Ftir Study of the Electroreduction of Co2 by Copc-Coated Edge Graphite Electrodes. *Journal of Electroanalytical Chemistry* **1988**, *241* (1–2), 361–371. https://doi.org/10.1016/0022-0728(88)85139-8.

(65) Shen, J.; Kolb, M. J.; Göttle, A. J.; Koper, M. T. M. DFT Study on the Mechanism of the Electrochemical Reduction of CO 2 Catalyzed by Cobalt Porphyrins. *The Journal of Physical Chemistry C* **2016**, *120* (29), 15714–15721. https://doi.org/10.1021/acs.jpcc.5b10763.

(66) Leung, K.; Nielsen, I. M. B.; Sai, N.; Medforth, C.; Shelnutt, J. A. Cobalt-Porphyrin Catalyzed Electrochemical Reduction of Carbon Dioxide in Water. 2. Mechanism from First Principles. *Journal of Physical Chemistry A* **2010**, *114* (37), 10174–10184. https://doi.org/10.1021/jp1012335.

(67) Göttle, A. J.; Koper, M. T. M. Proton-Coupled Electron Transfer in the Electrocatalysis of CO2 Reduction: Prediction of Sequential vs. Concerted Pathways Using DFT. *Chem Sci* **2016**, *8* (1), 458–465. https://doi.org/10.1039/c6sc02984a.

(68) Shinagawa, T.; Garcia-Esparza, A. T.; Takanabe, K. Insight on Tafel Slopes from a Microkinetic Analysis of Aqueous Electrocatalysis for Energy Conversion. *Sci Rep* **2015**, *5*. https://doi.org/10.1038/srep13801.

(69) Miller, J. H.; Bui, L.; Bhan, A. Pathways, Mechanisms, and Kinetics: A Strategy to Examine Byproduct Selectivity in Partial Oxidation Catalytic Transformations on Reducible Oxides. *Reaction Chemistry and Engineering*. Royal Society of Chemistry May 1, 2019, pp 784–805. https://doi.org/10.1039/c8re00285a.

(70) Rangarajan, S.; Maravelias, C. T.; Mavrikakis, M. Sequential-Optimization-Based Framework for Robust Modeling and Design of Heterogeneous Catalytic Systems. *Journal of Physical Chemistry C* **2017**, *121* (46), 25847–25863. https://doi.org/10.1021/acs.jpcc.7b08089.

(71) Bui, L.; Chakrabarti, R.; Bhan, A. Mechanistic Origins of Unselective Oxidation Products in the Conversion of Propylene to Acrolein on Bi2Mo3O12. *ACS Catal* **2016**, *6* (10), 6567–6580. https://doi.org/10.1021/acscatal.6b01830.

(72) Herrmann, S.; Iglesia, E. Selective Conversion of Acetone to Isobutene and Acetic Acid on Aluminosilicates: Kinetic Coupling between Acid-Catalyzed and Radical-Mediated Pathways. *J Catal* **2018**, *360*, 66–80. https://doi.org/10.1016/j.jcat.2018.01.032.

(73) Adanuvor, K.; White, R. E. Analysis of Electrokinetic Data by Parameter Estimation and Model Discrimination Technqiues. *J Electrochem Soc* **1988**, *135* (8), 1887–1898. https://doi.org/10.1149/1.2096174.

(74) Marshall, A. T. Using Microkinetic Models to Understand Electrocatalytic Reactions. *Current Opinion in Electrochemistry*. Elsevier B.V. January 1, 2018, pp 75–80. https://doi.org/10.1016/j.coelec.2017.10.024.

(75) Stewart, W. E.; Caracotsios, Michael. *Computer-Aided Modeling of Reactive Systems*; Wiley-Interscience, 2008.

(76) Urdan, T. C. *Statistics in Plain English*; Routledge, 2010.

(77) Decornez, H.; Hammes-Schiffer, S. Model Proton-Coupled Electron Transfer Reactions in Solution: Predictions of Rates, Mechanisms, and Kinetic Isotope Effects. *J Phys Chem A* **2000**, *104* (41), 9370–9384. https://doi.org/10.1021/jp001967s.

(78) Cape, J. L.; Bowman, M. K.; Kramer, D. M. Reaction Intermediates of Quinol Oxidation in a Photoactivatable System That Mimics Electron Transfer in the Cytochrome Bc 1 Complex. *J Am Chem Soc* **2005**, *127* (12), 4208–4215. https://doi.org/10.1021/ja043955g.

(79) Edwards, S. J.; Soudackov, A. V.; Hammes-Schiffer, S. Analysis of Kinetic Isotope Effects for Proton-Coupled Electron Transfer Reactions †. *J Phys Chem A* **2009**, *113* (10), 2117–2126. https://doi.org/10.1021/jp809122y.

(80) Singh, M. R.; Clark, E. L.; Bell, A. T. Effects of Electrolyte, Catalyst, and Membrane Composition and Operating Conditions on the Performance of Solar-Driven Electrochemical Reduction of Carbon Dioxide. *Physical Chemistry Chemical Physics* **2015**, *17* (29), 18924–18936. https://doi.org/10.1039/c5cp03283k.

(81) Yang, K.; Kas, R.; Smith, W. A. In Situ Infrared Spectroscopy Reveals Persistent Alkalinity near Electrode Surfaces during CO 2 Electroreduction. *J Am Chem Soc* **2019**, *141* (40), 15891–15900. https://doi.org/10.1021/jacs.9b07000.

(82) Ooka, H.; Figueiredo, M. C.; Koper, M. T. M. Competition between Hydrogen Evolution and Carbon Dioxide Reduction on Copper Electrodes in Mildly Acidic Media. *Langmuir* **2017**, *33* (37), 9307–9313. https://doi.org/10.1021/acs.langmuir.7b00696.

(83) Göttle, A. J.; Koper, M. T. M. Determinant Role of Electrogenerated Reactive Nucleophilic Species on Selectivity during Reduction of CO 2 Catalyzed by Metalloporphyrins. *J Am Chem Soc* **2018**, *140* (14), 4826–4834. https://doi.org/10.1021/jacs.7b11267.

(84) Christiansen, J. A. The Elucidation of Reaction Mechanisms by the Method of Intermediates in Quasi-Stationary Concentrations. *Advances in Catalysis* **1953**, *5* (C), 311–353. https://doi.org/10.1016/S0360-0564(08)60644-6.

(85) Garg, S.; Li, M.; Rufford, T. E.; Ge, L.; Rudolph, V.; Knibbe, R.; Konarova, M.; Wang, G. G. X. Catalyst–Electrolyte Interactions in Aqueous Reline Solutions for Highly Selective Electrochemical CO 2 Reduction. *ChemSusChem* **2020**, *13* (2), 304–311. https://doi.org/10.1002/cssc.201902433.

(86) Hsieh, Y.-C.; Senanayake, S. D.; Zhang, Y.; Xu, W.; Polyansky, D. E. Effect of Chloride Anions on the Synthesis and Enhanced Catalytic Activity of Silver Nanocoral Electrodes for CO 2 Electroreduction. *ACS Catal* **2015**, *5* (9), 5349–5356. https://doi.org/10.1021/acscatal.5b01235.

(87) Waegele, M. M.; Gunathunge, C. M.; Li, J.; Li, X. How Cations Affect the Electric Double Layer and the Rates and Selectivity of Electrocatalytic Processes. *Journal of Chemical Physics* **2019**, *151* (16), 1DUMMT. https://doi.org/10.1063/1.5124878.

(88) Herrero, E.; Mostany, J.; Feliu, J. M.; Lipkowski, J. Thermodynamic Studies of Anion Adsorption at the Pt(111) Electrode Surface in Sulfuric Acid Solutions. *Journal of Electroanalytical Chemistry* **2002**, *534* (1), 79–89. https://doi.org/10.1016/S0022-0728(02)01101-4.

(89) Kozuch, S.; Shaik, S. How to Conceptualize Catalytic Cycles? The Energetic Span Model. *Acc Chem Res* **2011**, *44* (2), 101–110. https://doi.org/10.1021/ar1000956.

(90) Jackson, M. N.; Surendranath, Y. Donor-Dependent Kinetics of Interfacial Proton-Coupled Electron Transfer. *J Am Chem Soc* **2016**, *138* (9), 3228–3234. https://doi.org/10.1021/jacs.6b00167.

(91) Jackson, M. N.; Jung, O.; Lamotte, H. C.; Surendranath, Y. Donor-Dependent Promotion of Interfacial Proton-Coupled Electron Transfer in Aqueous Electrocatalysis. *ACS Catal* **2019**, *9* (4), 3737–3743. https://doi.org/10.1021/acscatal.9b00056.

(92) Jenkins, H. D. B.; Thakur, K. P. Reappraisal of Thermochemical Radii for Complex Ions. *J Chem Educ* **1979**, *56* (9), 576. https://doi.org/10.1021/ed056p576.

(93) Håkansson, K.; Wehnert, A. Structure of Cobalt Carbonic Anhydrase Complexed with Bicarbonate. *J Mol Biol* **1992**, *228* (4), 1212–1218. https://doi.org/10.1016/0022-2836(92)90327-G.

(94) Firet, N. J.; Smith, W. A. Probing the Reaction Mechanism of CO2 Electroreduction over Ag Films via Operando Infrared Spectroscopy. *ACS Catal* **2017**, *7* (1), 606–612. https://doi.org/10.1021/acscatal.6b02382.

(95) Stoltze, P.; Nørskov, J. K. Bridging the “Pressure Gap” between Ultrahigh-Vacuum Surface Physics and High-Pressure Catalysis. *Phys Rev Lett* **1985**, *55* (22), 2502–2505. https://doi.org/10.1103/PhysRevLett.55.2502.

(96) König, M.; Vaes, J.; Klemm, E.; Pant, D. Solvents and Supporting Electrolytes in the Electrocatalytic Reduction of CO2. *iScience*. Elsevier Inc. September 27, 2019, pp 135–160. https://doi.org/10.1016/j.isci.2019.07.014.

(97) Verma, S.; Lu, X.; Ma, S.; Masel, R. I.; Kenis, P. J. A. The Effect of Electrolyte Composition on the Electroreduction of CO2 to CO on Ag Based Gas Diffusion Electrodes. *Physical Chemistry Chemical Physics* **2016**, *18* (10), 7075–7084. https://doi.org/10.1039/c5cp05665a.

(98) Gao, D.; McCrum, I. T.; Deo, S.; Choi, Y. W.; Scholten, F.; Wan, W.; Chen, J. G.; Janik, M. J.; Roldan Cuenya, B. Activity and Selectivity Control in CO2 Electroreduction to Multicarbon Products over CuOx Catalysts via Electrolyte Design. *ACS Catal* **2018**, *8* (11), 10012–10020. https://doi.org/10.1021/acscatal.8b02587.

(99) Ogura, K.; Ferrell, J. R.; Cugini, A. V.; Smotkin, E. S.; Salazar-Villalpando, M. D. CO2 Attraction by Specifically Adsorbed Anions and Subsequent Accelerated Electrochemical Reduction. *Electrochim Acta* **2010**, *56* (1), 381–386. https://doi.org/10.1016/j.electacta.2010.08.065.

(100) Hong, S.; Lee, S.; Kim, S.; Lee, J. K.; Lee, J. Anion Dependent CO/H2 Production Ratio from CO2 Reduction on Au Electro-Catalyst. *Catal Today* **2017**, *295*, 82–88. https://doi.org/10.1016/j.cattod.2017.05.063.

(101) Resasco, J.; Lum, Y.; Clark, E.; Zeledon, J. Z.; Bell, A. T. Effects of Anion Identity and Concentration on Electrochemical Reduction of CO 2. *ChemElectroChem* **2018**, *5* (7), 1064–1072. https://doi.org/10.1002/celc.201701316.

(102) Lynggaard, H.; Andreasen, A.; Stegelmann, C.; Stoltze, P. Analysis of Simple Kinetic Models in Heterogeneous Catalysis. *Prog Surf Sci* **2004**, *77* (3–4), 71–137. https://doi.org/10.1016/J.PROGSURF.2004.09.001.

(103) Gennero De Chialvo, M. R.; Chialvo, A. C. Kinetics of Hydrogen Evolution Reaction with Frumkin Adsorption: Re-Examination of the Volmer-Heyrovsky and Volmer-Tafel Routes. *Electrochim Acta* **1998**, *44* (5), 841–851. https://doi.org/10.1016/S0013-4686(98)00233-3.

(104) Holewinski, A.; Linic, S. Elementary Mechanisms in Electrocatalysis: Revisiting the ORR Tafel Slope. *J Electrochem Soc* **2012**, *159* (11), H864–H870. https://doi.org/10.1149/2.022211JES/XML.

(105) Miller, J. H.; Bhan, A. Kinetic Modeling of Acrolein Oxidation Over a Promoted Mo−V Oxide Catalyst. *ChemCatChem* **2018**, *10* (23), 5511–5522. https://doi.org/10.1002/cctc.201801029.

(106) Che-Galicia, G.; Quintana-Solórzano, R.; Ruiz-Martínez, R. S.; Valente, J. S.; Castillo-Araiza, C. O. Kinetic Modeling of the Oxidative Dehydrogenation of Ethane to Ethylene over a MoVTeNbO Catalytic System. *Chemical Engineering Journal* **2014**, *252*, 75–88. https://doi.org/10.1016/J.CEJ.2014.04.042.

(107) Lee, C. W.; Cho, N. H.; Im, S. W.; Jee, M. S.; Hwang, Y. J.; Min, B. K.; Nam, K. T. New Challenges of Electrokinetic Studies in Investigating the Reaction Mechanism of Electrochemical CO2 Reduction. *J Mater Chem A Mater* **2018**, *6* (29), 14043–14057. https://doi.org/10.1039/C8TA03480J.

(108) Limaye, A. M.; Zeng, J. S.; Willard, A. P.; Manthiram, K. Bayesian Data Analysis Reveals No Preference for Cardinal Tafel Slopes in CO2 Reduction Electrocatalysis. *Nature Communications 2021 12:1* **2021**, *12* (1), 1–10. https://doi.org/10.1038/s41467-021-20924-y.

(109) Rae, K.; Corpus, M.; Bui, J. C.; Limaye, A. M.; Pant, L. M.; Manthiram, K.; Weber, A. Z.; Bell, A. T. Beyond Tafel Analysis for Electrochemical CO2 Reduction. **2022**. https://doi.org/10.26434/CHEMRXIV-2022-9RX0M.

(110) Woodhouse, M.; Parkinson, B. A. Combinatorial Approaches for the Identification and Optimization of Oxide Semiconductors for Efficient Solar Photoelectrolysis. *Chem Soc Rev* **2008**, *38* (1), 197–210. https://doi.org/10.1039/B719545C.

(111) Muster, T. H.; Trinchi, A.; Markley, T. A.; Lau, D.; Martin, P.; Bradbury, A.; Bendavid, A.; Dligatch, S. A Review of High Throughput and Combinatorial Electrochemistry. *Electrochim Acta* **2011**, *56* (27), 9679–9699. https://doi.org/10.1016/J.ELECTACTA.2011.09.003.

(112) Guevarra, D.; Haber, J. A.; Wang, Y.; Zhou, L.; Kan, K.; Richter, M. H.; Gregoire, J. M. High Throughput Discovery of Complex Metal Oxide Electrocatalysts for the

Oxygen Reduction Reaction. *Electrocatalysis* **2022**, *13* (1), 1–10. https://doi.org/10.1007/S12678-021-00694-3/FIGURES/7.

(113) Lai, Z.; Zou, Y.; Zhao, Z.; Huang, F.; Liu, P.; Lai, T.; Jin, Y. An Automated Test Platform for High-Throughput Micro-Electrochemical Characterization of Metallic Materials and Its Application on a Fe–Cr–Ni Combinatorial Materials Chip. *J Electrochem Soc* **2021**, *168* (9), 091501. https://doi.org/10.1149/1945-7111/AC24BC.

(114) Gregoire, J. M.; Xiang, C.; Liu, X.; Marcin, M.; Jin, J. Scanning Droplet Cell for High Throughput Electrochemical and Photoelectrochemical Measurements. *Review of Scientific Instruments* **2013**, *84* (2), 024102. https://doi.org/10.1063/1.4790419.

(115) Neyerlin, K. C.; Bugosh, G.; Forgie, R.; Liu, Z.; Strasser, P. Combinatorial Study of High-Surface-Area Binary and Ternary Electrocatalysts for the Oxygen Evolution Reaction. *J Electrochem Soc* **2009**, *156* (3), B363. https://doi.org/10.1149/1.3049820/XML.

(116) Kolen, M.; Antoniadis, G.; Schreuders, H.; Boshuizen, B.; Noordenne, D. D. van; Ripepi, D.; Smith, W. A.; Mulder, F. M. Combinatorial Screening of Bimetallic Electrocatalysts for Nitrogen Reduction to Ammonia Using a High-Throughput Gas Diffusion Electrode Cell Design. *J Electrochem Soc* **2022**, *169* (12), 124506. https://doi.org/10.1149/1945-7111/ACA6A7.

(117) Rein, J.; Annand, J. R.; Wismer, M. K.; Fu, J.; Siu, J. C.; Klapars, A.; Strotman, N. A.; Kalyani, D.; Lehnherr, D.; Lin, S. Unlocking the Potential of High-Throughput Experimentation for Electrochemistry with a Standardized Microscale Reactor. *ACS Cent Sci* **2021**, *7* (8), 1347–1355. https://doi.org/10.1021/ACSCENTSCI.1C00328/SUPPL_FILE/OC1C00328_SI_004.MP4.

(118) Xie, M.; Shen, Y.; Ma, W.; Wei, D.; Zhang, B.; Wang, Z.; Wang, Y.; Zhang, Q.; Xie, S.; Wang, C.; Wang, Y. Fast Screening for Copper-Based Bimetallic Electrocatalysts: Efficient Electrocatalytic Reduction of CO2 to C2+ Products on Magnesium-Modified Copper. *Angewandte Chemie* **2022**, *134* (51), e202213423. https://doi.org/10.1002/ANGE.202213423.

(119) Jones, R. J. R.; Wang, Y.; Lai, Y.; Shinde, A.; Gregoire, J. M. Reactor Design and Integration with Product Detection to Accelerate Screening of Electrocatalysts for

Carbon Dioxide Reduction. *Review of Scientific Instruments* **2018**, *89* (12), 124102. https://doi.org/10.1063/1.5049704.

(120) Lai, Y.; Watkins, N. B.; Rosas-Hernández, A.; Thevenon, A.; Heim, G. P.; Zhou, L.; Wu, Y.; Peters, J. C.; Gregoire, J. M.; Agapie, T. Breaking Scaling Relationships in CO2Reduction on Copper Alloys with Organic Additives. *ACS Cent Sci* **2021**, *7* (10), 1756–1762. https://doi.org/10.1021/ACSCENTSCI.1C00860/ASSET/IMAGES/LARGE/OC1C00860_0004.JPEG.

(121) Lai, Y.; Watkins, N. B.; Muzzillo, C.; Richter, M.; Kan, K.; Zhou, L.; Haber, J. A.; Zakutayev, A.; Peters, J. C.; Agapie, T.; Gregoire, J. M. Molecular Coatings Improve the Selectivity and Durability of CO2 Reduction Chalcogenide Photocathodes. *ACS Energy Lett* **2022**, *7* (3), 1195–1201. https://doi.org/10.1021/ACSENERGYLETT.1C02762/SUPPL_FILE/NZ1C02762_SI_001.PDF.

(122) Weissermel, K.; Arpe, H.-J. *Industrial Organic Chemistry*, Fourth, Co.; WILEY-VCH Verlag, 2003.

(123) Franke, R.; Selent, D.; Börner, A. Applied Hydroformylation. *Chem Rev* **2012**, *112* (11), 5675–5732. https://doi.org/10.1021/CR3001803/ASSET/IMAGES/CR3001803.SOCIAL.JPEG_V03.

(124) Zhang, B.; Peña Fuentes, D.; Börner, A. Hydroformylation. *ChemTexts* **2022**, *8* (1), 1–26. https://doi.org/10.1007/S40828-021-00154-X/FIGURES/45.

(125) Kohlpaintner, C.; Schulte, M.; Falbe, J.; Lappe, P.; Weber, J.; Frey, G. D. Aldehydes, Aliphatic. *Ullmann's Encyclopedia of Industrial Chemistry* **2013**. https://doi.org/10.1002/14356007.A01_321.PUB3.

(126) Resasco, J.; Bell, A. T. Electrocatalytic CO2 Reduction to Fuels: Progress and Opportunities. *Trends Chem* **2020**, *2* (9), 825–836. https://doi.org/10.1016/J.TRECHM.2020.06.007.

(127) Birdja, Y. Y.; Pérez-Gallent, E.; Figueiredo, M. C.; Göttle, A. J.; Calle-Vallejo, F.; Koper, M. T. M. Advances and Challenges in Understanding the Electrocatalytic

Conversion of Carbon Dioxide to Fuels. *Nature Energy 2019 4:9* **2019**, *4* (9), 732–745. https://doi.org/10.1038/s41560-019-0450-y.

(128) Ren, D.; Wong, N. T.; Handoko, A. D.; Huang, Y.; Yeo, B. S. Mechanistic Insights into the Enhanced Activity and Stability of Agglomerated Cu Nanocrystals for the Electrochemical Reduction of Carbon Dioxide to N-Propanol. *Journal of Physical Chemistry Letters* **2016**, *7* (1), 20–24. https://doi.org/10.1021/ACS.JPCLETT.5B02554/ASSET/IMAGES/LARGE/JZ-2015-025548_0005.JPEG.

(129) Pan, F.; Yang, Y. Designing CO2 Reduction Electrode Materials by Morphology and Interface Engineering. *Energy Environ Sci* **2020**, *13* (8), 2275–2309. https://doi.org/10.1039/D0EE00900H.

(130) Otsuka, K.; Ando, T.; Yamanaka, I. Hydroformylation of Ethylene via Spontaneous Cell Reactions in the Gas Phase. *J Catal* **1997**, *165* (2), 221–230. https://doi.org/10.1006/jcat.1997.1472.

(131) Amsler, J.; Sarma, B. B.; Agostini, G.; Prieto, G.; Plessow, P. N.; Studt, F. Prospects of Heterogeneous Hydroformylation with Supported Single Atom Catalysts. *J Am Chem Soc* **2020**. https://doi.org/10.1021/jacs.9b12171.

(132) Ro, I.; Xu, M.; Graham, G. W.; Pan, X.; Christopher, P. Synthesis of Heteroatom Rh-ReOx Atomically Dispersed Species on Al2O3 and Their Tunable Catalytic Reactivity in Ethylene Hydroformylation. *ACS Catal* **2019**, *9* (12), 10899–10912. https://doi.org/10.1021/ACSCATAL.9B02111/SUPPL_FILE/CS9B02111_SI_001.PDF.

(133) Lawrance, G. A. Coordinated Trifluoromethanesulfonate and Fluorosulfate. *Chem Rev* **1986**, *86* (1), 17–33. https://doi.org/10.1021/CR00071A002/ASSET/CR00071A002.FP.PNG_V03.

(134) Zhao, J.; He, Y.; Wang, F.; Zheng, W.; Huo, C.; Liu, X.; Jiao, H.; Yang, Y.; Li, Y.; Wen, X. Suppressing Metal Leaching in a Supported Co/SiO2 Catalyst with Effective Protectants in the Hydroformylation Reaction. *ACS Catal* **2020**, *10* (2), 914–920. https://doi.org/10.1021/ACSCATAL.9B03228/ASSET/IMAGES/LARGE/CS9B03228_0006.JPEG.

(135) Ro, I.; Qi, J.; Lee, S.; Xu, M.; Yan, X.; Xie, Z.; Zakem, G.; Morales, A.; Chen, J. G.; Pan, X.; Vlachos, D. G.; Caratzoulas, S.; Christopher, P. Bifunctional Hydroformylation on Heterogeneous Rh-WOx Pair Site Catalysts. *Nature 2022 609:7926* **2022**, *609* (7926), 287–292. https://doi.org/10.1038/s41586-022-05075-4.

(136) Leshchev, D.; Rakitin, M.; Luvizotto, B.; Kadyrov, R.; Ravel, B.; Attenkofer, K.; Stavitski, E. The Inner Shell Spectroscopy Beamline at NSLS-II: A Facility for in Situ and Operando X-Ray Absorption Spectroscopy for Materials Research. *J Synchrotron Radiat* **2022**, *29* (4), 1095–1106. https://doi.org/10.1107/S160057752200460X/YE5015SUP1.PDF.

(137) Ravel, B.; Newville, M. ATHENA, ARTEMIS, HEPHAESTUS: Data Analysis for X-Ray Absorption Spectroscopy Using IFEFFIT. *J Synchrotron Radiat* **2005**, *12* (4), 537–541. https://doi.org/10.1107/S0909049505012719.

(138) Matsubu, J. C.; Yang, V. N.; Christopher, P. Isolated Metal Active Site Concentration and Stability Control Catalytic CO2 Reduction Selectivity. *J Am Chem Soc* **2015**, *137* (8), 3076–3084. https://doi.org/10.1021/JA5128133/SUPPL_FILE/JA5128133_SI_001.PDF.

(139) Farpón, M. G.; Henao, W.; Plessow, P. N.; Andrés, E.; Arenal, R.; Marini, C.; Agostini, G.; Studt, F.; Prieto, G. Rhodium Single-Atom Catalyst Design through Oxide Support Modulation for Selective Gas-Phase Ethylene Hydroformylation. *Angewandte Chemie International Edition* **2022**, e202214048. https://doi.org/10.1002/ANIE.202214048.

(140) Koshy, D. M.; Nathan, S. S.; Asundi, A. S.; Abdellah, A. M.; Dull, S. M.; Cullen, D. A.; Higgins, D.; Bao, Z.; Bent, S. F.; Jaramillo, T. F. Bridging Thermal Catalysis and Electrocatalysis: Catalyzing CO2 Conversion with Carbon-Based Materials. *Angewandte Chemie International Edition* **2021**, *60* (32), 17472–17480. https://doi.org/10.1002/ANIE.202101326.

(141) Stonehart, P.; Ross, P. N. The Commonality of Surface Processes in Electrocatalysis and Gas-Phase Heterogeneous Catalysis. *http://dx.doi.org/10.1080/01614947508067520* **2006**, *12* (1), 1–35. https://doi.org/10.1080/01614947508067520.

(142) Blurton, K. F.; Stetter, J. R. The Gas Phase and Electrochemical Oxidation of Carbon Monoxide on Platinum, Palladium and Ruthenium Catalysts: A Comparative Study. *J Catal* **1977**, *46* (2), 230–233. https://doi.org/10.1016/0021-9517(77)90203-2.

(143) Bates, J. S.; Biswas, S.; Suh, S. E.; Johnson, M. R.; Mondal, B.; Root, T. W.; Stahl, S. S. Chemical and Electrochemical O2 Reduction on Earth-Abundant M-N-C Catalysts and Implications for Mediated Electrolysis. *J Am Chem Soc* **2022**, *144* (2), 922–927. https://doi.org/10.1021/JACS.1C11126/ASSET/IMAGES/LARGE/JA1C11126_0005.JPEG.

(144) Adams, J. S.; Kromer, M. L.; Rodríguez-López, J.; Flaherty, D. W. Unifying Concepts in Electro- And Thermocatalysis toward Hydrogen Peroxide Production. *J Am Chem Soc* **2021**, *143* (21), 7940–7957. https://doi.org/10.1021/JACS.0C13399/ASSET/IMAGES/LARGE/JA0C13399_0008.JPEG.

(145) Ryu, J.; Bregante, D. T.; Howland, W. C.; Bisbey, R. P.; Kaminsky, C. J.; Surendranath, Y. Thermochemical Aerobic Oxidation Catalysis in Water Can Be Analysed as Two Coupled Electrochemical Half-Reactions. *Nature Catalysis 2021 4:9* **2021**, *4* (9), 742–752. https://doi.org/10.1038/s41929-021-00666-2.

(146) Howland, W. C.; Gerken, J. B.; Stahl, S. S.; Surendranath, Y. Thermal Hydroquinone Oxidation on Co/N-Doped Carbon Proceeds by a Band-Mediated Electrochemical Mechanism. *J Am Chem Soc* **2022**, *144* (25), 11253–11262. https://doi.org/10.1021/JACS.2C02746/ASSET/IMAGES/LARGE/JA2C02746_0011.JPEG.

(147) Singh, N.; Sanyal, U.; Ruehl, G.; Stoerzinger, K. A.; Gutiérrez, O. Y.; Camaioni, D. M.; Fulton, J. L.; Lercher, J. A.; Campbell, C. T. Aqueous Phase Catalytic and Electrocatalytic Hydrogenation of Phenol and Benzaldehyde over Platinum Group Metals. *J Catal* **2020**, *382*, 372–384. https://doi.org/10.1016/J.JCAT.2019.12.034.

(148) Wang, Z.; Ortiz, E. M.; Goldsmith, B. R.; Singh, N. Comparing Electrocatalytic and Thermocatalytic Conversion of Nitrate on Platinum–Ruthenium Alloys. *Catal Sci Technol* **2021**, *11* (21), 7098–7109. https://doi.org/10.1039/D1CY01075A.

(149) Liu, J.; Lu, L.; Wood, D.; Lin, S. New Redox Strategies in Organic Synthesis by Means of Electrochemistry and Photochemistry. *ACS Cent Sci* **2020**, *6* (8), 1317–1340. https://doi.org/10.1021/ACSCENTSCI.0C00549/ASSET/IMAGES/LARGE/OC0C00549_0033.JPEG.

(150) Ackermann, L. Metalla-Electrocatalyzed C-H Activation by Earth-Abundant 3d Metals and Beyond. *Acc Chem Res* **2020**, *53* (1), 84–104.

https://doi.org/10.1021/ACS.ACCOUNTS.9B00510/ASSET/IMAGES/LARGE/AR9B00510_0041.JPEG.

(151) Shrestha, A.; Lee, M.; Dunn, A. L.; Sanford, M. S. Palladium-Catalyzed C-H Bond Acetoxylation via Electrochemical Oxidation. *Org Lett* **2018**, *20* (1), 204–207. https://doi.org/10.1021/ACS.ORGLETT.7B03559/ASSET/IMAGES/LARGE/OL-2017-035594_0004.JPEG.

(152) Delano, T. J.; Reisman, S. E. Enantioselective Electroreductive Coupling of Alkenyl and Benzyl Halides via Nickel Catalysis. *ACS Catal* **2019**, *9* (8), 6751–6754. https://doi.org/10.1021/ACSCATAL.9B01785/SUPPL_FILE/CS9B01785_SI_001.PDF.

(153) Perkins, R. J.; Hughes, A. J.; Weix, D. J.; Hansen, E. C. Metal-Reductant-Free Electrochemical Nickel-Catalyzed Couplings of Aryl and Alkyl Bromides in Acetonitrile. *Org Process Res Dev* **2019**, *23* (8), 1746–1751. https://doi.org/10.1021/ACS.OPRD.9B00232/SUPPL_FILE/OP9B00232_SI_001.PDF.

(154) Gorbunov, D.; Safronova, D.; Kardasheva, Y.; Maximov, A.; Rosenberg, E.; Karakhanov, E. New Heterogeneous Rh-Containing Catalysts Immobilized on a Hybrid Organic-Inorganic Surface for Hydroformylation of Unsaturated Compounds. *ACS Appl Mater Interfaces* **2018**, *10* (31), 26566–26575. https://doi.org/10.1021/acsami.8b02797.

(155) Liu, B.; Huang, N.; Wang, Y.; Lan, X.; Wang, T. Promotion of Inorganic Phosphorus on Rh Catalysts in Styrene Hydroformylation: Geometric and Electronic Effects. *ACS Catal* **2021**, *11* (3), 1787–1796. https://doi.org/10.1021/ACSCATAL.0C04684/ASSET/IMAGES/LARGE/CS0C04684_0008.JPEG.

(156) Brown, C. K.; Wilkinson, G. Homogeneous Hydroformylation of Alkenes with Hydridocarbonyltris-(Triphenylphosphine)Rhodium(I) as Catalyst. *Journal of the Chemical Society A: Inorganic, Physical, Theoretical* **1970**, No. 0, 2753–2764. https://doi.org/10.1039/J19700002753.

(157) Seiche, W.; Schuschkowski, A.; Breit, B. Bidentate Ligands by Self-Assembly through Hydrogen Bonding: A General Room Temperature/Ambient Pressure Regioselective Hydroformylation of Terminal Alkenes. *Adv Synth Catal* **2005**, *347* (11–13), 1488–1494. https://doi.org/10.1002/ADSC.200505174.

(158) Vengatesan, S.; Cho, E.; Kim, H.-J.; Lim, T.-H. Effects of Curing Condition of Solution Cast Nafion® Membranes on PEMFC Performance. *Korean J. Chem. Eng* **2009**, *26* (3), 679–684.

(159) Williams, K.; Limaye, A.; Weiss, T.; Chung, M.; Manthiram, K. Accounting for Species' Thermodynamic Activities Changes Mechanistic Interpretations of Electrochemical Kinetic Data. **2022**. https://doi.org/10.26434/CHEMRXIV-2022-VK5Z9.

(160) Chu, A. T.; Surendranath, Y. Aprotic Solvent Exposes an Altered Mechanism for Copper-Catalyzed Ethylene Electrosynthesis. *J Am Chem Soc* **2022**, *144* (12), 5359–5365. https://doi.org/10.1021/JACS.1C12595/SUPPL_FILE/JA1C12595_SI_001.PDF.

(161) Roberts, J. A. S.; Bullock, R. M. Direct Determination of Equilibrium Potentials for Hydrogen Oxidation/Production by Open Circuit Potential Measurements in Acetonitrile. *Inorg Chem* **2013**, *52* (7), 3823–3835. https://doi.org/10.1021/IC302461Q/SUPPL_FILE/IC302461Q_SI_002.XLSX.

(162) Pujiastuti, S.; Onggo, H. Effect of Various Concentration of Sulfuric Acid for Nafion Membrane Activation on the Performance of Fuel Cell. In *AIP Conference Proceedings*; American Institute of Physics Inc., 2016; Vol. 1711. https://doi.org/10.1063/1.4941639.

(163) Wuttig, A.; Surendranath, Y. Impurity Ion Complexation Enhances Carbon Dioxide Reduction Catalysis. *ACS Catal* **2015**, *5* (7), 4479–4484. https://doi.org/10.1021/acscatal.5b00808.

(164) Chlistunoff, J.; Sansiñena, J. M. On the Use of Nafion® in Electrochemical Studies of Carbon Supported Oxygen Reduction Catalysts in Aqueous Media. *Journal of Electroanalytical Chemistry* **2016**, *780*, 134–146. https://doi.org/10.1016/j.jelechem.2016.09.014.

(165) O'Reilly, J. E. Oxidation-Reduction Potential of the Ferro-Ferricyanide System in Buffer Solutions. *BBA - Bioenergetics* **1973**, *292* (3), 509–515. https://doi.org/10.1016/0005-2728(73)90001-7.

(166) *Solubilities of Gases in Water at 293 K*. https://www.wiredchemist.com/chemistry/data/solubilities-gases (accessed 2022-11-20).

(167) Tenner, S. P.; Walnwright, M. S.; Trlmm, D. L.; Cant, N. W. Solubility of Carbon Monoxide in Alcohols. *J Chem Eng Data* **1983**, *28* (1), 59–61. https://doi.org/10.1021/JE00031A017.

(168) *NIST WebBook*. https://webbook.nist.gov/ (accessed 2022-12-04).

7 APPENDICES

APPENDIX A: ADDITIONAL CONSIDERATIONS FOR KINETIC ANALYSIS OF CO_2RR AT COBALT PHTHALOCYANINE

A.1 Experimental procedures

A.1.1 Electrode preparation

Disc shaped electrodes with a diameter of 12 millimeters were punched from carbon paper (Toray, TGP-H-060, Fuel Cell Earth LLC) and inserted into a preheated tube furnace at 800 °C in static air for 10 min to generate oxygen-functionalized carbon paper (OxCP).

Catalyst ink was prepared by dispersing 10 mg of Cobalt(II) Phthalocyanine (CoPc, Strem Chemicals, Lot 24745700) in a mixture of 25 µL of 20 wt.% Nafion solution (D2021 Nafion dispersion, Fuel Cell Store) and 9974.5 µL N,N-dimethylformamide (DMF, Sigma Aldrich, 99.8%) with 15 minutes of sonication to yield a final solution containing a CoPc concentration of 1.75 x 10^{-3} mol/L. This solution was then serially diluted in DMF to obtain catalyst inks containing CoPc concentrations ranging from 2 x 10^{-7} to 4.38 x 10^{-6} mol/L CoPc, with the corresponding Nafion content ranging from 6.25 to 12.5 × 10^{-4} mg/ml (for the 4.38 x 10^{-6} mol/L CoPc ink, the color of the solution was just barely blue). The specific loading of the catalyst, corresponding to the ink with CoPc concentration of 4.38 x 10^{-6} mol/L, did not affect the measurement of turnover frequencies (Figure A-A8).

The CoPc/OxCP working electrode was then prepared by dropcasting 15 µL of freshly sonicated ink onto the center of OxCP. The droplet instantaneously spread throughout the entire carbon paper without penetrating onto the underlying aluminum foil. The electrode was then oven-dried in air at 80 °C for 10 min. Fresh ink was prepared every time a new batch of electrodes was made, and electrodes were used within 24 hours of preparation. This is because there was a noticeable decrease in activity when electrodes were prepared from ink that was more than several days old or using electrodes that had been prepared even just one or two days prior. Catalyst loading was kept below 5.8 x 10^{-11} mol/cm^2.

A.1.2 Electrochemical testing

Electrochemical measurements were conducted in a previously reported,[51] customized three-compartment cell (Figure A-A1) fabricated from polycarbonate, containing a counter electrode compartment, working electrode compartment, and gas compartment. The working electrode compartment was separated from the counter electrode compartment by an activated[162] Nafion

membrane (Nafion117, Fuel Cell Store). The counter and reference electrodes were platinum foil (99.9% metals basis, Alfa Aesar) and Ag/AgCl leak-free reference (LF-2, Innovative Instrument Inc.), respectively. The leak-free reference was calibrated every day before use against a saturated calomel electrode, (CHI150, CH Instruments) in a saturated potassium chloride solution (The potential at the SCE was assumed to be, according the manufacturer specification, +0.241V vs SHE at 25ºC). CoPc/OxCP electrode was placed between the working electrode compartment and gas compartment.

Prior to experiments, 1.75 mL of CO_2-saturated electrolyte of specified composition was added into the working electrode compartment and counter electrode compartment, respectively. High-purity CO_2 gas (Airgas, 99.999%, 10 sccm) was controlled by an Alicat mass flow controller and introduced into the cell at atmospheric pressure; CO_2 gas entered the cell through the gas compartment, traversed the working electrode, and exited through the working electrode compartment and flowed directly to an on-line gas chromatograph (SRI Instruments, Inc., MG #5, Model 8610C). The anode compartment was not purged and was left open to atmosphere. The working compartment was purged with CO_2 for 5 min before electrochemical polarization. For CO_2 order dependence tests, the working compartment was purged with CO_2 for 30 min before polarization. Cells were disassembled and rinsed with MilliQ water, and a fresh electrode was used for each test.

The electrochemical measurements were controlled with a VMP3 Multi-channel potentiostat. Resistance between the reference and working electrodes was measured with Potential Electrochemical Impedance Spectroscopy (PEIS) and automatically compensated by 85%. The remaining 15% was not manually compensated, but because the cell resistance was always around 10 ohms, and operating currents were usually less than 1 mA (and were at most 4 mA), 15% of the IR drop should have been at most 1 mV, if not significantly less. For all experiments, the reaction was run for a total of 20 minutes, with gas products analyzed by an on-line gas chromatograph (SRI Instruments) every 5 minutes. The rates reported are calculated from average of the products detected at the 10, 15, and 20 minute marks. Data collection began after 10 minutes to ensure that the sampled gas headspace composition reflected steady state conditions. The gas chromatograph was equipped with a thermal conductivity detector (TCD) and flame ionization detector (FID), a methanizer, and a Hayesep-D column. Every 5 minutes, sample flowing through the sample loop was flowed to the Hayesep-D column, where it flowed to the FID and TCD. CO_2 eluted after CO, and flow to the FID was diverted during the times at which CO_2 was expected to elute. Column temperature was maintained at 100ºC. Each run

was 3.5 minutes long. Sample chromatograms from the FID and TCD are provided in Figure A-A2.

For the experiments where CO_2 partial pressure was varied, the total flow rate and pressure were kept constant by adding in a diluent stream of nitrogen. 1M sodium bicarbonate electrolytes were prepared by bubbling CO_2 (Airgas, 99.999% research grade) through 0.5M sodium carbonate (Sigma Aldrich, 99.999% trace metal basis) solution (prepared with MilliQ ultrapure water) overnight. To test the order dependence on bicarbonate at constant ionic strength, sodium perchlorate (Sigma Aldrich, ≥ 98.0%) was used as supporting electrolyte. For order dependence tests, sodium bicarbonate concentration was varied by mixing the 1M sodium bicarbonate solution in an appropriate ratio with the 1M sodium perchlorate solution. For all kinetic tests, constant voltage vs the Ag/AgCl leak free reference (i.e., a pH-independent reference) was used.

Kinetic isotope effect experiments were performed by preparing electrolytes of Na_2CO_3 and $NaClO_4$ identically as mentioned above, but using D_2O (Oakwood Chemical, Lot No. 044626K20K) instead of H_2O as the solvent.

Both the sodium bicarbonate and sodium perchlorate solutions were treated with Chelex resin (Chelex 100 sodium form, Sigma Aldrich, prepared according to previously reported procedures[163]) before use as a precaution against electrolyte impurities, which are known to cause issues for bulk metal foil catalysts. Notably, this treatment appeared to have very little effect, probably due to the mostly carbonaceous nature of the electrode used in this work (Figure A-A16).

Turnover frequency, defined as the reaction rate at each site, was calculated by assuming all deposited catalyst molecules were active. Thus, the formula for turnover frequency was:

$$TOF_{CO} = \frac{[CO] * v_{out}}{\rho_{CoPc} * A_{elec}}$$

Where $[CO]$ is the concentration of CO detected in the product stream in mol/cm^3, v_{out} is the flow rate of gas exiting the cell in cm^3/s (notably, the amount of H_2 evolution is small and any water vapor from the electrolyte was also assumed to be small, so this is assumed to be the input flow rate, 10 sccm), ρ_{CoPc} is the loading of CoPc deposited on the electrode in mol/cm^2 and A_{elec} is the active (exposed) area of the electrode, assumed to reflect the size of the electrode hole in the working compartment (specifically, 1 cm^2, though notably, 1 cm^2 is slightly smaller than the area of the entire physical electrode).

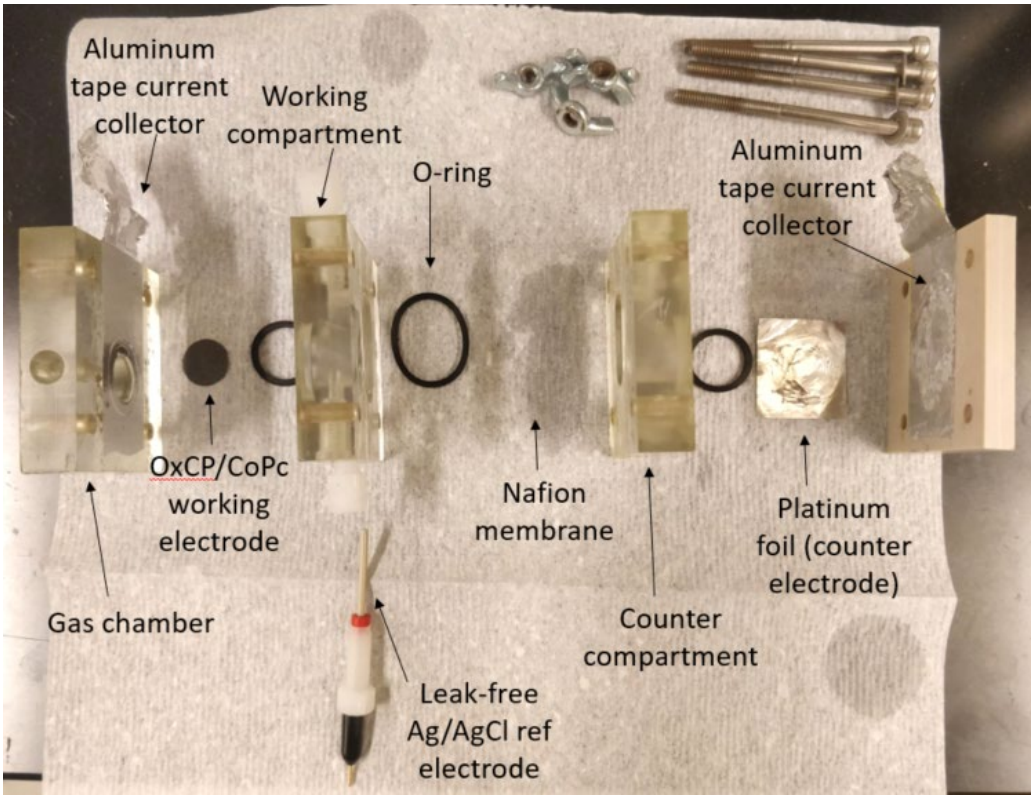

Figure A-A1. Setup of 3 compartment cell used in experiments

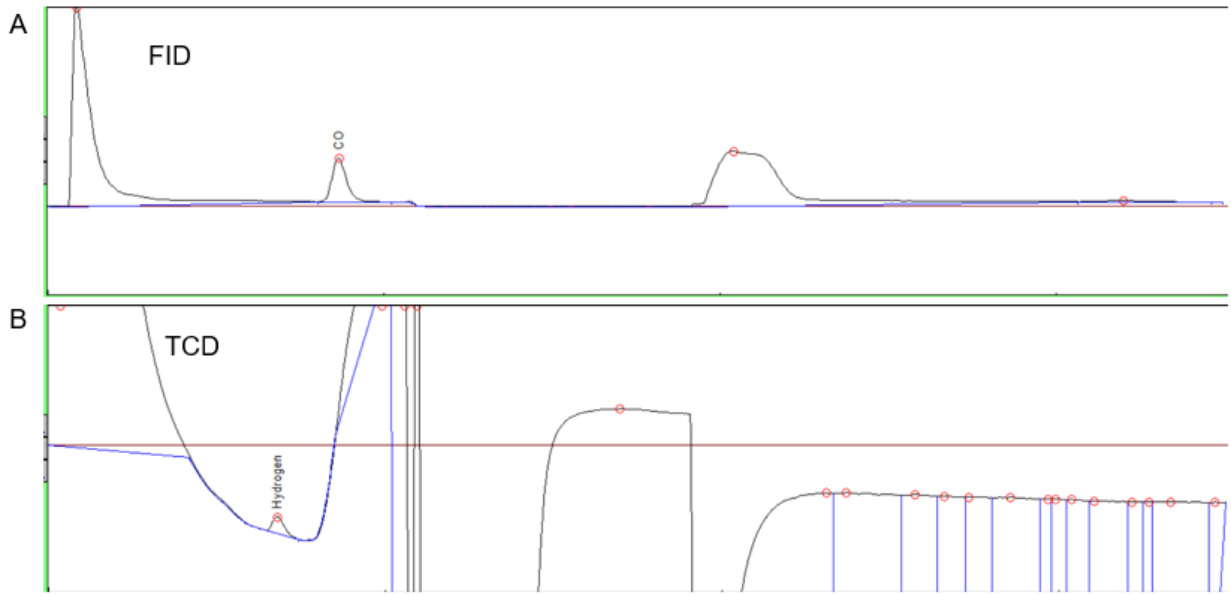

Figure A-A2. Sample chromatographs for the (A) FID and (B) TCD.

A.1.3 Precise nomenclature of tetrapyrrolic compounds

Various compounds were referenced in the main text. More precise nomenclature is enumerated below:

- Cobalt tetraphenyl porphyrin: 5,10,15,20-Tetraphenyl-21H,23H-porphine cobalt(II)

- Cobalt tetraaminophenyl porphyrin: 5,10,15,20-tetrakis(4-aminophenyl)porphinato cobalt
- Perfluorinated cobalt phthalocyanine: Cobalt(II) 1,2,3,4,8,9,10,11,15,16,17,18,22,23,24,25-hexadecafluoro-29H,31H-phthalocyanine

A.2 Considerations related to equilibria of electrolyte species

A.2.1 Details of equilibrium calculations

Modeling of equilibrium and transport in CO_2RR systems was based on a previous report in the literature.[80] Equilibrium species concentrations were numerically calculated in Matlab. The following relevant constants were used:

Physical context	**Value**
Eq constant for $CO_2(aq) + H_2O \rightarrow H^+ + HCO_3^-$	$10^{-6.37}*1000$ mol/m^3
Eq constant for $HCO_3^- \rightarrow H^+ + CO_3^{2-}$	$10^{-10.25}*1000$ mol/m^3
Eq constant for $H_2O \rightarrow H^+ + OH^-$	$10^{-14}*1000^2$ (mol/m^3)^2
Sechenov Coefficient for H^+ (h_{s,H^+})	0
Sechenov Coefficient for OH^- (h_{s,OH^-})	8.39 x 10^{-5} m^3/mol
Sechenov Coefficient for HCO_3^- (h_{s,HCO_3^-})	9.67 x 10^{-5} m^3/mol
Sechenov Coefficient for CO_3^{2-} ($h_{s,CO_3^{2-}}$)	14.23 x 10^{-5} m^3/mol
Sechenov Coefficient for K^+ (h_{s,K^+})	9.22 x 10^{-5} m^3/mol

Table A-A1. Constants used for electrolyte equilibrium calculation

Activities of ionic species were accounted for using Davie's equation:

$$a_i = C_i * 10^{-0.51*z_i^2*(\frac{\sqrt{I}}{1+\sqrt{I}}-0.3I)}$$

Where a_i is activity of species i, C_i is the concentration of species i, z_i is the charge on species i, and I is the total ionic strength of the solution, in mol/m^3, given by:

$$I = 0.5 * \sum_i z_i^2 * C_{i,o}$$

Where $C_{i,o}$ is the initial concentration of species i. Activity of dissolved CO_2 was calculated using Henry's law:

$$a_{CO_2} = H_{CO_2} * p_{CO_2}$$

Where p_{CO_2} is the partial pressure of CO_2 in atm and H_{CO_2} is Henry's constant, and calculated for CO_2 as:

$$H_{CO_2} = e^{(93.4517*\frac{100}{T} - 60.2409 + 23.3585*\log(\frac{T}{100}))}$$

Where T is the temperature in Kelvin. Concentration of CO_2 in the electrolyte (mol/m^3) was calculated as:

$$C_{CO_2} = a_{CO_2} / \gamma_{CO_2}$$

Where γ_{CO_2} is the activity coefficient of CO_2:

$$\gamma_{CO_2} = e^{\sum_i C_i*(h_{s,i}+h_G)}$$

Where $h_{s,i}$ are the Sechenov coefficients for each ionic species (listed in Table A-A1 above), and h_G is the specific gas constant of CO_2, (in m^3/mol) given by:

$$h_G = -1.72x10^{-5} - 3.38x10^{-7} * (T - 298.15)$$

Concentrations of all species were solved for by enforcing that ratios of activities equaled equilibrium constants for the reactions listed in Table A-A1 above. For general reference, the following values were calculated at different concentrations of [$NaHCO_3$] at 1 atm CO_2:

[$NaHCO_3$] prepared	**[HCO_3^-] calculated**	**-$\log_{10}$([H^+])**
0 M	1.22 x 10^{-4} M	3.91
0.1 M	0.0999 M	6.62
0.5 M	0.496 M	7.26
1 M	0.988 M	7.63

Table A-A2. Calculated species concentrations at various prepared concentrations of $NaHCO_3$ and 1 atm CO_2.

A.2.2 Notes on pH changes within order dependence tests

In general, order dependence tests can only be rigorously interpreted when all conditions except the desired species concentration are held constant. It is worth noting that in both the bicarbonate order dependence test at constant P_{CO2} (main text Figure 2-1A) and CO_2 order dependence at constant bicarbonate concentration (main text Figure 2-1C), the pH technically also changes when the concentration of the independent variable is being changed. This is because the equilibrium between CO_2 and carbonic acid that is described above in Section A.2.1 implies that out of the three variables P_{CO2}, $[H_3O^+]$, and $[HCO_3^-]$, it is only possible to independently manipulate 2. Therefore, it is not physically possible to vary one of these parameters while holding the other two constant.

In this work, we exclude the kinetic relevance of $[H_3O^+]$ due to literature precedent that suggests proton concentrations near an electrode during CO_2RR are generally too low to expect $[H_3O^+]$ to be a kinetically relevant species (full discussion in main text section 2.5.1.1). Therefore, in our kinetic modeling, the variation of pH in the bicarbonate and CO_2 order dependencies mentioned would only be significant for proton transfer steps that were assumed to be in thermodynamic equilibrium (where no matter which proton donor one assumes, pH will fall out of the equilibrium expression). However, from the results of the model fitting, the proposed model, M2, only has proton transfer steps that are assumed to be irreversible (i.e., kinetically limited and not equilibrated). Therefore, the variation of electrolyte pH with different $[NaHCO_3]$ and P_{CO2} did not actually have any physical significance in the final proposed mechanism. We acknowledge that we cannot definitively exclude the possibility that H_3O^+ is actually kinetically relevant. If it were, in fact, kinetically relevant, the bicarbonate and CO_2 order dependence tests could have different physical interpretations from the ones we have provided.

To illustrate the pH change more quantitatively, in the CO_2 order dependence test at costant $[NaHCO_3]_{added}$, when P_{CO2} is changed by an order of magnitude, the pH of the bulk electrolyte also changes by about 1 pH unit. The value of $[HCO_3^-]_{calc}$ also changes, but to a much smaller extent. Thus, off unity CO_2 order dependencies could also be explained by some sort of pH dependence. Example calculated values are shown below in Table A-A3.

For $[NaHCO_3]_{added}$ = 0.05M		
P_{CO2}	pH	$[HCO_3^-]_{calc}$
1	6.37	0.050 M
0.5	6.67	0.050 M

0.1	7.36	0.050 M
For $[NaHCO_3]_{added}$ = 0.5M		
P_{CO2}	pH	$[HCO_3^-]_{calc}$
1	7.26	0.497 M
0.5	7.56	0.493 M
0.1	8.24	0.469 M

Table A-A3. Calculated equilibrium species concentrations when keeping added sodium bicarbonate salt constant while changing partial pressure of CO_2.

For the bicarbonate order dependence tests at 1 atm of CO_2, please see Table A-A2 to see how the solution pH changes.

A.3 Mass transport analyses

A.3.1 Exclusion of mass transport limitations from invariance of TOF to loading

Mass transport limitations were not considered (alternatively framed, bulk concentrations for kinetically relevant species were assumed to reflect interfacial species concentrations) mainly due to the experimental observation that turnover frequency (TOF) per molecule of CoPc deposited was, within certain limits of loading, invariant to the loading of CoPc used (Figure A-A8). That means that if 5x more catalyst was deposited, then 5x more current was drawn. If mass transport limitations were at play, if 5x more current was drawn, we would expect steeper concentration gradients near the electrode (because the boundary flux of reactants is defined by the reaction rate at the electrode), which should change (most likely decrease) the experimentally measured TOF. Because no difference in rate per active site was observed, even at different overall geometrical current densities, we assumed that interfacial species gradients due to transport limitations were not kinetically relevant, meaning that for kinetically relevant species, the bulk concentrations were likely to be a good reflection of the interfacial concentrations.

A.3.2 1D Cartesian transport model

To more rigorously test our assumption that bulk species concentrations were a good reflection of interfacial species concentrations, we implemented a 1D reaction-diffusion model. We assumed a flat, planar electrode with a static boundary layer of δ=100 microns. This is an

approximation, because the actual system in this work is a porous carbon paper electrode with gas bubbling through it.

Within the static boundary layer, the following governing equation applies:

$$D_i\left[\nabla^2 C_i + \frac{z_i F}{RT}\nabla \bullet (C_i \nabla \Phi)\right] + R_{gen,i} = 0$$

Where the first term corresponds to diffusion, the second to migration, and the last to homogeneous reaction (in this case, buffering reactions and autoionization of water). When simplifying to one dimension, the above is simplified to:

$$D_i\left[\frac{d^2 C_i}{dr^2} + \frac{z_i F}{RT}\frac{d}{dr}(C_i \frac{d\Phi}{dr})\right] + R_{gen,i} = 0$$

The above equation is additionally paired with an electroneutrality requirement:

$$\sum_i C_i z_i = 0$$

These two equations are paired with a bulk concentration boundary condition at the boundary layer interface and a flux condition at the electrode:

Boundary:

$$C_i(r = \delta) = C_{b,i}$$

Electrode:

$$D_i \frac{dC_i}{dr}(r = 0) = \nu_i * f(j_{CO})$$

Where ν_i describes the stoichiometry of the species in CO_2 reduction (ie, if it is consumed, generated, or not affected by the reaction), and $f(j_{CO})$ converts units from geometric current density to molar flux. These equations were discretized using finite differences and numerically solved in Matlab. Diffusion and rate constants were obtained from previous literature.[80]

The 1D transport model explicitly simulated the following species: K^+, HCO_3^-, CO_3^{2-}, H^+, OH^-, CO_2 (aq). We found that the concentrations of CO_3^{2-}, H^+, and OH^- deviated the most from bulk concentrations, particularly at higher currents and lower buffer concentrations. This may serve as further justification for not explicitly modeling (CO_3^{2-}, H^+, OH^-) in the kinetic model, because these interfacial species concentrations appear to be very current-sensitive (Figure A-A3).

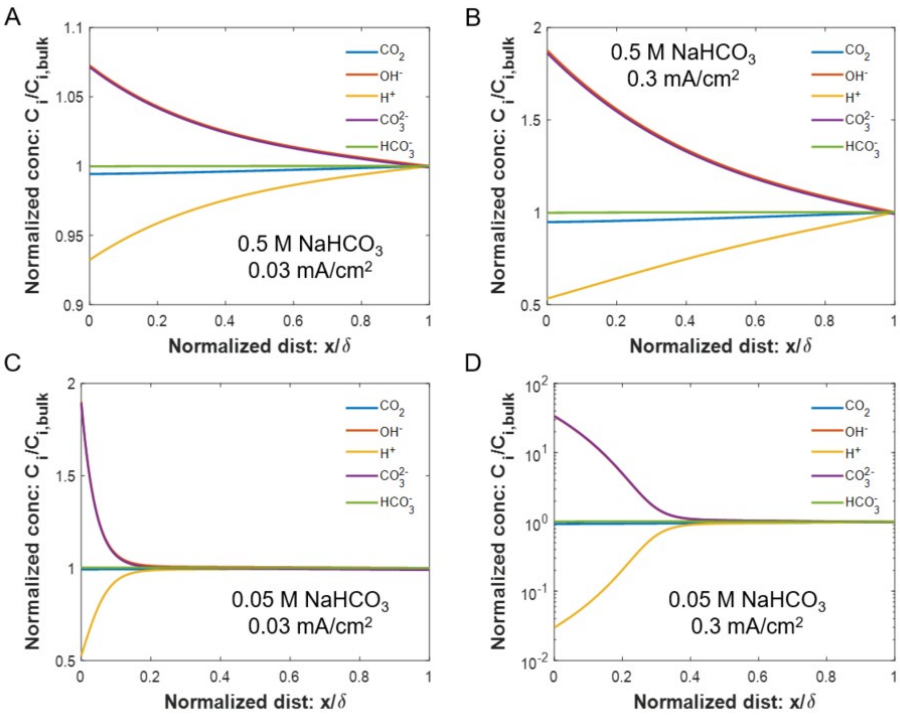

Figure A-A3. 1D Cartesian simulation of species concentrations. Carbonate (CO_3^{2-}) and hydroxide (OH^-) have identical concentration profiles. X and Y axes denote non-dimensionalized values, where concentration of species i is normalized by its bulk concentration, and distance is normalized by the boundary layer thickness, δ, which is assumed to be 100 microns. Simulations were performed at 1 atm CO_2 and (A) 0.5 M $NaHCO_3$, 0.03 mA/cm^2, (B) 0.5 M $NaHCO_3$, 0.3 mA/cm^2, (C) 0.05 M $NaHCO_3$, 0.03 mA/cm^2, (D) 0.0 5M $NaHCO_3$, 0.3 mA/cm^2.

A.3.3 1D Spherical transport model

An additional explanation for the invariance of TOF to loading could be that the isolated sites are distant enough from each other that the transport problem should be modeled locally as spherical (or hemispherical, since the catalyst is on a solid support) to the catalyst. If local spherical transport to one catalyst does not affect transport to another (i.e., the boundary layers do not coincide), then even if there were transport limitations, one would still expect TOF to be invariant with loading. We considered this possibility and excluded it, the physical rationale being mainly because the radius of the catalytic center in CoPc is very small. When transport to an object is spherically symmetric, (in the absence of homogeneous reactions), an intrinsic mass transport boundary layer will form, and at steady state the concentration profile will take the following form:

$$C_i(r) = C_i(bulk) - \frac{A_1}{r}$$

Where A_1 is a constant that can be resolved from some boundary condition at the catalyst surface and r is the spherical distance coordinate.

We also more rigorously modeled 1D spherical diffusion-reaction problem by using the same procedure as Section A.3.1 to numerically discretize and solve the following spherical conservation equation:

$$D_i\left[\frac{d^2C_i}{dr^2}+\frac{2}{r}\frac{dC_i}{dr}+\frac{z_iF}{RT}\frac{d}{dr}(C_i\frac{d\Phi}{dr})+\frac{z_iF}{RT}\frac{2}{r}C_i\frac{d\Phi}{dr}\right]+R_{gen,i}=0$$

Using the boundary conditions:

Bulk:

$$C_i(r\to\infty)=C_{b,i}$$

Electrode:

$$D_i\frac{dC_i}{dr}(r=R_{cat})=\nu_i * f(j_{CO})$$

On CoPc, we considered the radius of the active site (R_{cat}) to be 1 nm, which is a bit of an overestimation, but at much smaller length scales, the continuum limit for these bulk transport equations breaks down. We found that at TOF values of 200 s^{-1}, we did not get any significant depletion of reactants at the interface.

A.4 Considered mechanisms

A.4.1 Mathematical details – occupied sites

Occupied sites other than θ_{HCO_3} existed when certain RDS possibilities were invoked. If R3 was invoked:

$$\frac{\theta_{COO}}{\theta_o} = K_2 P_{CO2} e^{-F\phi/RT}$$

If R5 was invoked, even though HCO_3^- and H_2O were considered kinetically relevant proton donors, the thermodynamic equilibrium for extent of protonation (considering forward and reverse reactions) should be, in net, dependent on pH:

$$\frac{\theta_{H+}}{\theta_o} = K_4 [H^+]$$

If R2 and R3 were simultaneously invoked, θ_{COO} was calculated assuming steady state and assuming forward and backward reactions for R2 were at play, but that only the forward reaction of R3 was at play (because of an assumption of rapid forward reaction for the steps beyond R3). Therefore, the site balance ended up giving:

$$\frac{\theta_{COO}}{\theta_o} = \frac{k_{2f} P_{CO2} e^{-\beta_{2f} F\phi/RT}}{k_{2r} e^{(1-\beta_{2f})F\phi/RT} + k_{3f,HCO3}[HCO_3^-] + k_{3f,H2O}}$$

If R4 and R5 were simultaneously invoked, θ_{H+} was calculated using the same strategy as above to yield:

$$\frac{\theta_{H+}}{\theta_o} = \frac{k_{4f,HCO3}[HCO_3^-] + k_{4f,H2O}}{k_{5f} P_{CO2} e^{-\beta_{5f} F\phi/RT} + k_{4r,HCO3}[CO_3^{2-}] + k_{4r,H2O}[OH^-]}$$

A.4.2 Mathematical details - rate expressions

Individual rate contributions were summed to give the total rate. Below are explicit equations for the rate contribution of each RDS (subscript n indicates which Rn the rate is for). Each RDS involving a proton transfer considered both bicarbonate and water as possible proton donors.

$$r_{1HCO3} = k_{1f,HCO3} P_{CO2} [HCO_3^-] e^{-\beta_{1HCO3} F\phi/RT}$$

$$r_{1H2O} = k_{1f,H2O} P_{CO2} e^{-\beta_{1H2O} F\phi/RT}$$

$$r_2 = k_{2f} P_{CO2} e^{-\beta_{2f} F\phi/RT}$$

$$r_{3HCO3} = k_{3f,HCO3} \frac{\theta_{COO}}{\theta_o} [HCO_3^-]$$

$$r_{3H2O} = k_{3f,H2O} \frac{\theta_{COO}}{\theta_o}$$

$$r_{4HCO3} = k_{4f,HCO3} [HCO_3^-]$$

$$r_{4H2O} = k_{4f,H2O}$$

$$r_5 = k_{5f} \frac{\theta_{H+}}{\theta_o} P_{CO2} e^{-\beta_{5f} F\phi/RT}$$

If R2 and R3 were considered in series, the rate was calculated using the equations above for R3, and if R4 and R5 were considered in series, the rate was calculated using the equation above for R5. By convention, for any reaction involving water as a reactant, the activity of liquid water was assigned a value of 1.

A.4.3 Modeling details and voltage referencing

Inputs to the model were applied voltage (V vs SHE), p_{CO2}, and calculated values of $[HCO_3^-]$, $[H^+]$, $[OH^-]$, and $[CO_3^{2-}]$. In the model, 0 V for ϕ was arbitrarily set to -0.95V vs SHE. Any arbitrary 0 V reference could have been chosen, though a value within the range of voltages relevant to the data is prudent for numerical precision reasons. This arbitrary voltage reference is needed in order to calculate quantitative system properties from the fitted parameters provided in the main text.

A.4.4 Enumeration of considered mechanisms

Mechanisms were enumerated first invoking bicarbonate poisoning and one candidate RDS (Table A-A4). When none of those models fit the data, models invoking bicarbonate poisoning and mixed control between two candidate rate determining steps were considered (Table A-A5). Special cases used to test the importance of specific kinetics in the final proposed model (R1+R3+P1) are enumerated in Table A-A6.

Each table shows 1) The kinetics incorporated into the model, 2) The total number of parameters in the model, followed in parenthesis by the number of fitted parameters in the model (indeterminate or parameters that were fitted to their minimum possible value were not

considered to be fitted parameters), and 3) statistical goodness-of-fit metric, α (which used the fitted number of parameters in its calculation). Bolded entries are listed in Table 2-1 of the main text.

Mechanism	**Total # Params (Fitted # Params)**	**α value (goodness-of-fit)**
R1 + P1	**6 (6)**	**0.001**
R2 + P1	4 (4)	0.000
R3 + P1	5 (4)	0.000
R4 + P1	4 (4)	0.000
R5 + P1	5 (4)	0.000

Table A-A4. All mechanisms invoking bicarbonate poisoning and one candidate rate determining step

Mechanism	**Total # Params (Fitted # Params)**	**α value (goodness-of-fit)**
R1 + R2 + P1	**8(6)**	**0.001**
R1 + R3 + P1	**9 (9)**	**0.109**
R1 + R4 + P1	**8 (8)**	**0.001**
R1 + R5 + P1	**9 (7)**	**0.001**
R2 + R3 + P1	7(4)	0.000
R2 + R4 + P1	6 (5)	0.000
R2 + R5 + P1	**7 (6)**	**0.000**
R3 + R4 + P1	7 (6)	0.000
R3 + R5 + P1	8 (7)	0.000
R4 + R5 + P1	8 (7)	0.000

Table A-A5. All enumerated mechanisms considering bicarbonate poisoning and mixed control between two candidate rate determining steps

Mechanism	**Total # Params (Fitted # Params)**	**α value (goodness-of-fit)**
R1 + R3 + R5	**10 (10)**	**0.000**
R1 + R2 + R3 + P1	**11 (9; equiv to R1+R3+P1)**	**0.109**

Table A-A6. Specific alternative mechanisms tested against the proposed (R1+R3+P1) mechanism

A.4.5 Consideration of RDS steps involving the second electron transfer

We also briefly considered the possibility of a second electron transfer being rate determining. As such, we define R6 and R7 according to Figure A-A4.

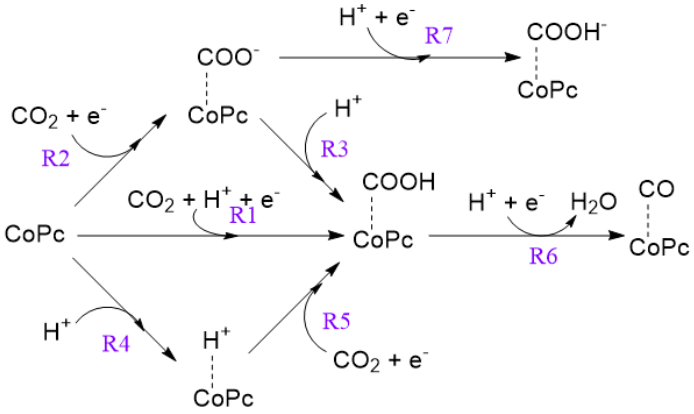

Figure A-A4. Extended illustration of possible RDS steps, including R6 and R7, which are second electron transfer steps in the catalytic cycle

We show the model fitting results for some mechanisms that considered these RDS possibilities in Table A-A7.

Mechanism	**Total # Params (Fitted # Params)**	**α value (goodness-of-fit)**
R6 + P1	7 (5)	0.000
R1 + R7 + P1	12 (9; equiv to R1+R3+P1)	0.181

Table A-A7. Enumeration of models considering the second electron transfer to be kinetically relevant

A.4.6 Consideration and exclusion of alternative anionic poisoning species

We also considered the possibility that another anion other than bicarbonate could be poisoning the catalyst, and excluded this possibility due to the following analysis: the only other anions present in the electrolyte would be perchlorate (ClO_4^-), hydroxide (OH^-), and carbonate (CO_3^{2-}). We were able to exclude perchlorate as a poisoning anion from some control perchlorate order dependence tests (Figure A-A14). We find it unlikely that hydroxide is poisoning the catalyst, because some studies have shown that at lower external buffer concentrations, the interfacial pH during CO2RR is more basic,[81] which means that a hydroxide poison should have a trend opposite to that of a bicarbonate poison.

It is possible that carbonate is a poisoning agent. However, it is difficult for us to experimentally discern this possibility from bicarbonate because (1) This effect could also be convoluted with a pH effect, because the only way to vary carbonate while keeping bicarbonate constant is to change the pH and (2) Carbonate is a minority species and also carries a -2 charge, so from both concentration and electrostatic repulsion arguments, we think bicarbonate is a more likely poison (main text, Section 2.5.1.1).

A.5 Supplemental model fitting details

A.5.1 Model fitting procedures

Parameter estimation was performed using Athena Visual software. Models were written in the mode of "Parameter Estimation" → "General form with user defined explicit models", since the expressions for rate could always be written explicitly in terms of the inputs and parameters. Parameter estimation was performed via Bayesian estimation, with a single response variable (which was ln(rate)). Gradient calculation was via central differences scheme, and lack-of-fit analysis was performed based on replicate experiments. Various tolerances defining convergence criterion were left as default values:

- Convergence tolerance: 1 x 10^{-1}
- Threshold pivot tolerance: 1 x 10^{-4}
- Parameter tolerance: 1 x 10^{-6}
- Objective function tolerance: 1 x 10^{-6}

Initial guesses were varied randomly, and several random initial guesses were tried when fitting each candidate model. Specifically, initial guesses for the $\{\beta_i\}$ and γ values were a random number between 0 and 1, and for the $\{\ln k_i\}$ and $\{\ln K_i\}$ rate and equilibrium constants, initial guesses were a random number between -3 and 4. For the best fit model, it generally did not matter what the initial guess was. For some rejected models, the initial guess did matter, and the model fit corresponding to the highest goodness-of-fit parameter was selected and reported.

Goodness-of-fit statistics were obtained from the Athena Visual-generated model discrimination and criticism report, which reports a variance ratio (which is referred to as the F-ratio in this work) and the sampling probability of greater ratio (which is referred to as alpha in this work). A theoretical discussion is provided in a textbook resource.[75]

A.5.2 Statistical graphs of best-fit model

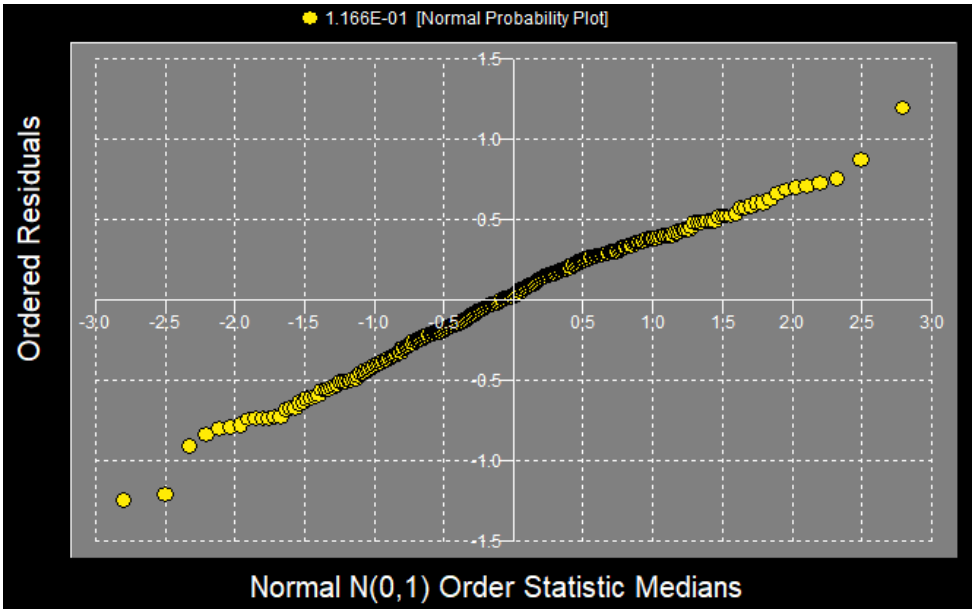

Figure A-A5. Normal probability plot for optimum parameter fitting of the proposed model. Since the plot appears linear, there is a good indication that errors between model and data are normally distributed

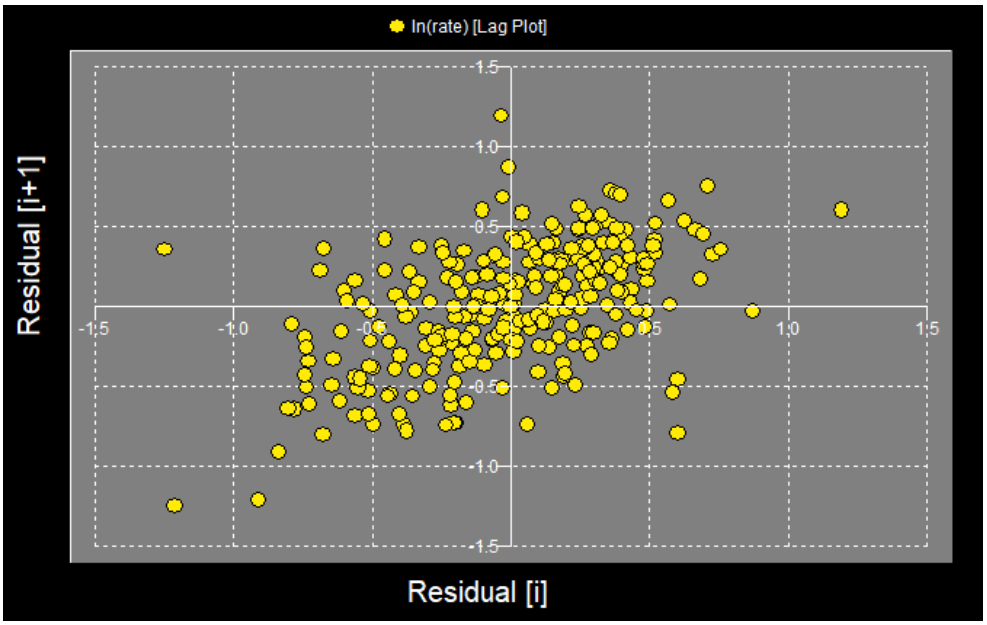

Figure A-A6. Lag plot for the optimum parameter fitting of the proposed model. Since the plot appears random, that is a good indication that there is no correlation or drift within the data

A.6 Supplemental data

A.6.1 Negligible effect of Nafion in the electrode

A small amount of Nafion was added to the electrode to serve as an ion conductive binder. However, Nafion has been implicated to block heterogenized transition metal macrocycle active sites in some electrocatalytic contexts.[164] To address this possibility, we performed control experiments to determine if Nafion had a similar detrimental effect in our system and found a negligible difference (Figure A-A7).

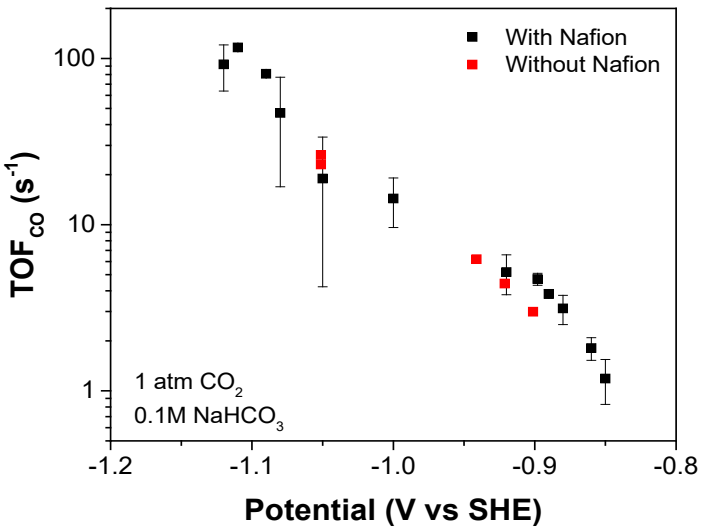

Figure A-A7. Plot of turnover frequency at different applied potentials for electrodes with (black) and without (red) Nafion added to the electrode. Points in red are single measurements. For points in black, error bars represent standard deviation between 2-10 data points.

A.6.2 Invariance of TOF to catalyst loading

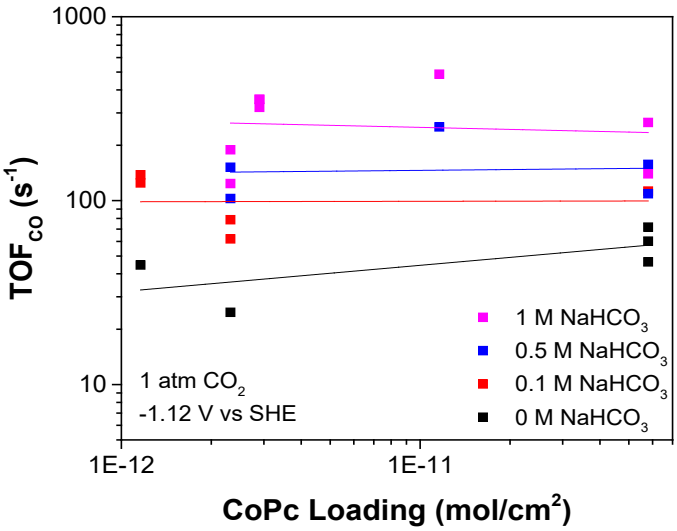

Figure A-A8. Turnover frequency to CO as a function of various catalyst loadings. All points collected at the most reductive potential analyzed in this work, -1.12 V vs SHE, which is the potential that should be most susceptible to transport limitations. Total geometric current density is given by multiplying TOF_{CO} with CoPc loading. Each point represents one experiment, solid lines are linear regressions to help guide the eye.

A.6.3 Hydrogen evolution (HER) trends

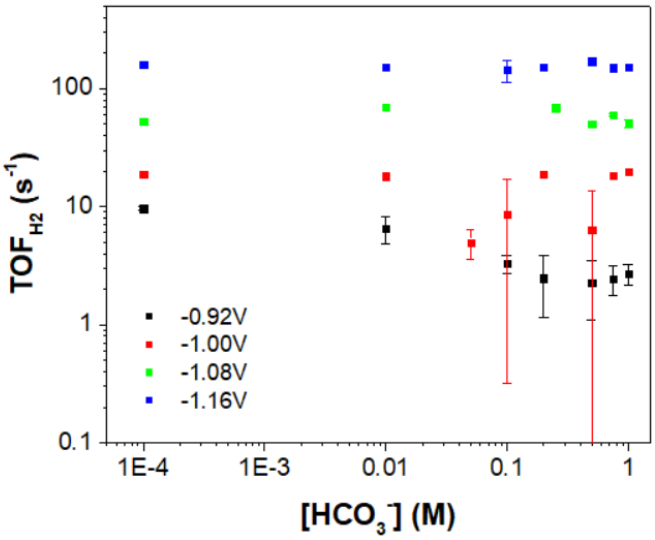

Figure A-A9. Rate data for hydrogen evolution reaction. Points without error bars were repeated in singlicate. Error bars represent standard deviation between 2-5 data points

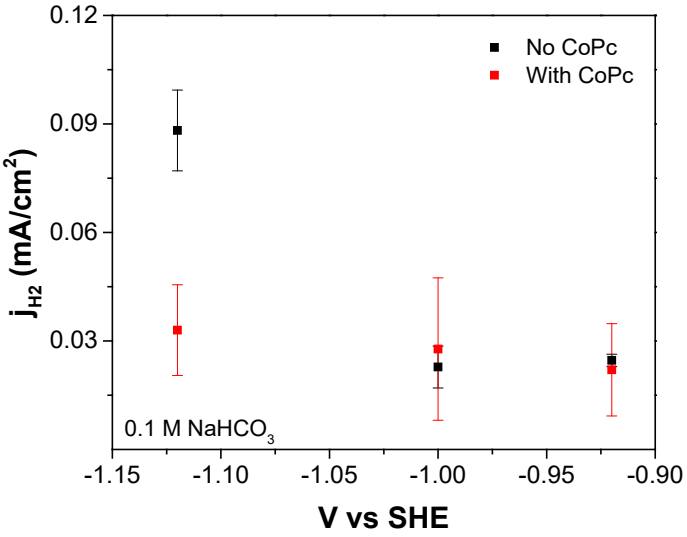

Figure A-A10. Rate data for hydrogen evolution reaction under some representative reaction conditions, using carbon paper with and without CoPc catalyst. Error bars represent standard deviation with n ≥ 2. Although the TOF towards HER is seen to increase with more reductive potentials in Figure A-A9, because the overall catalyst loading was generally lowered at more reductive potentials, the overall current towards HER was roughly constant with potential, as seen in this figure.

A.6.4 Tafel fitting graphs

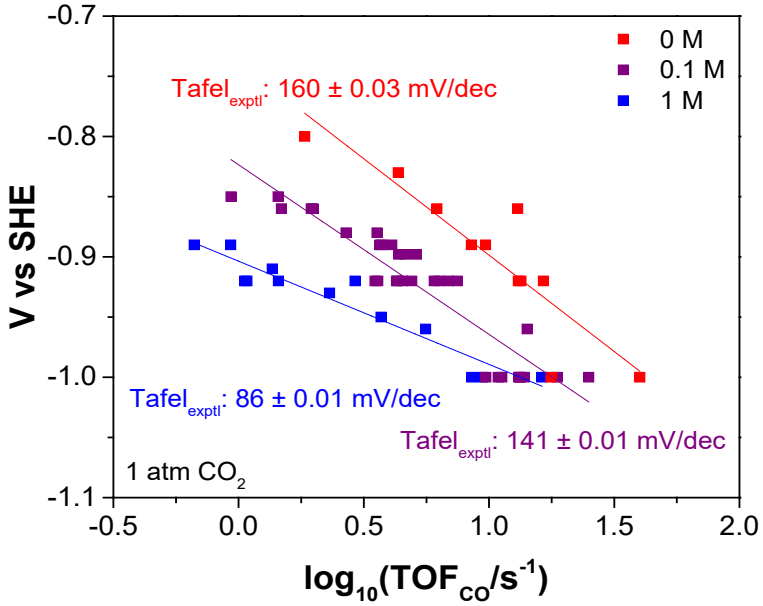

Figure A-A11. All data used to fit experimental Tafel slopes that were reported in Figure 4-1 of the main text. Unlike Figure 4-1 of the main text, all points represent one singlicate experiment; multiple points collected at the same conditions are shown as multiple points on the graph (only points that were not repeated in at least duplicate were shown in Figure 4-1 of the main text, but all points were considered for the fitting in this figure). For all

bicarbonate concentrations, the region less reductive of -1 V vs SHE was considered for the Tafel fit. Lines represent linear regressions of the data.

A.6.5 CO_2 order dependence fitting

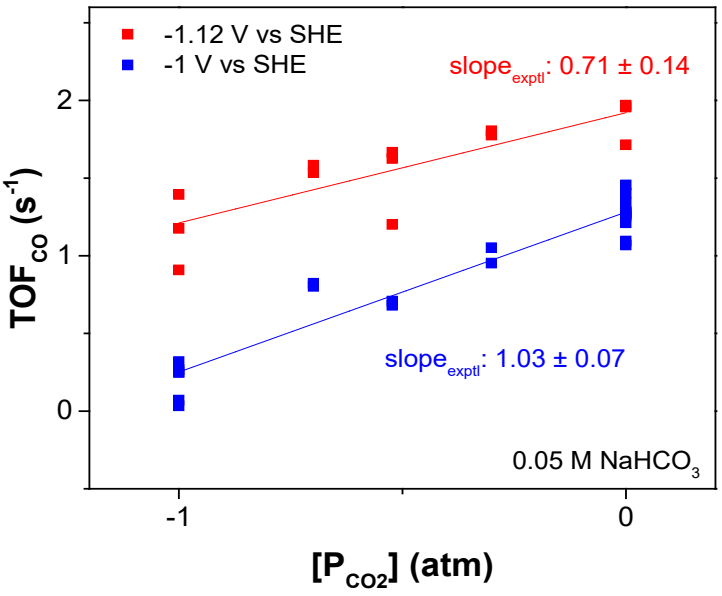

Figure A-A12. All data used to fit experimental CO_2 order dependences that were reported in Figure 2-1 of the main text. Unlike Figure 2-1 of the main text, all points represent one single experiment; multiple points collected at the same conditions are shown as multiple points on the graph. Lines represent linear regressions of the data.

A.6.6 CO2 order dependence at different [$NaHCO_3$]

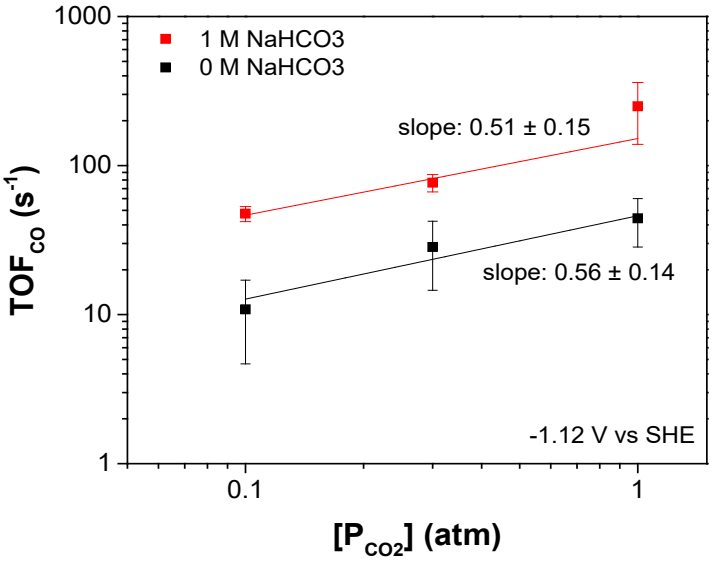

Figure A-A13. CO_2 order dependence at -1.12 V vs SHE, in 1 M $NaHCO_3$ and 1 M $NaClO_4$ (0 M $NaHCO_3$) electrolyte solutions. A deviation from unity is observed in both cases.

A.6.7 Control measurements for excluded hypotheses

Perchlorate order dependence was measured at constant [$NaHCO_3$] of 0.05M and varying [$NaClO_4$] from 0 to 0.95M (thus, the ionic strength was not kept constant). The below data in Figure A-A14 is not corrected for "salting out" because the overhead partial pressure of CO_2 was kept at 1 atm, which means that the activity of dissolved CO_2 was constant in the electrolyte solution.

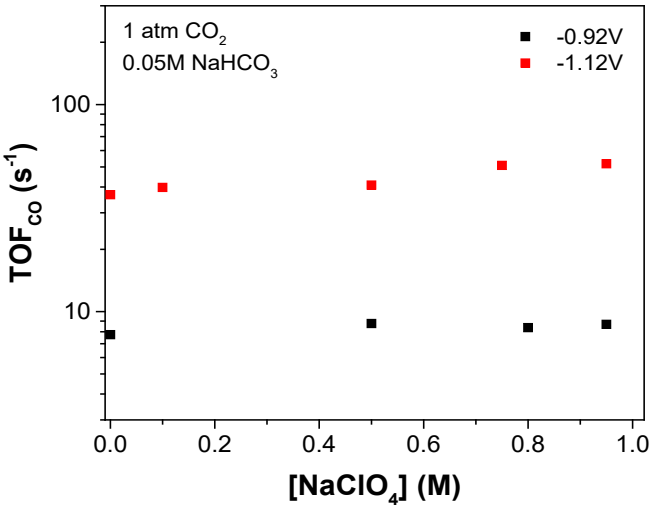

Figure A-A14. Perchlorate order dependence on CoPc. Voltages are vs SHE.

We also considered the possibility that changing the electrolyte composition could cause changes in the junction potential between the leak-free reference and the electrolyte. This hypothesis seemed unlikely due to the different observed bicarbonate order dependence trends at less vs more reductive cathode potentials. We nonetheless tried calibrating the reference electrode against the ferri/ferrocyanide redox couple in the different electrolyte compositions. This was done by running cyclic voltammograms in solutions consisting of 5mM $K_3[Fe(CN)_6]$ dissolved in the appropriate electrolyte composition, using calcined carbon paper as the working electrode and Pt as the counter electrode. As seen in Figure A-A15 and Table A-A8, we did not observe shifts large enough to account for the observed kinetic trends. (A 4mV shift for a reaction that has a Tafel slope of approx. 120 mV/dec represents about 8% error in measurement of TOF.) This data should be interpreted with caution because some white precipitate formed upon dissolution of 5mM $K_3[Fe(CN)_6]$ in the electrolyte solutions. Additionally, the ferri/ferrocyanide redox potential may also change depending on electrolyte composition.[165]

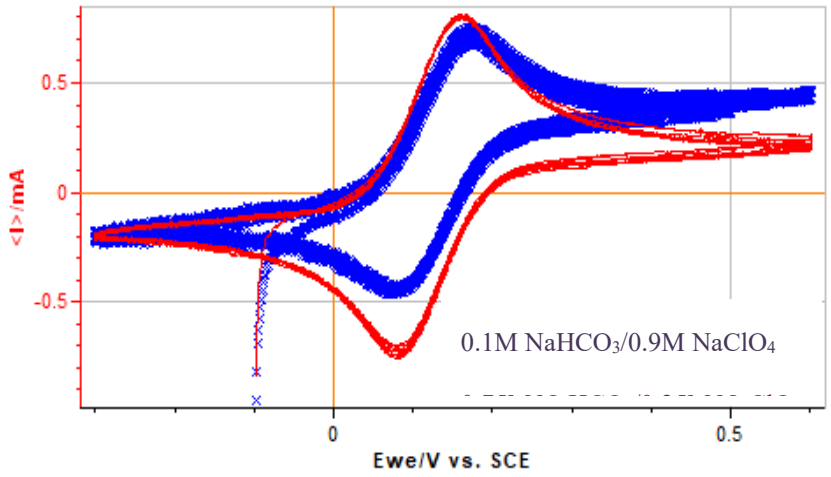

Figure A-A15. Cyclic voltammograms of 5mM $K_3[Fe(CN)_6]$ in different electrolyte compositions. Voltage on the graph is V vs leak-free Ag/AgCl reference.

	0.1M $NaHCO_3$/0.9M $NaClO_4$	**0.75M $NaHCO_3$/0.25M $NaClO_4$**
E_{ox} (V)	0.171	0.161
E_{red} (V)	0.084	0.083
$(E_{ox}+ E_{red})/2$ (V)	0.128	0.122

Table A-A8. Tabulated values of reference electrode shift due to junction potential, determined from cyclic voltammograms

Finally, we also considered the possibility that the observed kinetic trends could be due to a difference in the amount/types of impurities present in the $NaHCO_3$ solution vs the $NaClO_4$ solution. Upon using higher purity sodium carbonate salts (99.999% rather than >99% Na_2CO_3, Sigma Aldrich) and also treating the electrolyte with chelating agent according to previously reported procedures[163], we did not notice any change in the kinetic data (Figure A-A16). We hypothesize that due to the mostly carbonaceous and CO2RR-inert nature of the electrode, trace metal impurities would be less likely to plate onto catalyst site and affect activity.

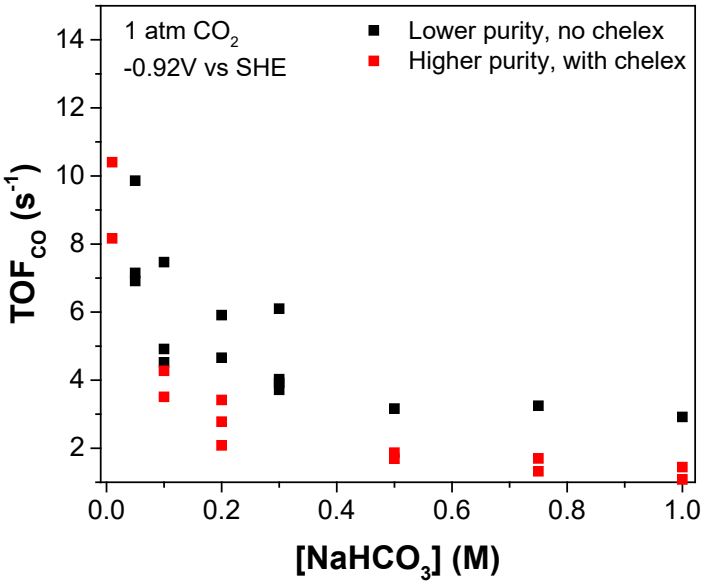

Figure A-A16. Effect of using purer electrolytes in CO2RR on CoPc. The observed bicarbonate order dependence trend remains. Data shown was collected months apart.

A.6.8 Addition of exogenous phosphate buffer

We also performed an experiment in which phosphate buffer (0.5 M, pH 7: 0.289 M Na_2HPO_4 + 0.211 M NaH_2PO_4) was added to the system while maintaining constant total ionic strength of 1 M (Figure A-A17). Because $H_2PO_4^-$ has a pKa of 7.2 whereas HCO_3^- has a pKa of 10.33, we expect that when the two ions are present at similar concentrations, that $H_2PO_4^-$ should be the preferential proton donor. Therefore, the attenuated positive bicarbonate order dependence in the presence of phosphate buffer at more reductive potentials adds further evidence to support our mechanistic hypothesis.

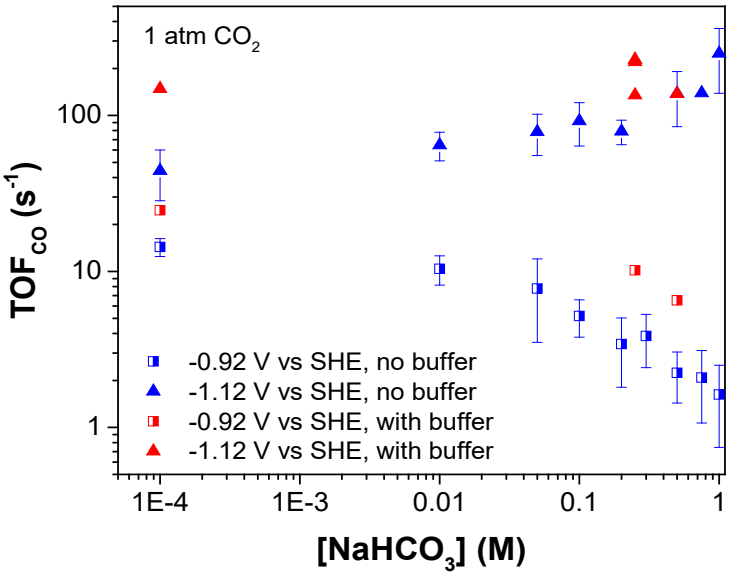

Figure A-A17. Effect of adding phosphate buffer to the system. For points in blue, no phosphate buffer was added to the system, and the total salt concentration is 1 M via the addition of balancing $NaClO_4$. Blue points and error bars represent means and standard deviations for 2-10 points. For points in red, in addition to adding the amount of $NaHCO_3$ specified by the x-axis, 0.5 M pH 7 phosphate buffer was added to the electrolyte. The total salt concentration was kept at 1 M via addition of balancing $NaClO_4$. Each red point represents a single experiment.

A.6.9 Cursory bicarbonate order dependence on CoTPP

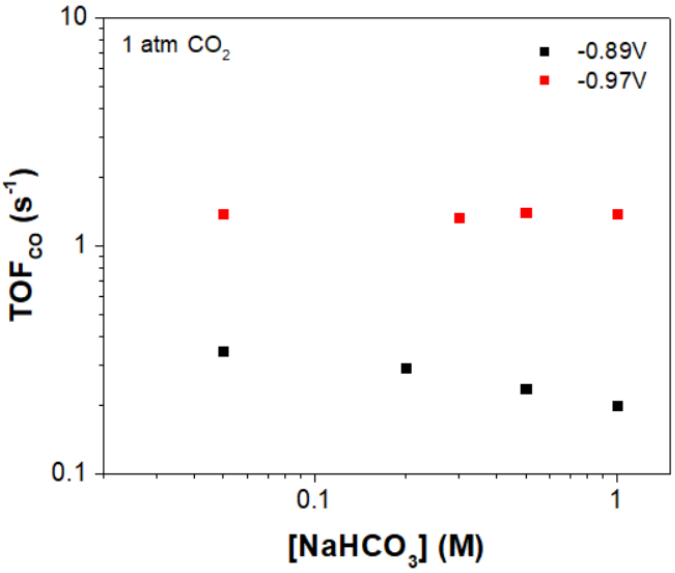

Figure A-A18. Bicarbonate order dependencies on cobalt tetraphenyl porphyrin (CoTPP) at more and less reductive potentials (potentials are vs SHE). Points indicate singlicate experiments. A slight negative order dependence is observed at less reductive potentials.

A.7 Supplemental model visualizations

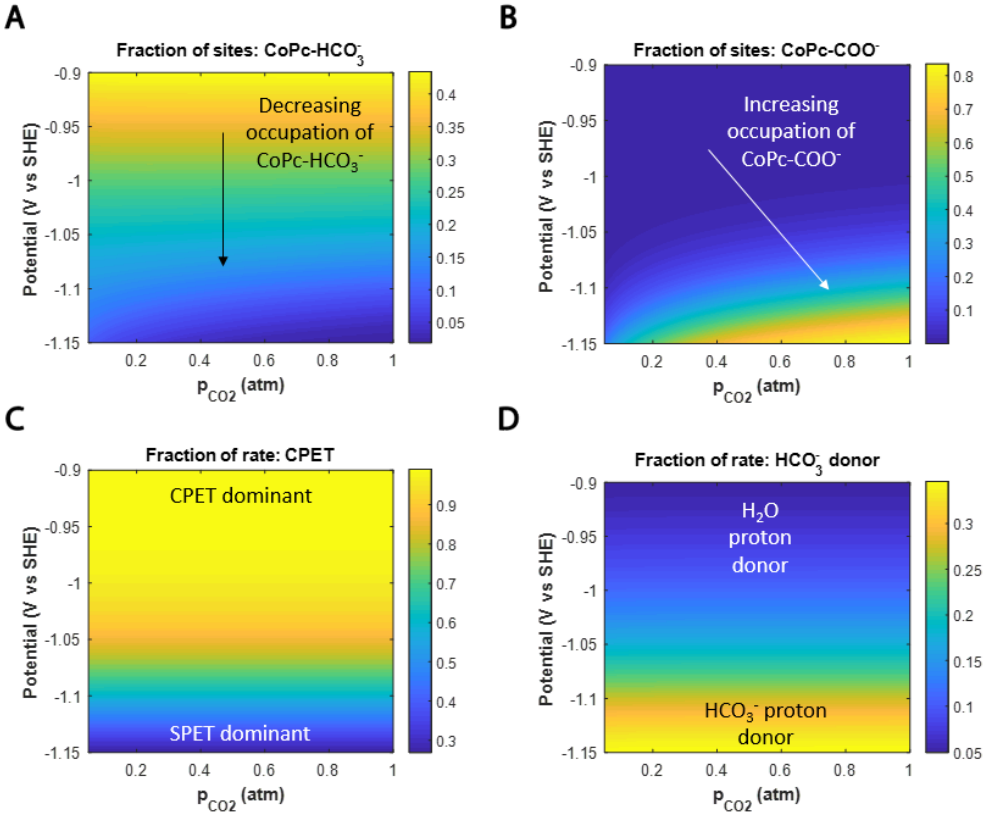

Figure A-A19. Relevant kinetic limits, allowing voltage and P_{CO2} to vary and holding [$NaHCO_3$] at 0.05M

APPENDIX B: ADDITIONAL CONSIDERATIONS AUTOMATED ELECTROCHEMICAL KINETIC ANALYSIS

B.1 Materials and methods

B.1.1 Parts list

A list of key commercially available parts:

- Tinkerforge parts:
  - Master Brick (x1)
  - Silent Stepper Brick (x 1)
  - Silent Stepper Bricklet (x 2)
  - RS232 Bricklet 2.0 (x 2)
  - Industrial Quad Relay Bricklet 2.0 (x 4)
  - Bricklet Cables, assorted lengths
- [power supply]
- Actuators:
  - Fuyu FSL30 Mini Linear Stage Actuator (150 mm stroke)
  - Fuyu FSL40 Linear Guide (400 mm stroke)
- Pumps:
  - Kamoer low flow peristaltic pump 12V DC 3mm ID x 5mm OD (x2)
  - Kamoer small peristaltic pump stepper motor 24V Adjustable Speed KPAS-100, 110ml/min, 3.2mm ID ×6.4mm OD, 3 rotors (x 1)
- Misumi aluminum extrusions
- Soft Viton o-rings (McMaster-Carr 1284N12 & 1284N116)

The cell body and cell pans, as well as mounts/housing for the cell body and cell pans, were custom-made parts. Blown up CAD drawings of these components are illustrated below, and CAD files are available upon request.

B.1.2 Control software details

Control over the potentiostat was achieved using the PyExpLabSys package that utilizes the EClab Development Package. All code was implemented in 32-bit Python 3.7. Databasing was performed with PostgreSQL.

B.1.3 Additional experimental details

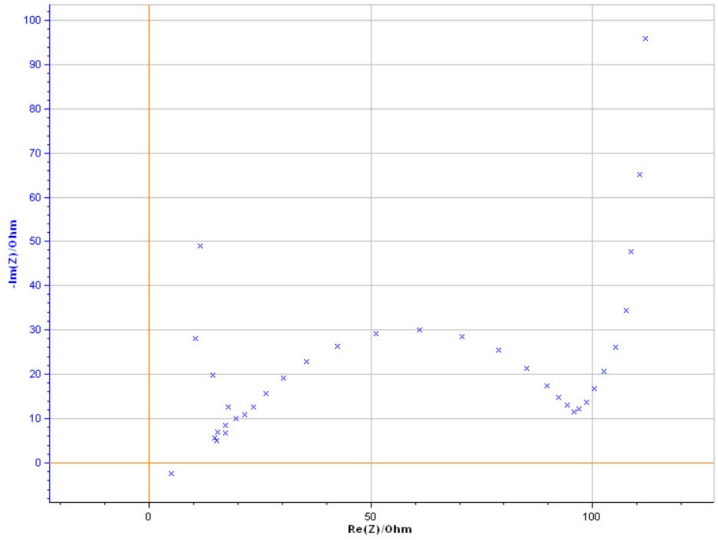

Figure 7-1. PEIS spectrum of cell, showing a solution resistance of approximately 15 ohms.

B.2 Supplemental data and discussion

B.2.1 Geometric effects

With asymmetry between working and counter electrode, there can arise inhomogeneity in current flux at different locations on the working electrode. These inhomogeneities are more problematic for highly resistive solutions, and for the 1 M ionic strength solutions used here, this is not expected to be an issue.

B.2.2 Effects related to flow configuration and mass transport

Despite the fact that the CO_2RR currents measured here are orders of magnitude below the predicted transport-limited current density (for a planar electrode), control tests in a hand-assembled 3-compartment cell show that the gas flow configuration does influence measured rates. This may possibly be related to the porosity of the electrode, and the fact that approximated transport limitations for a planar electrode may not be fully reflective of the transport phenomena within porous carbon electrodes.

B.2.3 Faradaic efficiency closure

Faradaic efficiency closure for the two expected products, hydrogen and carbon monoxide gas, were usually between 50-90%, which is low compared to the expected 100%. This is likely to

to background ORR, possibly exacerbated by OER at the counter electrode of the 1 compartment cell.

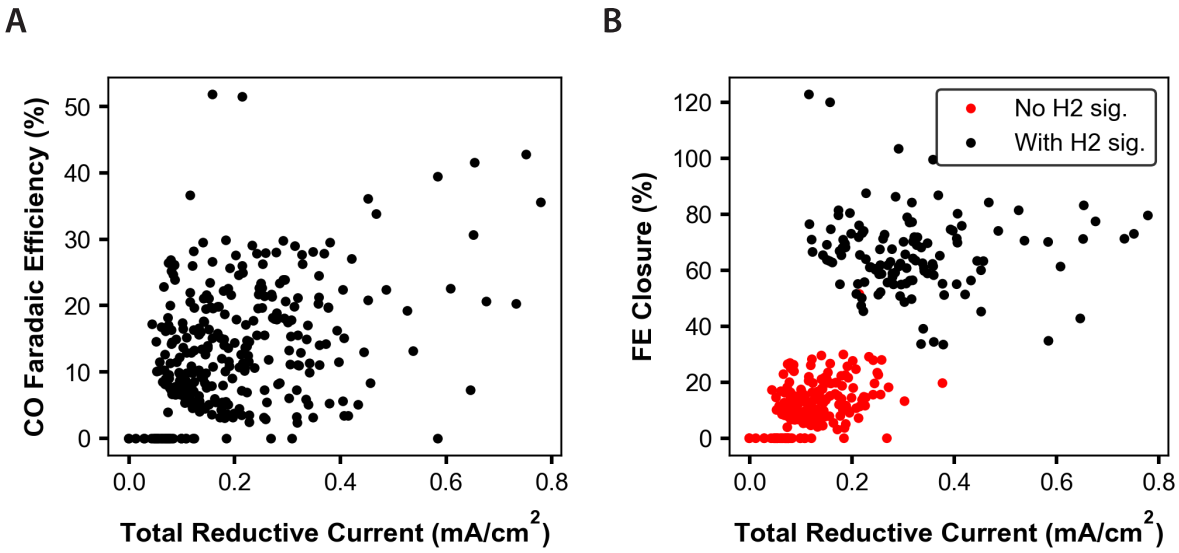

Figure 7-2. Faradaic efficiency (FE) of data collected with automated setup. **A**, FE towards CO, plotted as a function of total current. **B**, Total FE closure ($FE_{CO} + FE_{H2}$), plotted as a function of total current. Points for which the H_2 signal was below the GC TCD detection limit are shown in red.

APPENDIX C: ADDITIONAL CONSIDERATIONS FOR ELECTRIFIED C–C BOND FORMATION

C.1 Materials and Methods

C.1.1 Materials List

All chemicals and materials were used as received unless otherwise specified.

Catalyst materials

- Cerium(III) nitrate hexahydrate (Beantown Chemical, 128635)
- Rhodium (III) acetylacetylonate (97%, Sigma Aldrich 282774)
- Toray 120 carbon paper (Fuel Cell store, 5% wetness proofing)
- Nafion 117 solution (5% in alcohols and water, Sigma Aldrich 70160)
- Carbon black (Vulcan XC 72, Fuel Cell Store)

Reactivity Studies

- Isopropanol (>99.5% Sigma Aldrich 190764)
- Tetrabutylammonium trifluoromethanesulfonate (Sigma Aldrich 86888)
- Trifluoromethanesulfonic acid (Sigma Aldrich 347817)
- Styrene (Sigma Aldrich, S4972)
- Carbon monoxide gas (Airgas CM R300)
- Hydrogen gas (Airgas HY UHP35)
- 1,3,5 trimethoxybenzene (>99%, Sigma Aldrich 138827)
- Neosepta AHA membrane (Ameridia Innovative Solutions)
- Aluminum foil (Reynold's Wrap)

C.1.2 Supplemental figures for methods

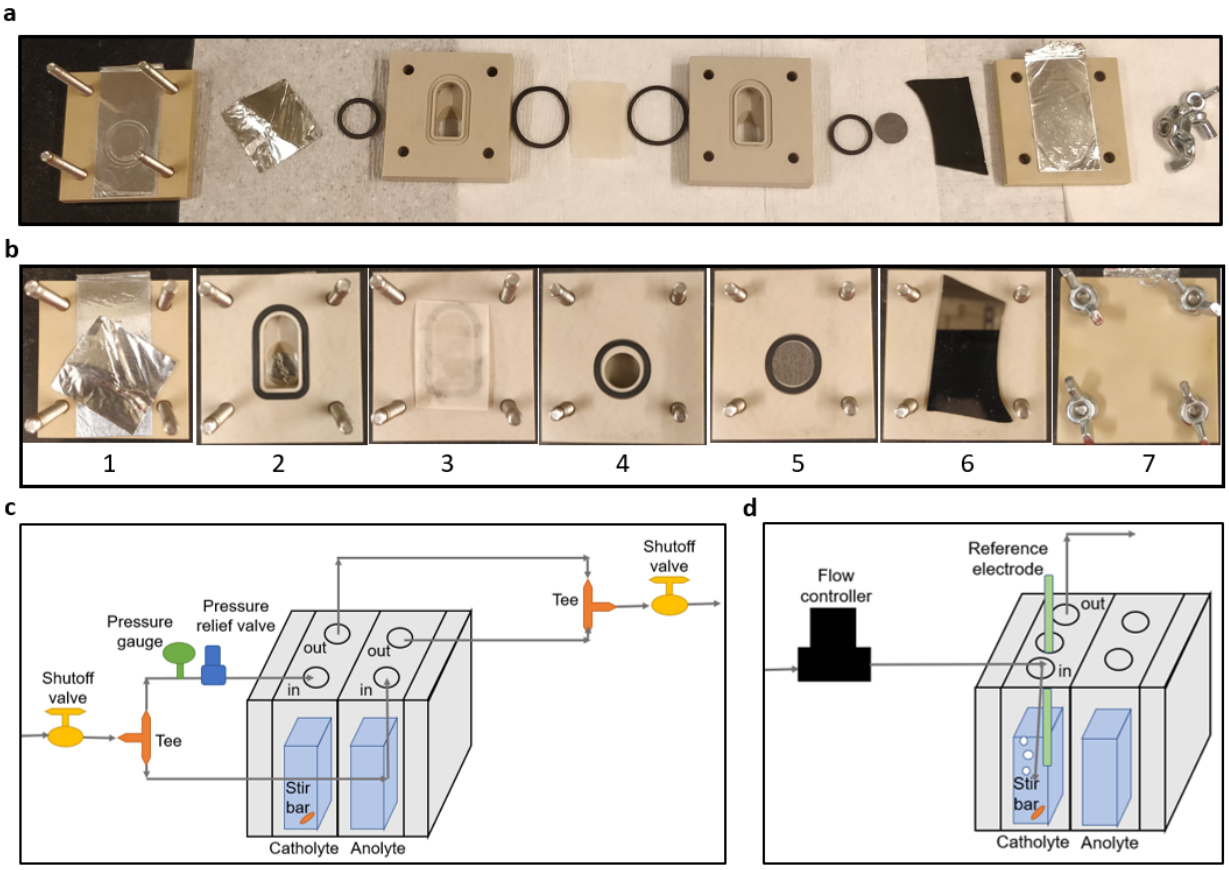

Figure A-C1. Assembly and set up of the electrochemical cell. **a**, Exploded-view picture of all cell parts. **b**, Sequential birds-eye view of the cell as it is assembled. **c**, Gas configuration for elevated pressure experiments, in which there is no gas flow, just a static pressurized headspace. **d**, gas configuration for ambient pressure experiments, in which gas is bubbled through the electrolyte.

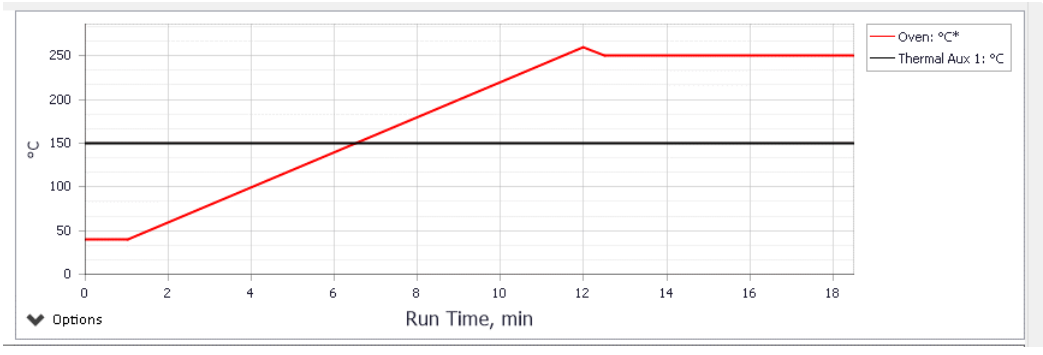

Figure A-C2. GC temperature ramp method.

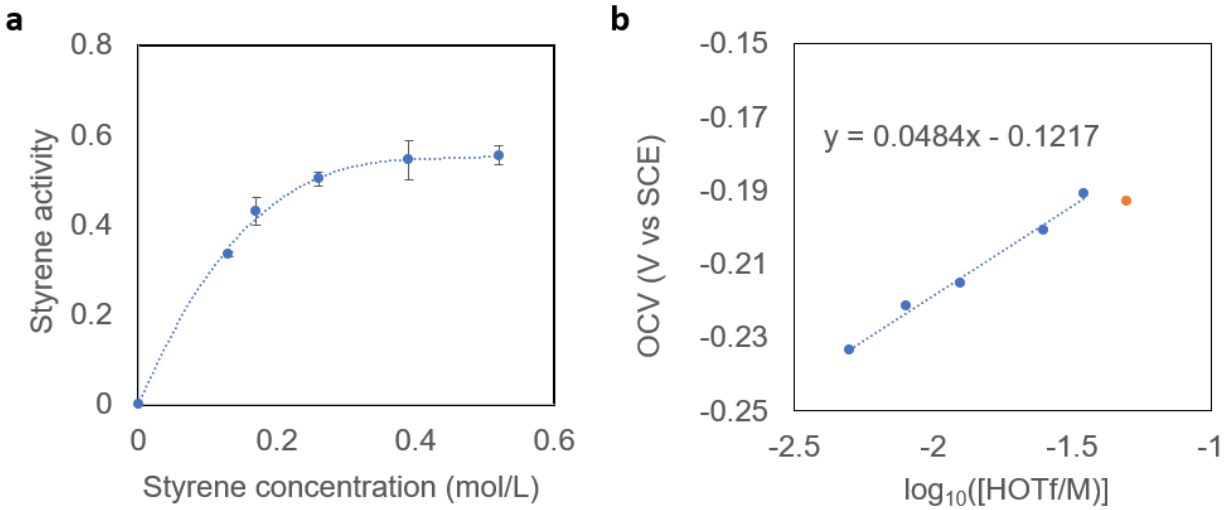

Figure A-C3. Characterization of liquid-phase species activity in electrolytes used for order dependence studies. **a**, Experimentally measured styrene activity as a function of styrene concentration. All points were collected in triplicate and error bars indicate population standard deviation. **b**, experimentally measured reversible hydrogen electrode (RHE) potentials under 1 bar of H_2 gas flow for electrolyte with different concentrations of HOTf. In all cases, electrolyte consisted of 50% v/v H_2O/IPA with 0.1 M TBAOTf, 0.52 M styrene, and 25mM HOTf (unless explicitly labeled otherwise).

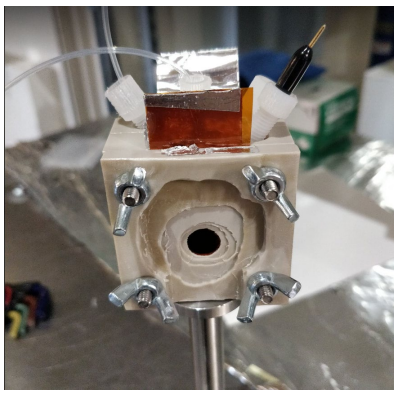

Figure A-C4. *Operando* XAS cell. Depicted is the Kapton window, which is pressed right against the back of the working electrode in an electrochemical cell that is otherwise configured identically to a typical electrolysis cell.

C.2 Supplemental discussion

C.2.1 Temperature dependence of electro- and thermo- HFN

At elevated temperatures of 80 °C, we observed that the Rh@CeO_2 catalyst was fairly active for thermo-HFN, with a TOF of around 40 hr^{-1} in representative electrolyte conditions, at 10 bar of 1:1 CO:H_2 (Figure A-C5c). We found activity for electro-HFN at 80 °C in comparable

solvent conditions to be quite poor, with a maximum observed TOF of less than 0.1 hr^{-1} (Figure A-C5d).

The observations at 80 ºC are in contrast with what we observed at room temperature, where the thermo-HFN TOF was around 0.01 hr^{-1} (Figure A-C6a) and the electro-HFN TOF was around 0.7 hr^{-1} (Figure 4-1c).

The increase in thermo-HFN TOF at higher temperatures intuitively makes sense, and corresponds to a positive enthalpy of reaction. The apparent decrease in electro-HFN TOF at higher temperatures likely does not hold any significant fundamental meaning. We hypothesize that the apparent decrease in rate is simply due to a greater degree of side reactivity and product degradation at elevated temperatures. From a fundamental perspective, likely that the electro-HFN mechanism is simply less sensitive to temperature than the thermo-HFN mechanism (lower apparent activation enthalpy), which allows for reasonable electro-HFN reactivity to be retained even at ambient temperature.

C.2.2 No evidence for non-Faradaic promotion

We tested for evidence that voltage could non-Faradaically promote of thermo-HFN, since this could be an alternative explanation to our kinetic data that suggested a non-mediated mechanism. It was not possible to directly test for non-Faradaic promotion of thermo-HFN at room temperature because observed electro-HFN rates exceeded those of thermo-HFN. Therefore, upon application of voltage, it would not be possible to examine only the contribution of reactivity that could be unambiguously attributed to thermo-HFN. However, at elevated temperatures, we observed that thermo-HFN was much faster than electro-HFN. Thus, at 80 ºC, we could run a thermo-HFN reaction with applied potential, and rigorously attribute most or all of the observed reactivity to thermo-HFN (in these conditions, the amount of charge passed was much lower than the amount of product observed). We note that of course the mechanisms at 25 and 80 degrees C may not be the same.

Figure A-C8b shows that under thermo-HFN conditions, the measured thermo-HFN TOF does change in response to applied potential (black points). However, if the catalyst is simply dispersed in the solution, rather than being attached to the electrode (Figure A-C8a), the measured thermo-HFN rate also responds to applied potential, and with a very similar trend (red points). Thus, the changes in thermo-HFN reaction rates that we observe in Figure A-C8b are likely not due to non-Faradaic promotion; rather, they likely arise from bulk changes in electrolyte composition that arise due to Faradaic processes at the electrode surfaces. Thus, in this experiment, we do not see compelling evidence that voltage non-Faradaically promotes thermo-HFN.

C.2.3 Analysis of maximum local H_2 accumulation

We will analyze the case in which soluble H_2 is being generated at the cathode at a flux of -0.4 mA/cm^2, where this current density is given with respect to the planar geometric area of the electrode. The question here is whether the local concentration of H_2 under this current density

can exceed the bulk concentration of H_2 expected under 10 bars of H_2 headspace. This analysis will help us understand whether electro-HFN rates reported in Figure 4-1c and thermo-HFN rates reported in Figure A-C6a can be consistent with an indirect electro-HFN mechanism. In the end, we will conclude that an indirect mechanism via local H_2 accumulation is not feasible.

We will analyze the transport problem as a constant flux boundary condition applied to a mass transport boundary layer. Since the flux across this boundary layer must be constant and equal to the boundary condition, we can write:

$$C_{bulk} - C_{interface} = \frac{nF\delta i}{D}$$

Where n is the number of electrons transferred in the reaction, F is Faraday's constant, δ is the hydrodynamic boundary layer thickness, i is the applied current, D is the diffusivity of the species, and C_{bulk} and $C_{interface}$ are the bulk and interfacial concentrations of the species.

If we assume the diffusion coefficient for H_2 is 5E-5 cm^2/s (its value in pure water at 25 ºC), and that the boundary layer thickness is about 100 um, we get:

$$C_{bulk} - C_{interface} = \frac{(2)*(96485)*(1E-4\ cm)*(0.4\ \frac{mA}{cm^2})}{5E-5\ \frac{cm^2}{s}} = 0.1\ \text{mM}$$

The solubility of H_2 gas in pure water at 25 ºC and 1 bar is 0.00016 g H_2/100 g H_2O,[166] or 0.8 mM; at 10 bar H_2, assuming linear scaling that is typical of gas-liquid equilibrium, the solubility of H_2 should be around 8 mM, more than an order of magnitude higher than the maximum H_2 concentration that could be generated from a -0.4 mA/cm^2 reaction flux.

C.2.4 Analysis of transport limited current density

The equation for transport limited current density to a planar surface is given by:

$$i_{lim} = nF\frac{D_A C_A}{\delta}$$

Where n is the number of electrons transferred in the reaction, F is Faraday's constant, D_A and C_A are the diffusivity and bulk concentrations of A, the most limiting reactant in the system, and δ is the hydrodynamic boundary layer thickness.

In our system, the possible limiting reactants are styrene (0.52 M), proton (0.025 M), and CO (0.009 M in pure IPA[167] and 0.0009 in pure water). Taking the lowest concentration, which is CO, we will assume the solubility of pure water (which should give a lower limit). We can also assume a diffusion coefficient for CO of about 1E-5, which is a conservative estimate for gas in liquid. Finally, we can assume a boundary layer thickness of about 100 um, which has been shown in similar cells.[45] Taken together, we get:

$$i_{lim} = 2 * 96485\ \frac{(1E-5\frac{cm^2}{s})(9E-4\frac{mol}{L})(\frac{1L}{1000\ cm^3})}{1E-4\ cm} = 17\ \text{mA/cm}^2$$

In the kinetic data reported in main text Figure 4-3, total currents are below -0.5 mA/cm^2, which is only 3% of the transport limited current density, and partial current towards electro-HFN,

the only CO-consuming reaction, is less than 6 uA/cm^2, which is less than 1% of the transport limited current density.

C.2.5 Rh valency and coordination during proposed mechanism

Precedent from both homogeneous and heterogeneous thermo-HFN literature suggest that intermediates **1**, **2**, **3**, and **4** from Figure 4-4 of the main text are at Rh(I), and that intermediate **7** is at Rh(III). However, in our proposed mechanism, we invoke that the most abundant reactive intermediate within the proposed cycle is mostly **1**. Thus, there is an apparent contradiction with our reported XANES data (Figures 2a and 2b from the main text), which shows that on average, the surface Rh species under reaction conditions is Rh(III). We suggest two mechanistic possibilities that may resolve this apparent contradiction. We emphasize that the below discussions simply represent mechanistic speculations that can reconcile the reported experimental observations with chemical intuition and do not represent mechanistic claims of this work.

First, it may be the case that the most abundant surface Rh species is Rh(III), and that only a small fraction of Rh sites are participating in electro-HFN catalysis,. Of the small fraction of sites participating in catalysis, the most abundant reactive intermediate within the catalytic cycle may still be Rh(I), which would be consistent with previous reported thermo-HFN mechanisms, the proposed mechanism in Figure 4-4, and the operando XANES data. In this case, chemical intuition that Rh(I) typically prefers coordination of 4 ligands would suggest that intermediates **1**-**4** are coordinated to 3 lattice oxygens that function as L-type ligands (i.e., OR_2). Intermediate **5** could also be Rh(I) coordinated to 3 lattice oxygens, and perhaps intermediate **6** could be formulated as Rh(III) coordinated to 4 lattice oxygens, one of which functions as an X-type ligand (i.e., OR^-).

Alternatively, it may be the case that all of the reactive intermediates proposed in the cycle are actually formulated as Rh(III) sites, where intermediates **1**-**5** would then be coordinated to five lattice oxygens (because Rh(III) tends to prefer 6 ligands), 3 of which function as L-type ligands and 2 of which function as X-type ligands. Then, perhaps intermediate **6** can be formulated also as Rh(III), which would require one of the X-type oxygen ligands to decoordinate.

In either case, we invoke that **6** is likely a Rh(III) intermediate, and that to get from **4** to **5** to **6**, regardless of whether **4** is formulated as a Rh(I) or Rh(III), we require dynamic coordination (in the case of **4** being Rh(I)) or decoordination (in the case of **4** being Rh(III)) of an X-type oxygen ligand to avoid even numbered Rh oxidation states (i.e., Rh(II) or Rh(IV) that are more unlikely to exist).

Finally, we note that this picture of dynamic coordination and decoordination of lattice oxygen ligands may be consistent with our experimental observation that triflate-containing salts enhance electro-HFN activity. Triflate is known to be a labile ligand,[133] and it may be the case that its presence helps increase the lability of Rh-O bonds. Increase in Rh-O lability may generally increase the availability of open coordination sites at Rh for catalysis, as well as

facilitate the dynamic oxygen coordination that may also be occurring during electro-HFN catalysis.

C.2.6 Mechanistic interpretations from kinetic rate data

We will present a rate equation for the proposed mechanism illustrated in Figure 4-4 of the main text and provide more detail about how it is qualitatively consistent with the rate data presented in Figure 4-3 of the main text.

Each step will be described with either an equilibrium constant (K) or forward rate constant (k). Let us assume that (1) is the MARI, that steps between (1) to (4) are equilibrated, that the ET and PT steps are rate limiting and irreversible, and that the pseudo steady state hypothesis can be applied to (4). Then, solving for the rate equation will yield:

$$rate = \frac{k_{ET}K_{12}K_{23}K_{34}[CO][sty]exp\left(-{}^{\alpha F\phi}/_{RT}\right)}{1 + K_{12}[sty] + K_{12}K_{23}[sty] + K_{12}K_{23}K_{34}[CO][sty] + K_{12}K_{23}K_{34}[CO][sty]\frac{k_{ET}exp\left(-{}^{\alpha F\phi}/_{RT}\right)}{k_{PT}[H^+]}}$$

We can qualitatively observe that at high overpotentials, the last term in the denominator will dominate, leading to a reduced voltage dependence and increased positive proton dependence. At low overpotentials and low CO and styrene surface coverages, the first term (ie, just 1) in the denominator will dominate, and the reaction will have a strong dependence on electron with no dependence on proton.

C.2.7 Overpotentials and energy efficiency of electro-HFN

We will first require a calculation of the expected equilibrium potential for the electro-HFN half reaction. For this, let us consider a representative, gas-phase thermochemical hydroformylation reaction, for which all of the gas-phase thermochemistry data is readily available:[168]

Ethylene + CO + H_2 → Propionaldehyde $\Delta G^{o}_{\mathrm{tHFN}}$

Where the standard gibbs free energy of reaction is given by $\Delta G^{o}_{\mathrm{tHFN}}$. This reaction can be written as two electrochemical half-reactions, the electro-HFN half reaction and the hydrogen oxidation (HOR) half reaction:

Ethylene + CO + $2H^+ + 2e^-$ → Propionaldehyde E^{o}_{eHFN}

H_2 → $2H^+ + 2e^-$ $E^{o}_{\mathrm{HOR}} \overset{\mathrm{def}}{=} 0\ V\ vs\ SHE$

Where each half reaction is associated with a standard equilibrium potential. For HOR, the standard equilibrium potential is, by definition, the standard hydrogen electrode (SHE). The relationship between all of these quantities is given by the equation:

$$\Delta G = -nFE_{cell}$$

Where in this case, we have:

$$\Delta G^{\circ}_{\mathrm{tHFN}} = -nF * (E^{\circ}_{\mathrm{HOR}} - E^{\circ}_{\mathrm{eHFN}})$$

$$\Delta G^{\circ}_{\mathrm{tHFN}} = -(2\ \frac{mol\ e}{mol\ rxn}) * (96485\ \frac{C}{mol\ e}) * (-E^{\circ}_{\mathrm{eHFN,vs\ SHE}})$$

Calculating the Gibbs free energy of reaction from gas-phase thermochemical data gives:

$$\Delta G^{\circ}_{\mathrm{tHFN}} = -58.44\ kJ/mol$$

And solving for the standard equilibrium potential of electro-HFN gives:

$$E^{\circ}_{\mathrm{eHFN,vs\ SHE}} = +0.303\ V\ vs\ SHE$$

Since electro-HFN has an equal number of protons and electrons, the pH dependence of the actual equilibrium potential under different pH conditions is given by:

$$E_{\mathrm{eHFN}} = E^{\circ}_{\mathrm{eHFN}} - 0.059 * pH = (+0.303\ V - 0.059 * \mathrm{pH})\ \mathrm{V\ vs\ SHE}$$

This value represents the equilibrium potential for electro-HFN (even within the liquid phase electrolyte, due to gas-liquid equilibrium) of ethylene under 1 atm ethylene and 1 atm of CO. We will use this as an approximation for the thermodynamics of styrene electro-HFN as well.

Under typical operating, conditions, we add 25 mM of HOTf as explicit acid. To get a rough estimate of equilibrium potential, we will make a coarse assumption that proton activity within the electrolyte reflects acid concentration. Thus, we get:

$$E_{\mathrm{eHFN}} = \left(+0.303V - 0.059 * -\log_{10}(0.025)\right) = +0.21\ \mathrm{V\ vs\ SHE} = -0.04\ \mathrm{V\ vs\ SCE}$$

With respect to this analysis, we provide several points of discussion:

First, the positive standard equilibrium potential of electro-HFN with respect to SHE means that electro-HFN can be thermodynamically feasible in conditions where hydrogen evolution (HER) is not. Thus, direct electro-HFN reactions could, in principle, save energy by bypassing H_2 as an intermediate. Specifically, a direct electro-HFN reaction using water as the H atom source would thermodynamically require less cell potential than an alternative process that uses water splitting to generate H_2 and then feeds the H_2 gas to a thermo-HFN reaction.

Second, for experiments performed potentiostatically at 1 bar CO, our typical operating conditions in this work are around -1.05 to -1.45 V vs SCE, which reflect about 1 to 1.5 volts of overpotential with respect to the thermodynamics of electro-HFN, and 0.7 to 1.2 volts of overpotential with respect to the thermodynamics of hydrogen evolution. Thus, further optimization of this chemistry will be required to lower these overpotentials, and will be the subject of future work.

C.3 Extended Data

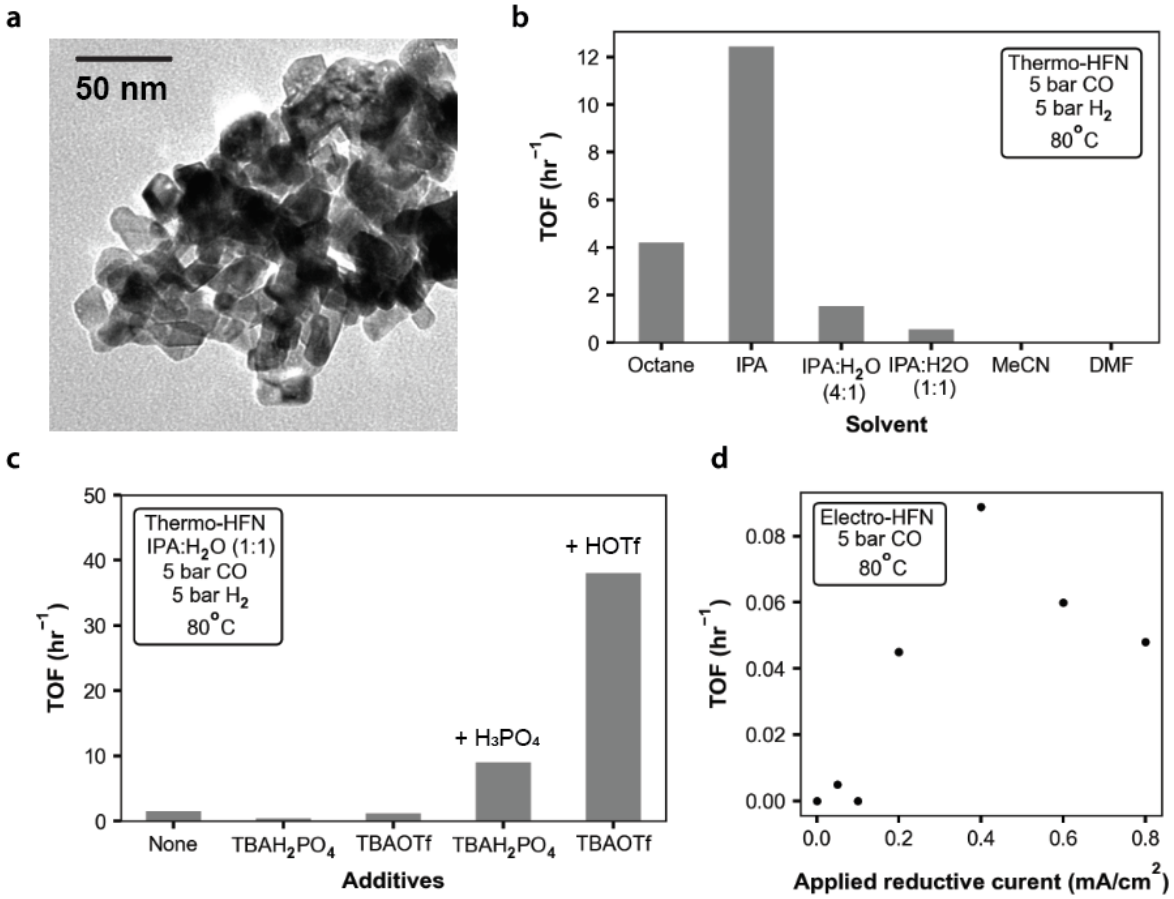

Figure A-C5. Catalyst and reaction characterization during sequential electrification of hydroformylation catalysis. **a**, TEM image of as-synthesized Rh-impregnated CeO_2 (Rh@CeO_2) particles. Individual CeO_2 nanoparticle sizes appear to be ~20 nm. **b**, solvent dependence of thermo-HFN catalyzed by powder Rh@CeO_2 catalysts. **c**, dependence of thermo-HFN rates on salt and acid additives in a 50% v/v IPA and H_2O mixture. **d**, electro-HFN data rates at Rh@CeO_2 catalysts deposited on carbon paper during galvanostatic experiments. All rates are of styrene hydroformylation to both 2-phenylpropanal and 3-phenylpropanal. All thermo-HFN experiments performed at 80 °C, 5 bar CO, 5 bar H_2, and 0.2 M styrene. Electro-HFN experiments were performed at 80 °C, 5 bar CO, 80% v/v IPA with 20% v/v H2O, 0.1 M TBAOTf, 25 mM HOTf, and 2 M styrene.

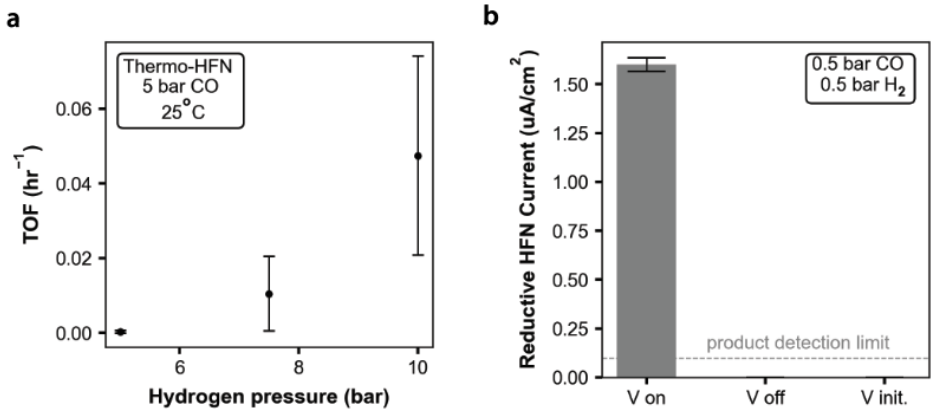

Figure A-C6. Control experiments to examine a possible indirect electro-HFN mechanism. **a**, thermo-HFN rates as a function of hydrogen pressure, at 5 bar CO, in conditions otherwise identical to "default" electro-HFN conditions. **b**, control tests showing amounts of product detected with and without application of voltage, in the explicit presence of H_2 gas. V on indicates constant application of -1.45 V vs SCE for the entire duration of the experiment, V off indicates no voltage applied, and V init indicates -1.45 V vs SCE was applied for only the first 5 minutes of a 2 hr experiment. All data collected at 25 °C, 0.52 M styrene, and 25 mM HOTf, in a 50% v/v IPA/H_2O mixture. Error bars represent standard deviation with n ≥ 3.

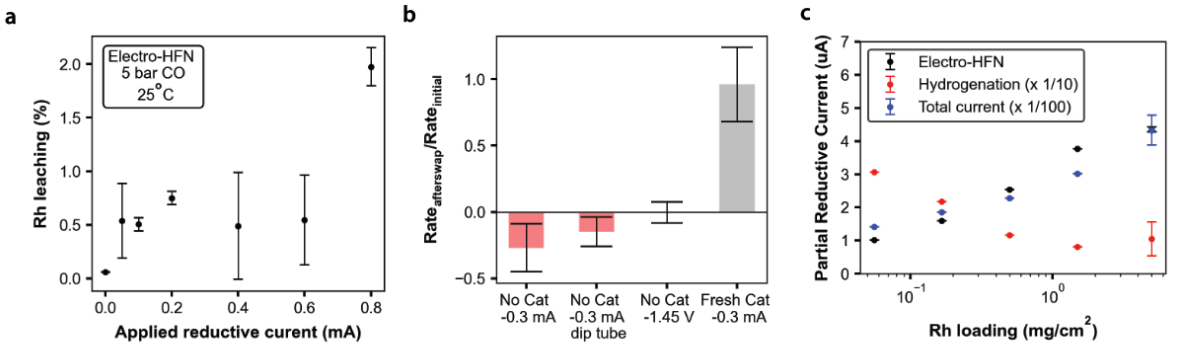

d

Condition	Electro-HFN (uA)	Hydrogenation (uA)	Total Current (mA)
Bare carbon paper (CP)	0	0	-0.07
CP + nafion	0	0	-0.07
CP + nafion + carbon black (CB)	0	-50	-0.15
CP + nafion + CB + CeO_2	0	-40	-0.30

Figure A-C7. Control experiments examining the nature of catalysts sites for electro-HFN. **a**, Amount of solubilized Rh species detected in the electrolyte after electrolysis, quantified via ICP-MS, expressed as a percentage of the total amount of Rh initially deposited on the electrode. These data were collected at 5 bar CO, 2 M styrene, and 80% v/v IPA with 20% v/v H_2O, at conditions otherwise identical to "default" conditions. **b**, heterogeneity test data showing relative rate after a catalyst-coated electrode was swapped with either carbon paper (denoted as "No Cat") or fresh catalyst (denoted as "Fresh Cat"). This test was done under galvanostatic conditions at -0.3 mA and 5 bar CO (bars 1, 2, and 4), or under potentiostatic conditions at -1.45 V vs SCE with 1 bar CO (bar 3). The "dip tube" label indicates that during the electrode swap, electrolyte was removed from the cell while potential was still being applied, whereas for the rest of the experiments, the potential was first stopped,

then the electrolyte was removed, and then the electrode swapped. **c**, Catalyst particle loading dependence of electro-HFN as well as hydrogenation and HER. Collected at 1 bar CO, -1.45 V vs SCE. **d**, additional data from catalyst loading dependence tests, for electrode formulations containing no Rh. Same conditions as **c**. Conditions unless stated otherwise: 25 °C, 0.52 M styrene, 0.1 M TBAOTf, 25 mM HOTf, in 50% v/v IPA/H_2O. For **a** and **b**, error bars represent standard deviation with n ≥ 3. Data in **c** and **d** are reported for singlicate experiments.

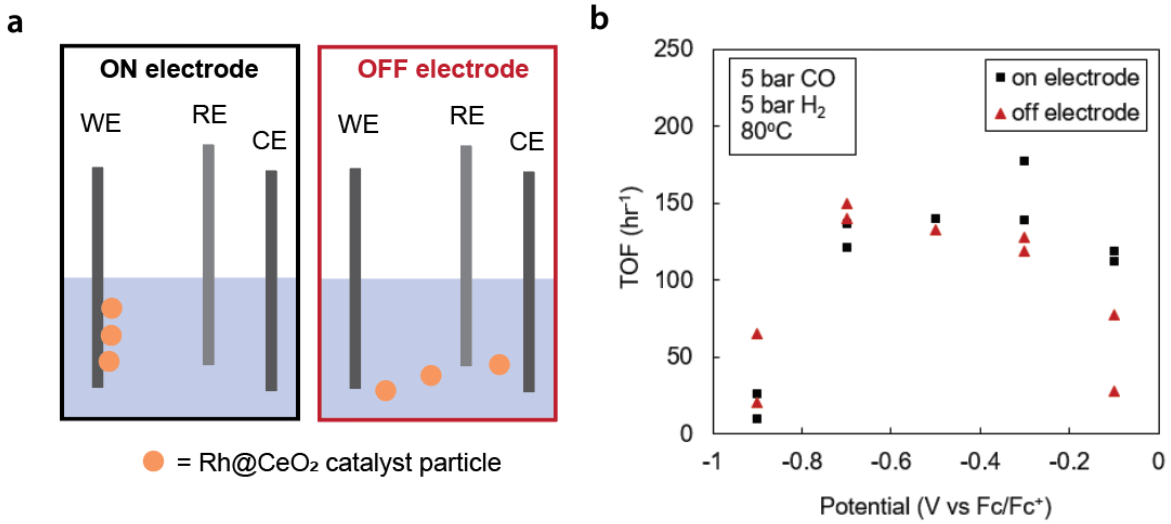

Figure A-C8. Testing for non-Faradaic promotion of electro-HFN. **a**, schematic showing the relevant reaction setups, where in one case, the Rh@CeO_2 catalyst particles are deposited at the working electrode (WE) (termed "on electrode"), and in the other case, the catalyst particles are free floating in the solution (termed "off electrode"). In both cases, voltage is applied at the WE, which is referenced to the reference electrode (RE). Current also passes through the counter electrode (CE), which consists of sacrificial Al foil. **b**, rate of electro-HFN as a function of applied potential for both on and off electrode configurations. Data collected at 80°C, 5 bar H_2, 5 bar CO, 0.2 M styrene, 80% v/v IPA with 20% v/v H_2O, 0.1 M TBAOTf, 25 mM HOTf.

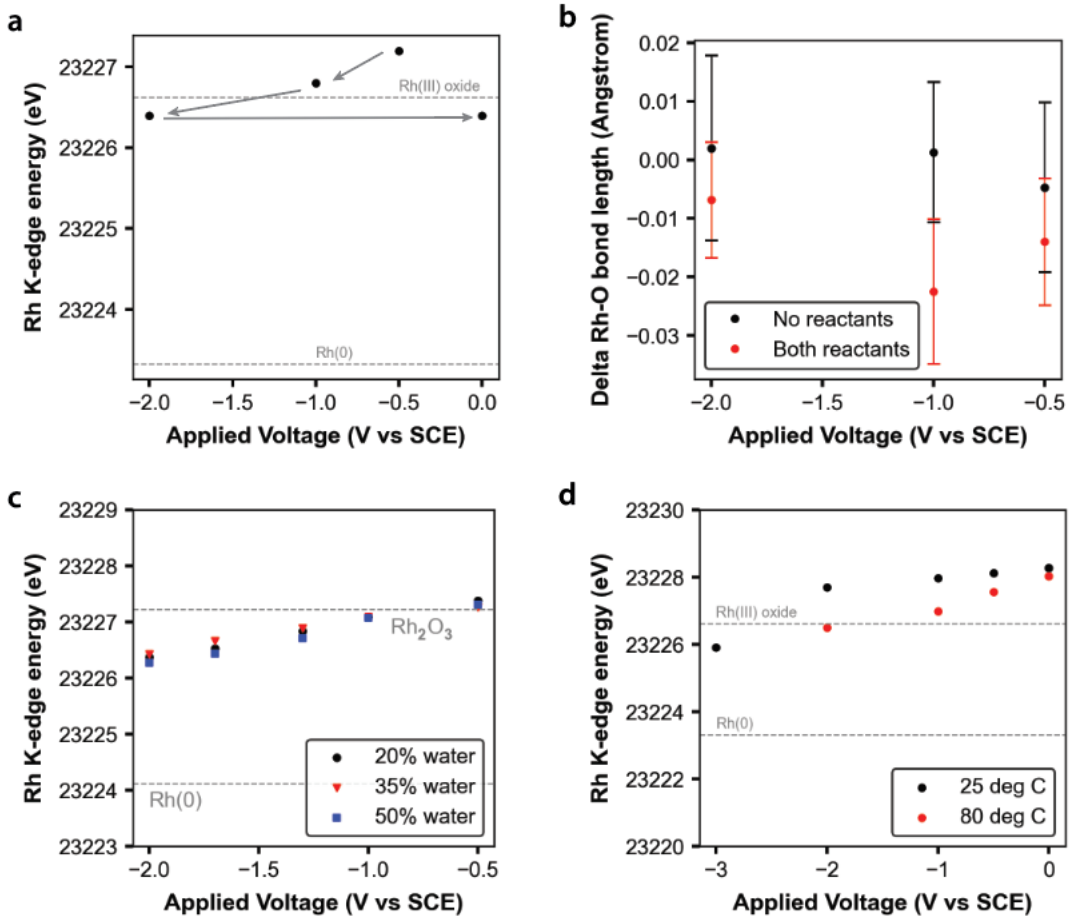

Figure A-C9. Additional XANES and EXAFS data. **a**, Plot of Rh K-edge energy as a function of applied potential, with no reactants present, at 25 ºC. Grey dotted lines indicated energies of known Rh standards and grey arrows indicate temporal sequence of the tested potentials (all points shown were tested in the same cell without changing electrode or electrolyte between different potentials). **b**, fitted EXAFS data of the Rh-O coordination number both with and without reactants (i.e., CO and styrene) present at 25 ºC. Error bars represent fitting errors reported by the fitting software. **c**, Effect of solvent composition on XANES response. Data collected with no styrene and no CO present at 25 ºC. **d**, Effect of temperature on XANES response. Data collected with no styrene and no CO present. All data collected at ambient pressure, 0.1 M TBAOTf, 25 mM HOTf in 80% v/v IPA with 20% v/v H_2O unless explicitly labeled otherwise.

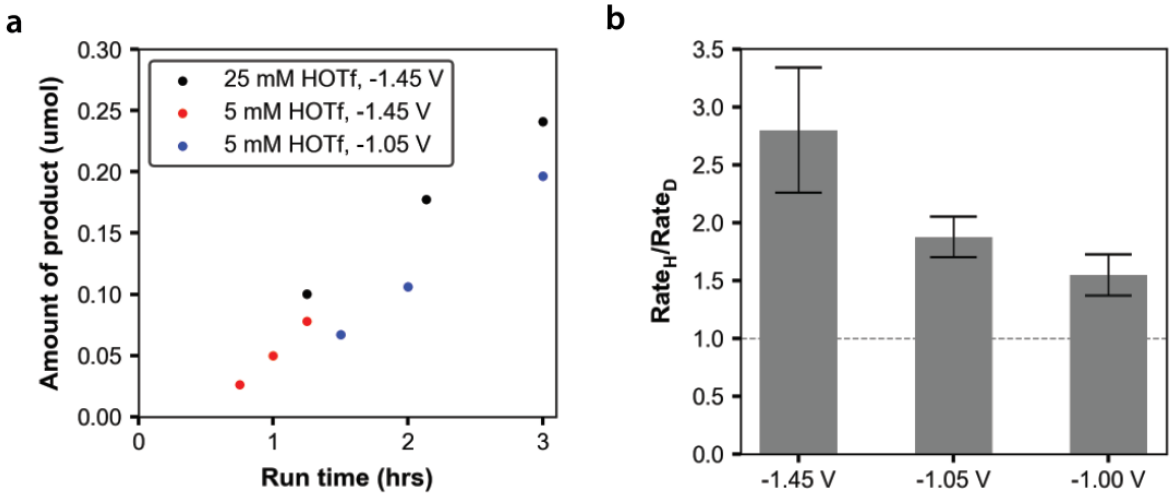

Figure A-C10. Supplemental electrochemical kinetics plots. **a**, Time dependence of reaction kinetics experiments. Each point represents a different electrolysis experiment. Points represent singlicate experiments **b**, Kinetic isotope effect (KIE) data. Reaction was run with D_2O, isopropanol-D8, and DOTf to replace all protons with deuterium. Plotted is the rate with protons divided by the rate with deuterons, at three different applied potentials. Dotted line is drawn through a y value of 1, which represents no KIE. Error bars represent errors propagated through division, where individual errors for numerator and denominator were calculated from standard deviations for $n \geq 3$. Default conditions for both figures, unless explicitly specified otherwise, were at 25 °C, 1 bar CO, 0.52 M styrene, 50% v/v IPA/H_2O mixture (or IPA-D8/D_2O), 0.1 M TBAOTf, and 25 mM HOTf (or DOTf).

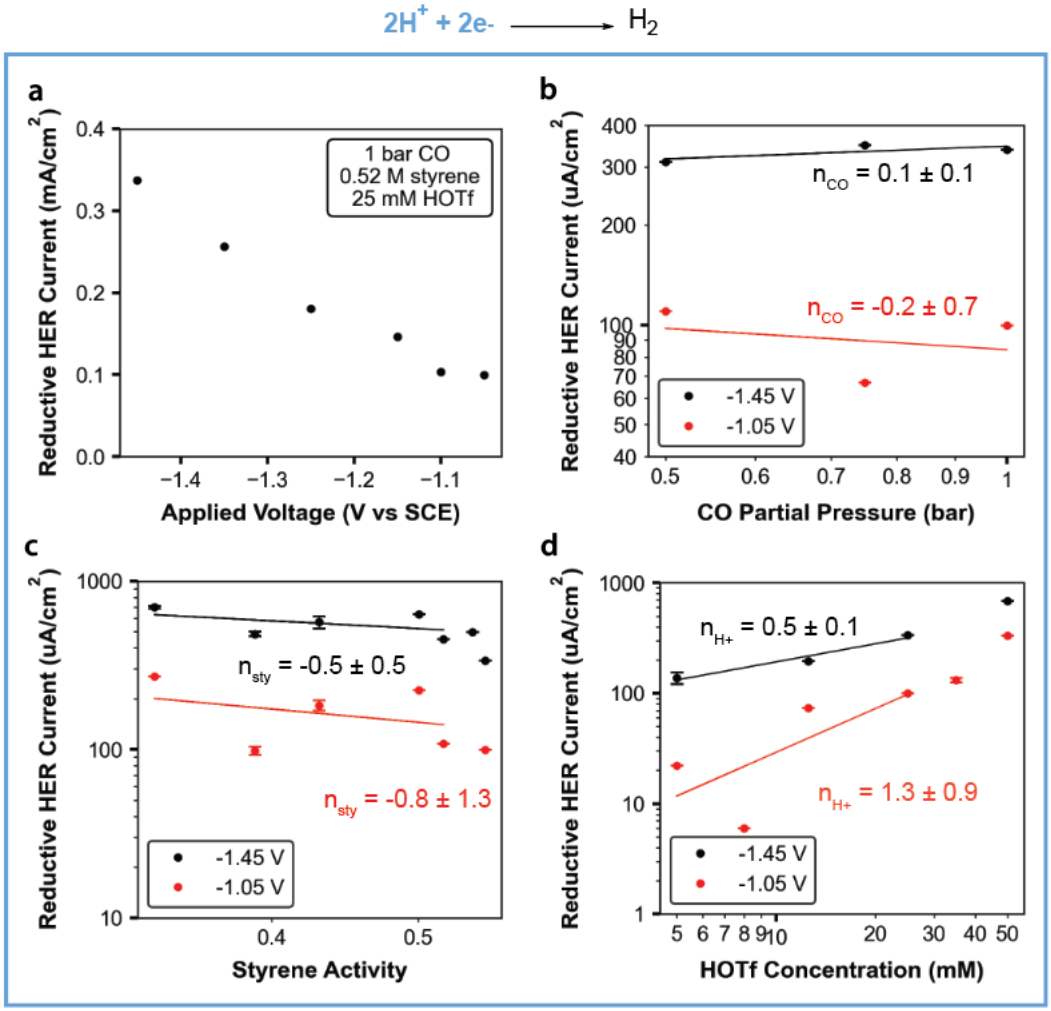

Figure A-C11. HER kinetics. **a**, Tafel (potential) dependence.**b**, CO partial pressure dependence. **c**, styrene activity dependence. **d**, Proton (HOTf concentration) dependence. For **b-d**, black points were collected at -1.45 V vs SCE and red points at -1.05 V vs SCE. All data collected at 25 ºC, 1 bar CO, 0.52 M styrene, 25 mM HOTf, 0.1 M TBAOTf in 50% v/v IPA/H2O mixture unless explicitly specified otherwise. Most points represent singlicate experiments.

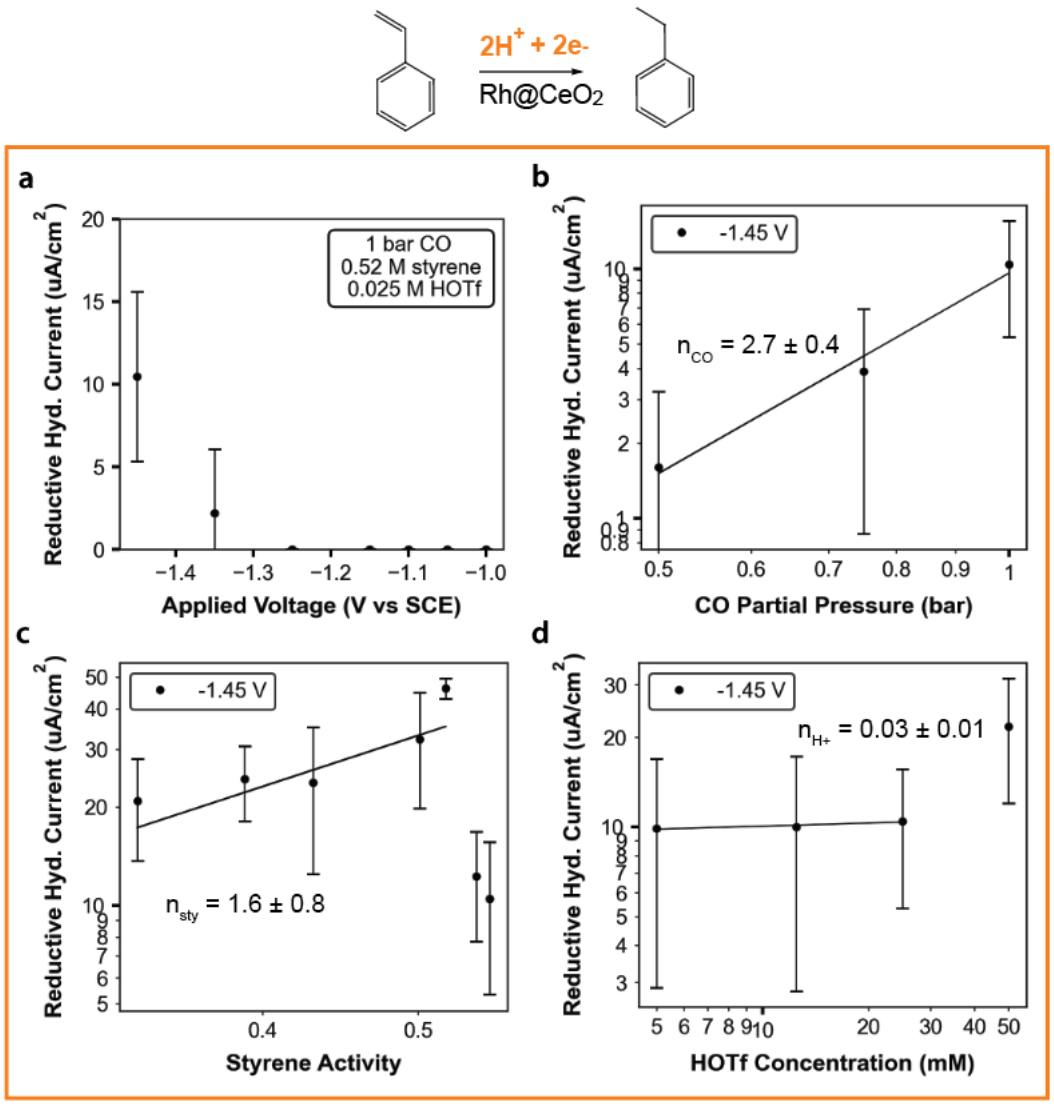

Figure A-C12. Hydrogenation kinetics. **a**, Tafel (potential) dependence. **b**, CO partial pressure dependence. **c**, styrene activity dependence. **d**, Proton (HOTf concentration) dependence. For B-D, kinetic data is reported at -1.45 V vs SCE (no product was observed at -1.05 V vs SCE). All data collected at 25 ºC, 1 bar CO, 0.52 M styrene, 25 mM HOTf, 0.1 M TBAOTf in 50% v/v IPA/H2O mixture unless explicitly specified otherwise. Error bars represent standard deviation for $n \geq 3$.

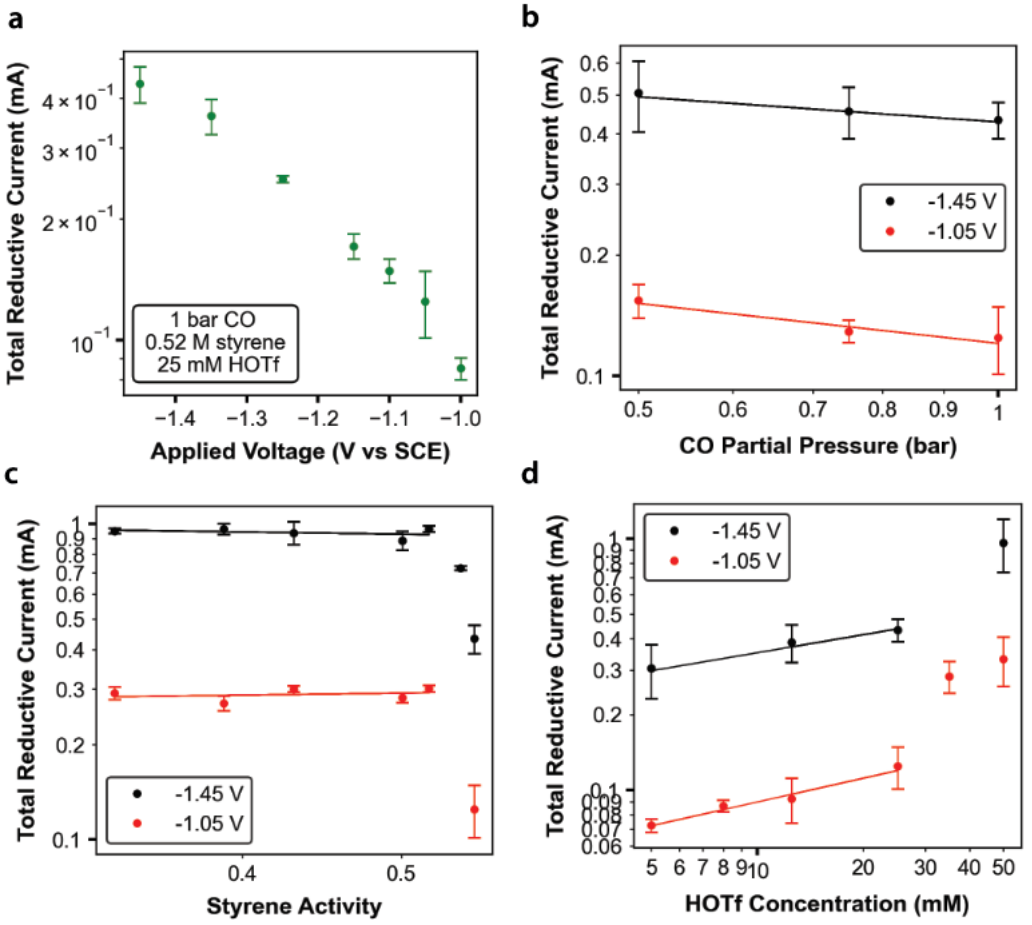

Figure A-C13. Total current kinetics. **a**, Tafel (potential) dependence. **b**, CO partial pressure dependence. **c**, styrene activity dependence. **d**, Proton (HOTf concentration) dependence For **b**-**d**, black points were collected at -1.45 V vs SCE and red points at -1.05 V vs SCE. All data collected at 25 ºC, 1 bar CO, 0.52 M styrene, 25 mM HOTf, 0.1 M TBAOTf in 50% v/v IPA/H2O mixture unless explicitly specified otherwise.

Qty	HFN (-1.45V)	HFN (-1.05V)	HER (-1.45 V)	HER (-1.05 V)	Hyd. (-1.45 V)
Tafel slope	530	173	720	720	148
n_{CO}	0.62 ± 0.06	1.32 ± 0.25	0.13 ± 0.11	-0.21 ± 0.72	2.67 ± 0.35
$n_{Styrene}$	0.91 ± 0.32	0.56 ± 0.37	-0.47 ± 0.51	-0.81 ± 1.34	1.6 ± 0.76
n_{H+}	0.34 ± 0.10	-0.07 ± 0.13	0.55 ± 0.12	1.32 ± 0.93	0.03 ± 0.01

Figure A-C14. Summary table of apparent Tafel slopes and reaction orders for electro-HFN to make 2-phenylpropanal (labeled as HFN, in black), hydrogen evolution to make H_2 gas (labeled as HER in blue), and hydrogenation to make ethylbenzene (labeled as Hyd. in red)